CARBON NANOTUBE SYNTHESIS FOR MICROSYSTEMS APPLICATIONS

A Thesis Presented to

The Academic Faculty

By

Erik Oscar Sunden

In Partial Fulfillment of the Requirements for the Degree

Master of Science in Mechanical Engineering

Georgia Institute of Technology

August 2006

CARBON NANOTUBE SYNTHESIS FOR MICROSYSTEMS APPLICATIONS

Approved:

Dr. Samuel Graham, Chair
Mechanical Engineering
Georgia Institute of Technology

Dr. William King
Mechanical Engineering
Georgia Institute of Technology

Dr. Satish Kumar
Polymer and Textile Engineering
Georgia Institute of Technology

Date Approved: June 16th, 2006

ACKNOWLEDGEMENTS

I would like to thank my thesis advisors Dr.Samuel Graham and Dr.William King for taking the time to both mentor and guide me through my graduate research. The quality of my education and overall graduate school experience would not have been so complete, were it not for them. I would also like to express my deep thanks to Dr.Satish Kumar who has served on my thesis reading committee. Your expertise in this subject matter has helped me write a very high quality thesis.

I would also like to thank my fellow group members, who helped to keep me focused and determined through the tough times. An advanced degree from Georgia Tech involving research requires a strong work ethic and dedication. When this was lacking, I had great friends to lean upon and even offer a place to sleep. In no particular order, thanks are deserved to Adam Christensen, Ashante' Allen, Abe Greenstein, Mark Abel, Stephan Turano, Fabian Göericke, Greg Ostrowicki, Jay Lee, Keunhan Park, Shubham Saxena, Andrew Cannon, Marcus Eliason, Tanya Wright and Brent Nelson.

I would also like to thank my family who has helped support me through all these years at Georgia Tech. It has certainly been nice to have a home so close to campus to visit. Last, but certainly not least, I need to thank my girlfriend, Lindsey. Thanks for showing me a great deal about whom I am and who I'd like to become. You're a real trouper to have stuck with me through these years in my life.

TABLE OF CONTENTS

ACKNOWLEDGEMENTS .... **III**

LIST OF TABLES .... **VII**

LIST OF FIGURES .... **VIII**

SUMMARY .... **XV**

CHAPTER I: INTRODUCTION **1**

- 1.1 Motivation for Research 1
- 1.2 Thesis Overview 8

CHAPTER II: BACKGROUND AND LITERATURE REVIEW OF CARBON NANOTUBES **9**

- 2.1 Structure 9
  - 2.1.1 Singlewalled Nanotubes 10
  - 2.1.2 Multiwalled Nanotubes 13
- 2.2 Synthesis Techniques 15
  - 2.2.1 Chemical Vapor Deposition 15
  - 2.2.2 Arc Discharge 18
  - 2.2.3 Laser Ablation 19
- 2.3 Properties 22
  - 2.3.1 Mechanical Properties 22
  - 2.3.2 Electrical Transport Properties 24
- 2.4 Microsystems Applications 26

CHAPTER III: NANOTUBE GROWTH TECHNIQUES **31**

3.1 Global CVD 31

3.1.1 Experimental Setup & Methods 31

3.1.2 Experimental Results 36

3.2 Localized CVD for Direct Growth 50

3.2.1 Experimental Setup & Methods 50

3.2.2 Experimental Results 58

3.3 CNT Enhancement via Protective Coatings 64

3.3.1 Experimental Setup & Methods 64

3.3.2 Experimental Results 66

CHAPTER IV: NANOTUBE INTEGRATION/PRINTING 70

4.1 Hot Emboss Imprint Lithography 70

4.1.1 Experimental Setup & Methods 70

4.1.2 Experimental Results 73

4.2 Vertical Variable Frequency Microwave Imprinting 76

4.2.1 Experimental Setup & Methods 76

4.2.2 Experimental Results 80

CHAPTER V: MICROBIOLOGICAL APPLICATIONS 84

5.1 CNT Enhanced Substrates for Neuronal Stimulation 84

5.1.1 Experimental Setup & Methods 84

5.1.2 Experimental Results 86

5.2 Cell Guidance Substrates 89

5.2.1 Experimental Setup & Methods 89

5.2.2 Experimental Results 91

CHAPTER VI: SUMMARY AND RECOMMENDATIONS 94
6.1 Summary 94
6.2 Preliminary Results 96
6.2.1 Nonstandard Substrates 96
6.2.2 Multilayered Catalysts 98
6.2.3 SWNT Synthesis via Dendrimer Catalyst 100
6.3 Future Work 101
6.3.1 Future Experiements 101
6.3.2 Experimental Recommendations 101
REFERENCES 103

LIST OF TABLES

Table 1. Parameters of carbon atom in various materials [51] 10

Table 2. Comparison of CNT synthesis techniques. 21

Table 3. Physical properties of single and multiwalled CNTs... 26

Table 4. Process recipe for iron and nickel nanoparticle catalyst. 35

Table 5. Process recipe for thin film catalyst. 35

Table 6. Intesity ratios of D-peak and G-peak from sample Raman scans for samples in Figure 20. 49

LIST OF FIGURES

Figure 1. Vector diagram of carbon nanotube taken from [52]. The chiral angle is defined as the angle between the chiral vector and the closest basis vector. The rectangle created by OAB'B, represents the unit cell of the nanotube. 11

Figure 2. Illustration of the three types of CNTs including a) zigzag, b) armchair and c) chiral, adapted from reference [52]. The chiral angle of the zigzag tube (n,m) is 0° since either n or m equals 0. The chiral angle of the armchair tube (n,m) is 30° since n and m are equal. The chiral tube has n,m integer values between the two extremes. 12

Figure 3. Transmission electron microscropy image of herringbone MWNT taken from reference [57]. The name is given to the layering of the graphitic planes because of the similarity to the stacking of a herring backbone. The dark colored spot in the bottom of the image is the catalyst particle. 14

Figure 4. Transmission electron microscopy image of a bamboo type MWNT taken from reference [58]. The bamboo name is given to the carbon formation because of the similarity to the capsulated growth of bamboo shoots... 14

Figure 5. Various stages of vapor-liquid-solid (VLS) growth mechanism. Catalyst particle in molten state absorbs carbon in vapor form (a) to form an alloy (b). As the particle becomes saturated with carbon, a solid CNT begins to extrude from the particle. The final location of the catalyst particle defines tip grown (c) or root grown (d) CNTs. 16

Figure 6. Formation of germanium nanowires from gold nanoparticles via the vapor-liquid-solid growth mechanism [59]. These transmission electron microscopy images reveal the extrusion of the germanium nanowires (c-i) from the saturated particle (b). 17

Figure 7. Arc discharge synthesis chamber, image taken from reference [52]. Critical components of the synthesis chamber include the anode and cathode graphite rods, vaccum port and gas inlet. An electrical arc creates a synthesis plasma between the rods. 19

Figure 8. Laser ablation setup, adapted from reference [60]. Laser heating in addition to the elevated ambient from the furnace causes the graphite target to evaporate. Carbon nanotubes are collected downstream on the water cooled copper collector. 20

Figure 9. Conductivity roadmap for single walled carbon nanotubes indicating the conductivity of the nanotube produced with a chiral vector of given (n,m) integers. Multiwalled nanotubes tend to be metallic due to the low likelihood of all semiconducting nested nanotubes. 24

Figure 10. Density of states diagrams for a semiconducting CNT (a) and a metallic CNT (b) taken from reference [64]. The spikes in the figure represent energy levels at which electrons tend to exist and are called van Hove singularities. The metallic tube (b) can readily move electrons between the two lowest energy levels. The energy band gap seen in (a) between the lowest level states is indicative of a semiconducting tube (a). 25

Figure 11. IBM produced ring oscillator consisting of 12 transistors built onto the side of an individual CNT [73]. The arrangement of the device allows it to test the speed at which the CNT based transistors are capable of switching. 27

Figure 12. Nanotube emitting display made by Motorola Labs [74]. The use of CNTs as field emitters has the potential to make display panels millimeters thin and economical to manufacture. 28

Figure 13. High tensile strength in CNT fabric is demonstrated as droplets of orange and cranberry juice and water are placed onto two stacked CNT sheets [75]. The droplets are roughly 50,000 times the mass of the two perpendicularly arranged CNT fabrics. 29

Figure 14. Easytube 1000 series tube furnace featuring a 5cm diameter quartz tube, automatic sample loader and 4 separate programmable mass flow controllers. 31

Figure 15. Sample diameter measurements of CNTs, created at 800 °C with iron nanoparticles in solution, taken using Metamorph image processing software. The image colors have been inverted to more easily see the measurement marks. 36

Figure 16: Iron catalyst MWNTs at varying synthesis temperatures, ethylene and acetylene gas flows compared. Sample error bars represent 1 standard deviation from a set of acetylene data and the thin film data point. Average mean diameter increases along with diameter standard deviation with elevated synthesis temperature. All the samples represented in this analysis were produced in synthesis periods of 10 minutes. 38

Figure 17. Comparison of low and high aspect ratio CNT growth on iron nanoparticles using acetylene, methane, and hydrogen at temperatures of 600 °C and 900 °C, respectively. Synthesis temperatures below 600 °C generally did not produce highly graphitic nanofeature growth. 39

Figure 18: Typical SEM images of (a-c): Iron catalyzed CNTs produced at 600, 750, 900 °C respectively, (d-f): Nickel catalyzed materials produced at 500, 600, 700 °C. All these nanomaterials were created using the same acetylene/methane/hydrogen gas recipe as detailed above. 41

Figure 19. : Acetylene produced CNFs (a) Ethylene produced CNFs (b), both using nickel catlalyst at a synthesis temperature of 500 °C. The application of a 50V bias

to the sample during synthesis proved to increase the amount of helical configured CNFs as seen in (a). 43

Figure 20. Alignment results of various catalysts. Evaporate thin film demonstrated the greatest probability to form vertically aligned features as seen in (a,b). Vertical alignment was also seen in some cases where particles in solution were spinning coated onto a substrate (c). Drip dispersing catalyst particles demonstrated only randomly arranged CNTs (d). 44

Figure 21. Short vertically aligned growth measuring 4-5 μm in height, caused by growth period conditions of 700 sccm ethylene at 700 °C for 2 minutes. At this temperature, ethylene provides little carbon to the synthesis reaction resulting in short growth and high control of the produced CNT height. 46

Figure 22. Transmission electron microscopy images of MWNTs produced with iron particles at (a) 500 °C (b)750 °C and (b)900 °C. The increase in graphitization with higher synthesis temperature is seen in images (b,c) as evidenced by their more pronounced sidewalls. The scale bar is equal to 5 nm. 47

Figure 23. Raman spectroscopy scans of nanostructures produced at synthesis temperatures of 500 °C, 750 °C, and 900 °C using nanoparticle in solution based catalyst. The ratio of the defective band (1350-1365 cm^{-1}) over the graphitic band (1580-1620 cm^{-1}) is seen to decrease for each increase in synthesis temperature. This is supported by the transmission electron microscopy results shown above in Figure 22, that also indicate lower amounts of defects and greater graphitization at higher synthesis temperatures. 48

Figure 24. Image of heated atomic force microscopy cantilever fabricated at Georgia Tech. The cantilever features a resistive heating element in the end of the device and a read/write tip.. 50

Figure 25. Infrared image demonstrating cantilever heating capability. The device shown is safely approaching 370 °C in the lesser resistively doped heater region. These cantilevers have demonstrated temperatures upwards of 800 °C without thermal damage. 51

Figure 26. Scanning electron microscope image shows thin film iron catalyst breaking up under heating from the cantilever heater region. As the cantilever continues to heat, the iron film will continue to disperse and create CNT nucleation sites across the end of the cantilever. Also pictured at center is the sensing tip of the cantilever. 52

Figure 27. Cantilever resistance response to input voltage signal of 0-5 V. As seen in the figure, the iron deposition, temperature calibration and synthesis of the CNTs does not radically affect the electrical response of the device. The iron catalyst film is sufficiently thin such that it does not cause continuity across the cantilever electrical contact pads. 53

Figure 28. Raman temperature calibration of heated AFM cantilever. The Raman shift is linear with increase in cantilever input power during calibration. Because the Raman shift is also linearly related to the temperature of silicon, cantilever temperature can be estimated from input power to the device. 55

Figure 29. Cantilever image at left shows Raman spectroscopy scanning points. Plot of heating profiles is taken from work done previously on characterizing the heater region of thermal cantilever [28]. Plot indicates maximum temperatures at center of heater region.. 56

Figure 30. Cantilever mounting diagram for localized synthesis. Synthesis is performed inside quartz tube with no assistive ambient heating. Synthesis process takes approximately 10 minutes to complete and is readily assembled............................ 56

Figure 31. Enlarged detail of cantilever during CNT synthesis. During heating, carbon gases are decomposed and allowed to saturate the catalyst particles on the cantilever end.. 57

Figure 32. Scanning electron microscope image of the cantilever with CNTs on the heater region. As seen in the image, the CNTs are locally confined to the desired synthesis area.. 58

Figure 33. Enlarged view of cantilever heater region with CNT growth. The growth of CNTs is locally confined to the heater region and the tallest growth occurred at the midpoint of the heater region where temperatures are greatest. Breakup of the iron catalyst film can be seen extending outwards towards the legs of the device where temperatures gradually decrease.. 59

Figure 34. Resonant frequency of cantilever during process. With the added mass of the iron catalyst film, the frequency dropped to 119.10 kHz. After synthesis, the added point mass of CNTs resulted in a frequency decrease to 118.23 kHz. When the CNTs were removed through oxidation, the cantilever natural frequency increased to 119.09 kHz.. 60

Figure 35. Heating time constant of cantilever. As seen, the added thermal mass of the CNTs did not alter the heating time constant of the cantilever heating region......... 61

Figure 36. Schematic image of polysilicon heater beam. Beams were made from polysilicon on oxide wafers using a two step lithography process in lengths of 100, 200, 300, 400, 500 μm and widths of 5, 10, 20 μm. The aluminum contact pads seen in yellow were 1cm^2 for electrical connectivity. 62

Figure 37. Growth of CNTs on polysilicon heater beam. The synthesis of CNTs onto heated beams proved easier than onto the cantilever structure due to their large size and ability to withstand large amounts of input power... 63

Figure 38. Experimental setup of an atomic layer deposition chamber (ALD). Similar to the chemical vapor deposition setup, ALD involves both mass flow controllers and a heated box furnace. In this setup however, solenoid valves provide the ability to pulse process gases. 64

Figure 39. Linkam TS-1500 spectroscopy compatible heating stage. The top viewport window allows for Raman microscopy scanning at elevated temperatures up to 1500 °C. The chamber also has the capacity for vacuum, electrical feed-through, and gas connections. The stage temperature is controlled using heating pulses from a separate temperature controller. The stage is used to characterize samples under elevated temperatures.. 66

Figure 40. Degree of graphitization given by the ratio of the Raman measured G band (1580-1620 cm^{-1}) intensity over the initial graphitic band intensity. While the control sample and TiO_2 coated CNTs show rapid loss in graphitization, the Al_2O_3 coated CNTs prove to be more resistant to oxidation at 700 °C.............................. 67

Figure 41. ALD coated CNTs, 10 nm Al_2O_3 (a,b), 10 nm TiO_2 (c,d), all scale bars are equal to 100 nm. The Al_2O_3 coated tubes (a,b) exhibit diameters between 40-50 nm, thus supporting the 10 nm conformal coating onto ~20-25 nm CNTs. The CNTs coated with 10 nm TiO_2(c,d) however, appear similar to the original 20-25 nm features. 68

Figure 42. Imprint lithography printing process. The CNT patterned silicon coupon is placed face down onto the polymer substrate (a). This sandwich is placed inside the heated press on top of a clean middle disk resting on a rubber spacer. The rubber helps achieve a uniform loading across the sample. After pressure is applied for 4 minutes the platens are separated revealing the sample.. 71

Figure 43. Scanning electron microscopy image of two dimensional CNT imprint by hot emboss imprint lithography process. As seen in the image, the CNTs are well adhered to the substrate. The CNTs have a very low vertical profile and show very low traces of catalytic iron particles at higher magnification images...................... 73

Figure 44. Typical I-V response of imprinted CNT trace. The linear behavior of the CNT trace is similar to the response of a resistor, indicating that most of the CNTs are metallic. The resistance of the trace decreases with resistive heating up to 80 V, where the trace begins to experience failure due to melting of the surrounding polymer. 74

Figure 45. Imprinted CNT trace response to bending strain. Varying amounts of bending strain were applied to the trace and the resistance was found to vary 1% between 3 successive trials. This demonstrates the ability of the CNT-CNT network within the trace to accept deformation and reforming without a loss of electrical conductivity. 75

Figure 46. Schematic shows process of transferring CNTs into a polymer substrate by variable frequency microwave excitation (a-c). The CNT patterned coupon is placed face down onto the polymer substrate (a). The sandwich is then placed inside microwave chamber and exposed to electromagnetic waves for 4 minutes (b). The silicon coupon is then lifted from the embedded CNTs, leaving vertically standing features (c). 76

Figure 47. Individual temperature profiles for CNTs, silicon, and polycarbonate substrate during microwave exposure process. Each sample was exposed under the same power setting for 2 minutes and monitored via an infrared temperature sensor. The silicon demonstrated the greatest ability to absorb microwaves, while the polycarbonate did not show any signs of heating. This indicates that heat generated in the silicon and CNTs is conducted through the CNTs to melt the polycarbonate substrate locally. 79

Figure 48. Microwave embossing of vertical aligned CNTs. Differences in adhesion between the silicon substrate and the CNTs accounts for the torn CNT appearance (a,b) versus the smooth surface appearance (d). The CNTs are submerged into the melted substrate as seen in image (c). 81

Figure 49. Hydrophobicity test of vertically standing CNTs. The CNTs proved to be superhydrophobic with a measured water droplet contact angle of 168°. The arrows in the image indicate the edges of the vertically standing CNT regions on the polymer substrate. 83

Figure 50. Scanning electron microscopy image demonstrating the uniformity of plasma enhanced deposition of SiO_2 onto CNTs. The oxide coating is shown to only adhere to the outer most CNTs where diameters are close to 80 nm. The plasma does not coat CNTs closer to the center of the group where diameters still measure close to 25 nm. 87

Figure 51. Scanning electron microscopy images of neurons cultured on SiO_2 coated CNTs. The neurons appear to prefer the roughened CNT surface over the bare silicon substrate. Neurons are also shown to extend between CNT features and no negative effects to the silicon dioxide coatings. 88

Figure 52. Scanning electron microscopy images of cellular adhesion to imprinted CNT patterns. These substrates were prepared using the hot embossing method to imprint CNTs into polycarbonate. The filopodia appear well anchored to the CNT features. 91

Figure 53. Florescent microscopy image of cells on CNT infused substrate. The image colors have been altered to make the cells more visible. As seen in the figure, there is a large amount of cell-cell interaction due to the high seeding density. The 5 μm CNT traces are shown as light grey vertical lines and are spaced 5 μm apart. 92

Figure 54. CNT growth onto MFI type zeolite structures. The CNT growth is quite long measuring 300 μm in length in images (a,b). Another item to note is the thin CNT in images (c,d), measuring less than 10 nm in diameter. 97

Figure 55. Images depict CNT synthesis attempts onto alternative substrates. These scanning electron microscopy images depict thin film iron growth onto a graphite sheet(a), a copper block(b), a stainless steel block(c) and lastly onto copper foil(d). 98

Figure 56. Scanning electron microscopy image of CNT growth using aluminum-iron thin film catalyst. The resultant structures in the image appears similar to iron thin film growth, but also exhibit a second phase of larger diameter tubules on top of the vertically aligned CNT array. 99

Figure 57. Scanning microscopy image of thin film titanium-iron catalyzed CNT growth. As seen in the image, titanium restricts the CNTs from achieving tall vertical alignment.. 100

SUMMARY

Modern day engineering systems research presently lacks techniques to exploit the unique properties of many nanomaterials; coupled with this challenge exists the need to interface these nanomaterials with microscale and macroscale platforms. A nanomaterial of particular interest is the carbon nanotube (CNT), due to its enhanced physical properties. In addition to varied electrical properties, the CNT has demonstrated high thermal conductivity and tensile strength compared to conventional fiber materials. CNTs are beginning to see commercial applications in areas in which sufficient study has been dedicated. While a large part of the worldwide focus of CNT research has been in synthesis, an equally important area of research lies in CNT integration processes. The unique and useful properties of many nanostructured materials will never be realized in mainstream manufacturing processes and commercial applications without the proper exploration of integration methods such as those detailed in this thesis.

The primary motivation for the research detailed in this thesis has been to develop CNT synthesis processing techniques that allow for novel interfacing methods between carbon nanotubes and eventual applications. In this study, an investigation was performed to look at several approaches to integrating CNTs into micro-electromechanical systems (MEMS). Synthesis of CNTs was studied in two different settings. Synthesis was first performed, directly on the microsystem, via a global scale chemical vapor deposition (CVD) process. Secondly, synthesis was performed directly onto a microsystem device via localized resistive heating. Following synthesis, the application of atomically layered, protective coatings was then investigated. Integration methods were then investigated to allow for CNT transfer to microsystem applications incapable of withstanding synthesis temperatures. The developed integration methods were evaluated by creating functional microscale electrical circuits in flexible substrates via hot emboss imprint lithography. Lastly, post synthesis processing methods were used to create micropatterned cell guidance substrates as well as neuronal stimulating substrates.

CHAPTER I: INTRODUCTION

1.1 Motivation for Research

Carbon nanotubes (CNTs) are perhaps the most widely investigated nanomaterial because of their thermal [1], electrical [2], and mechanical [3, 4] properties. Discovered in 1991 [5], their promise of being a super material capable of endless applications is still primarily under research. While the possibilities of nanomaterials, like CNTs, are still being realized, there is a lack of techniques to exploit their unique properties; in particular there is a need to interface nanomaterials with microscale and macroscale platforms. The primary motivation for the research detailed in this thesis has been to develop CNT synthesis techniques that allow for interfacing methods between carbon nanotubes and microsystems applications. The following sections detail the growth and integration methods of CNTs as well as their use in microbiological substrates.

CNT synthesis tailored to subsequent microsystem applications can be performed in two primary ways, global growth or localized growth directly into the microsystem. Protective, atomically layered films can also be applied to CNTs after the process of either global or direct synthesis.

Synthesis of Carbon Nanotubes

Global synthesis attempts to produce CNTs in a high temperature environment directly on the actual microsystem, where the entire microsystem is exposed to the high temperature field. Synthesis methods such as arc-discharge [6, 7], laser ablation [8, 9], pyrolysis, and numerous types of chemical vapor deposition (CVD) [10-13] provide many different ways to produce CNTs. The synthesis of CNTs by the global CVD method is of great interest due to its ability to be easily modified and scaled-up in terms of quantities produced. The challenge of the CVD method lies in the multitude of parameters involved, any of which can have dramatic effects on the material produced [14]. The use of metal nanoparticles as a catalyst source to the CVD process is of great interest due to the large amount of commercially available particles and the low concentrations of particles in solution necessary to facilitate CNT growth. The use of nanoparticles and thin films as catalyst sources is a well documented method of providing catalyst to the synthesis reaction [15-18]. The success of CVD as a reliable synthesis method for producing commercial quality CNTs requires a detailed, systematic study of all the growth parameters involved in a given synthesis setup.

By varying global growth parameters such as synthesis temperature and types of carbonaceous gases, this study attempted to qualify a regime of the output capabilities of the thermal CVD method using iron and nickel nanoparticles. The size, structure and general quantity of produced CNTs are all affected by the synthesis parameters and thus justify a need for such a study. Although studies exist for particular thermal CVD experimental setups, none have dealt with the specific setup employed in this experiment. In performing this study, the use of nanoparticles is also compared to the use of more conventional thin catalyst films deposited via sputtering and thermal evaporation [19-21]. In summary, global CVD synthesis creates CNTs at high temperatures directly onto the microsystem by exposing the entire system to elevated temperatures.

Localized synthesis of CNTs allows for the direct introduction of nanostructures onto a microsystem, safely containing the elevated processing temperatures to a confined microscale area. The integration of nanomaterials with microelectronics, microelectromechanical systems (MEMS), and macroscale sensors has otherwise been demonstrated with directed self-assembly [22], directed growth on micropatterned catalytic sites [23], spin casting [24], and electrophoretic trapping [25]. While these integration techniques are scalable, they require global exposure of the device to the processing procedure, which may risk contamination and/or make the process incompatible with CMOS processing. For example, the chemical vapor deposition synthesis of CNTs typically requires temperatures up to 900°C and processing windows greater than 100 minutes, most of which is attributed to the heating and cooling of the synthesis chamber. This high temperature renders impossible direct CNT synthesis on most MEMS and electronics. Attempts to reduce the synthesis temperatures using PECVD have resulted in nanostructure growth temperatures as low as 120 °C [26]. However, relatively high temperatures are still needed to produce tubes of high quality. Local synthesis can circumvent these risks, facilitating nanomaterial integration in only desired areas while leaving the remainder of the device platform unaffected. CNT growth in a room-temperature reactive gas onto microfabricated heaters is significantly faster than CNT growth in a furnace because of the extremely small thermal mass of the micro-heater, and further offers highly local control of CNT growth [27, 28]. While the localized synthesis of carbon nanostructures onto a microfabricated heater has been demonstrated [27], this work did not employ local temperature calibration, nor was it capable of integrated quantitative assessment of the CNTs. This technique for highly local materials growth and measurement is compatible with any CVD material, and creates novel opportunities for interfacing nanomaterials with microstructures.

The use of CNTs as tips for scanning microscopy tools such as atomic force microscopes has been widely documented and practiced over the last ten years. CNTs are an ideal substitute for a conventional probe tip, due to their large aspect ratio, small tip radius and robust mechanical properties. A number of methods are currently available to attach the nanotubes to the end of the cantilever device, including arc joining and global chemical vapor deposition. The method of localized heating, however, allows for localized chemical vapor deposition of any material created via thermal CVD, including CNTs [29]. In summary, localized synthesis via selective heating allows for direct growth of CNTs into microsystems that can locally withstand the elevated temperatures.

Conformal nanotube coatings could help to make them more robust and capable of withstanding harsh environments. The atomically layered films can be deposited over a large area onto globally synthesized CNTs or over small areas onto locally synthesized CNTs. The ease with which these protective layers can be deposited following synthesis, supports their mention with aforementioned CNT production processes. Thermal oxidation via heating in moist air is a reliable way to eliminate carbon nanotube deposits. Oxidation can be delayed and possibly prevented however, by applying an insulating coating such as aluminum oxide or titanium oxide. The use of such films would allow for a utilization of the nanotubes in an otherwise compromising and destructive environment. Global and localized synthesis techniques and secondary coatings are important processes that dictate the success of nanostructure integration.

Integration with Flexible Electronics and MEMS

Opposite to high temperature synthesis and coating processes, low temperature interfacing methods are vital to applications where elevated temperatures can cause damage to sensitive microsystem components. These processes can be coupled with one-dimensional semiconductor nanomaterials for creating a wide range of macroelectronics and sensors on flexible substrates with excellent transport mobilities, along with novel optoelectronic and piezoelectric properties [30-32]. Previous research has shown that random carbon nanotube (CNT) networks may possess electron mobilities as high as 270 cm^2/V-s and transistor on-off ratios as high as 10^4, [33] while micro-silicon networks exhibit transport mobilities near 180 cm^2/V-s [34]. Combining these inherently flexible materials with polymer and paper substrates could yield low-cost high-performance devices which cannot be produced using current semiconductor processing methods. Flexible electronics device manufacture from nanomaterial building blocks is a key challenge, as direct synthesis of nanomaterials on flexible substrates is typically forbidden due to material-processing incompatibilities. A few methods have attempted to address this challenge of incorporating high-mobility nanomaterials into flexible substrates, either by self assembly or direct printing on polymer substrates [30, 35-42]. In general, the processing technologies can be classified as solution-based [36, 40] or dry transfer printing [35, 39, 42]. In solution-based printing such as spin casting, flow-directed alignment, or electrophoretic trapping, the nanomaterials are suspended in an "ink" solution which is used to transfer the material to the substrate. These techniques can be used to pattern a wide range of features and are amenable to high throughput manufacturing. However, care must be taken in developing the particle/solution/substrate chemistry to ensure material compatibility. Dry transfer printing techniques use stamps to transfer the nanomaterials to a variety of substrates and may be done without [40-42] or with the assistance of an electric field [43, 44]. Dry transfer printing methods can be advantageous over solution-based processing as they do not require substrate-fluid compatibility.

Two dry transfer, embossing methods were utilized to integrate both conductive and semi-conductive nanomaterials into flexible polymer substrates. Nanomaterials are transferred from an intermediate microfabricated master template into a thermoplastic substrate during embossing processes. The techniques are compatible with nanomaterial synthesis techniques that use the vapor-liquid-solid or vapor-solid growth mechanism. The current techniques differs from other dry transfer printing methods in that the nanomaterials are synthesized directly on the master template in discrete patterns and transferred to the polymer substrate with no intermediate steps. One benefit to the use of nanomaterials is that it would allow for low cost, durable electronics. These devices would be capable of flexing and withstanding harsh environments, and be cost effective enough to be considered disposable. Recent research has developed new methods for integrating CNTs into polymers via their casting into viscous liquid polymers and subsequent curing [45]. These casting methods present their own processing and handling problems however, due to the lack of a defined rigid polymer substrate. In summary, low temperature printing still represents one of the more promising transfer methods that allows for interfacing CNTs into microsystems that cannot withstand high temperatures.

Biomedical Applications

CNT infused substrates, created by dry transfer printing, are of particular interest for select biomedical applications and microbiological research. Prosthetics research on carbon nanofibers has shown that osteoblast cells can demonstrate enhanced functionality with a decrease in nanofiber diameter [46] as well as promote a reduction in scar tissue [47]. CNTs are also not biodegradable, which could allow them to act as an extracellular scaffolds to guide directed neurite outgrowth [48]. Additional research on neuronal cell cultures has shown that CNTs, as devices, can improve neural signal transfer in a network of cells [49]. This study investigated the possibility to stimulate neuronal cells via carbon nanotube electrodes. With successful signs of neuronal stimulation, evidence would support the use of CNTs for minimally invasive, neuronal activity sensing implants. Studies are also being conducted on the use of micropatterned carbon nanostructure substrates that can encourage cell function and development, as seen before with hot embossed microchannels [50]. For a cell line to show preferential growth to a given substrate means that the cell line can be engineered to grow in a controllable manner or direction.

1.2 Thesis Overview

The purpose of this research is to develop synthesis techniques of carbon nanotubes (CNTs) that allow for the integration into microsystems applications. This thesis presents work targeting CNT growth, CNT integration techniques and finally CNT enabled microbiological applications.

A literature review of CNTs is the focus of chapter 2. Items in discussion include the structure of single and multiwalled nanotubes, various synthesis techniques, mechanical and electrical properties, and finally existing microsystems applications of CNTs. Chapter 3 focuses mainly on the global and local growth of CNTs and also on post-growth protective coatings. Chapter 4 focuses on nanotube integration techniques made necessary where high synthesis temperatures prevent direct CNT growth. Chapter 5 presents microbiological applications made possible by the integration of CNTs as seen in Chapter 4. Finally, chapter 6 presents conclusions on this project and possible future experiments.

CHAPTER II: BACKGROUND AND LITERATURE REVIEW OF CARBON NANOTUBES

2.1 Structure

A CNT is comprised of one or many graphitic sheets, rolled up into a cylinder. Carbon can exist in many forms and take on varying chemical and physical properties that will be detailed in later sections. Carbon atoms have six total electrons, occupying the $1s^2$, $2s^2$, and $2p^2$ orbitals. The bond strength between the valence electrons in the outer two orbitals is weaker than that in the $1s^2$ orbital, thus allowing a mixing or hybridization of the electrons. This mixing is made possible by the small energy difference between the 2s and 2p energy levels. The three possible hybridizations in carbon are sp, sp^2 and sp^3 and three respective example materials include acetylene, polyacetylene, and methane. Table 1, compiled by Saito et al. [51], shows some of the physical parameters given for the isomers made possible by the different hybridizations of carbon.

Table 1. Parameters of carbon atom in various materials [51]

Dimension	**0-D**	**1-D**	**2-D**	**3-D**
	C_{60}	Carbon nanotube	Graphite	Diamond
Hybridization	sp^2	sp^2	sp^2 (sp)	sp^3
Density (g/cm^3)	1.72	1.2-2.0	2.26	3.515
Bond Length (Å)	1.4	1.44	1.42	1.54
Electronic properties	Semiconductor E_g=1.9 eV	Metal or Semiconductor	Semi-metal	Insulator E_g=5.47 eV

The physical characteristic that predominantly determines the behavior of CNTs is the structure of the carbon atoms within the graphitic sheet. For example, the chirality of the CNT, the twist or wrap-angle of the nanotube with respect to its central axis, determines the electrical characteristics of the tube. The mechanical strength of CNTs, estimated higher than 1 TPa in the tensile direction [3], is also largely affected by the arrangement of the carbon atoms and the general defectiveness of this structuring. CNTs can be grouped into two classifications based upon the number of layers of graphitic carbon that comprise their sidewalls. Tubes consisting of one single layer are called singlewall CNTs (SWNTs) and those having more than one layer of carbon are referred to as multiwall CNTs (MWNTs). CNTs of both types are of considerable interest depending upon the situation and application.

2.1.1 Singlewalled Nanotubes

Singlewalled nanotubes are viewed as the more promising type of nanotube for electrical applications due to their ability to be either conducting or semiconducting. The structure and conductivity of the nanotube is determined by the chirality of the nanotube, which is defined by its chiral vector, depicted as C_h in Figure 1 below.

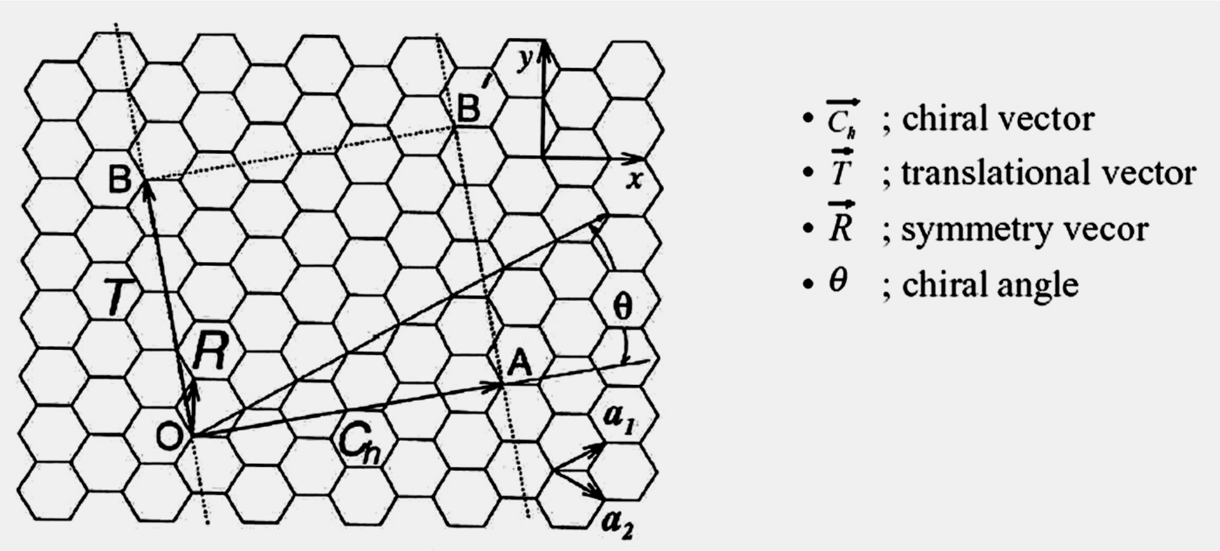

Figure 1. Vector diagram of carbon nanotube taken from [52]. The chiral angle is defined as the angle between the chiral vector and the closest basis vector. The rectangle created by OAB'B, represents the unit cell of the nanotube.

The chiral vector defines the amount of twist present in the hexagonal network of carbon atoms with respect to the central axis of the tube. As seen in Figure 1, the axial direction of the nanotube is given by vector OB. The chiral vector, given by OA, is the direction in which the nanotube rolls up. The unit cell of the nanotube is bounded by the rectangle OAB'B. The formula for the chiral vector is

$$C_h = a_1 \cdot n + a_2 \cdot m$$

where n and m are integers and a_1 and a_2 are the basis unit vectors shown in the hexagonal carbon network above in Figure 1. The nanotube shown in Figure 1 is a (4,2) tube. The chiral angle θ, defined by the angle between the chiral vector and one of the basis vectors, can never be greater than 30°. The chiral angle reaches a maximum of 30°

when the nanotube basis vector integers are equal. The chiral vector is a minimum of 0° when the tube has coordinates (n,m) equal to (0,m) or (n,0). The chiral vector dictates the geometric arrangement of the nanotube and there exist three distinct possible classifications. The names given for the three classes are armchair, in which *n* is equal to *m*; zigzag, where *m* is equal to 0; and helical, in all other cases, are illustrated below in Figure 2.

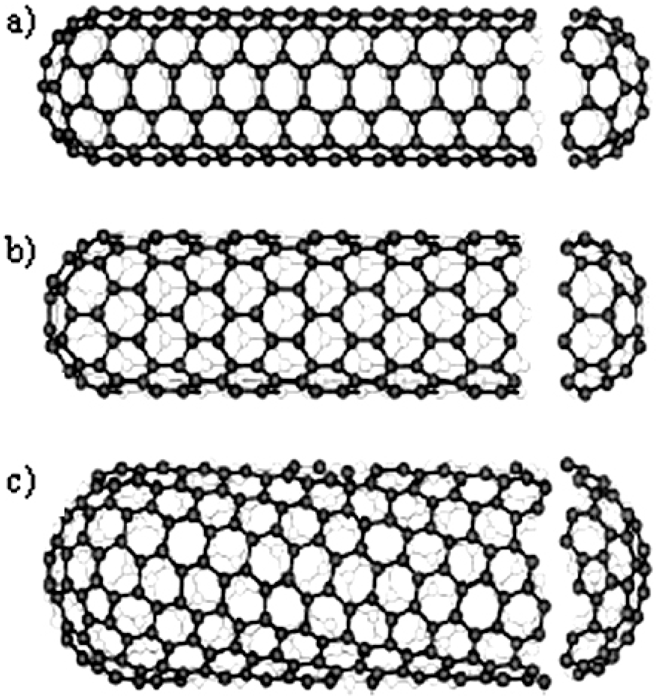

Figure 2. Illustration of the three types of CNTs including a) zigzag, b) armchair and c) chiral, adapted from reference [52]. The chiral angle of the zigzag tube (n,m) is 0° since either n or m equals 0. The chiral angle of the armchair tube (n,m) is 30° since n and m are equal. The chiral tube has n,m integer values between the two extremes.

The approximate diameter of single walled nanotubes can be calculated from the *n* and *m* integers of the chiral vector, C_h. The nanotube diameter, D, can be given by,

$$D = \frac{|C_h|}{\pi} = \frac{a_{cc}\sqrt{3(n^2 + m^2 + nm)}}{\pi}$$

where a_{cc}, $1.41\,\text{Å} \le a_{cc} \le 1.44\,\text{Å}$, is the average carbon-carbon bond length as found in graphite (lower limit) and in C_{60} fullerine molecule (upper limit)[53]. The smallest diameter nanotube that has been experimentally synthesized is 4 Å [54]. The upper bound for SWNTs has not been experimentally determined, but calculations have shown that collapse due to van der Walls forces is favorable at diameters above 25 Å [55]. Carbon nanotubes can be produced with very large aspect ratios, as SWNTs have been measured to lengths of several centimeters [56].

2.1.2 Multiwalled Nanotubes

Multiwalled nanotubes (MWNTs) can be thought of as concentric singlewalled nanotubes of increasing diameter arranged in a nested, Russian doll type fashion. The material properties of MWNTs are mostly dependent upon the perfection and orientation of the graphitic planes comprising the MWNT[53]. Depending upon the structuring of the concentric nanotubes and the presence of slight imperfections, a multiwalled nanotube can exhibit a number of structural formations including herringbone and bamboo type. Herringbone MWNTs exhibit graphitic planes, also called graphines, at an angle to the central nanotube axis. When many such angled planes are stacked over a given length of the nanotube as seen in Figure 3, it looks similar to a herring backbone.

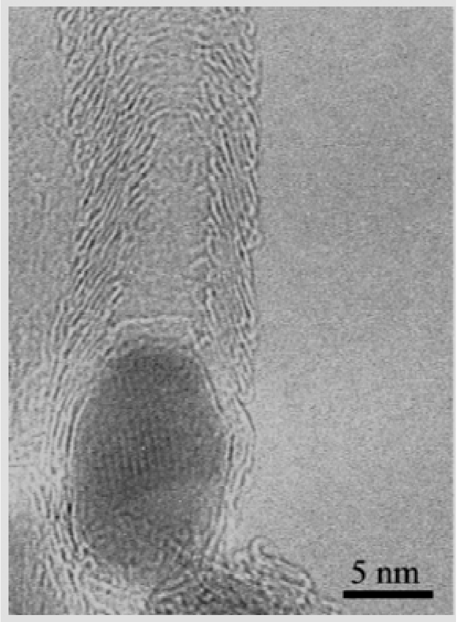

Figure 3. Transmission electron microscropy image of herringbone MWNT taken from reference [57]. The name is given to the layering of the graphitic planes because of the similarity to the stacking of a herring backbone. The dark colored spot in the bottom of the image is the catalyst particle.

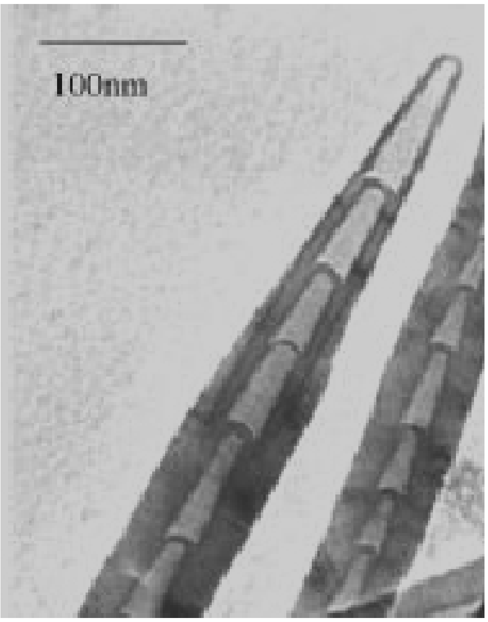

Figure 4. Transmission electron microscopy image of a bamboo type MWNT taken from reference [58]. The bamboo name is given to the carbon formation because of the similarity to the capsulated growth of bamboo shoots.

Bamboo type MWNTs, shown in Figure 4 are characterized by the growth of graphines perpendicular to the central nanotube axis. This type of growth creates pockets within the nanotube similar to that of bamboo shoots. Properties of MWNTs will be discussed later in this chapter.

2.2 Synthesis Techniques

There exist many methods by which CNTs can be produced, including but not limited to chemical vapor deposition, arc discharge and laser ablation. These three techniques are the focus of this section as they are some of the most common in research and industrial manufacturing environments. One of the major challenges facing the CNT industrial and research communities is to find a synthesis technique that yields CNTs of a specified or uniform chirality. Currently, researchers are relying on techniques that separate metal and semiconducting CNTs through sophisticated sonication and electrophoresis type processes.

2.2.1 Chemical Vapor Deposition

Chemical vapor deposition (CVD) is a synthesis technique that has existed for many years and is capable of depositing a number of materials. While the CVD method has been used since the 1960's to produce carbon filaments and fibers, it was not until the early 1990's that it was capable of producing CNTs. There are many types of CVD that can be used in the manufacture of CNTs, but the predominant types are thermal and plasma enhanced. Although the two methods are similar, this section with focus primarily on thermal chemical vapor deposition (t-CVD) as it was employed in the experimental setup.

Thermal chemical vapor deposition relies on thermal decomposition, or cracking, of carbonaceous gas molecules to introduce carbon into the vapor-liquid-solid (VLS) growth mechanism that subsequently forms CNTs. The VLS synthesis mechanism can be used in the synthesis of many types of one dimensional nanostructures and generally consists of the three primary steps of absorption, saturation, and structure extrusion. A low melting point metal, with the ability to absorb the desired gas species, is typically used as a catalyst in the VLS mechanism. In the synthesis of carbon nanotubes, transition type metals such as iron, nickel, and molybdenum are used as catalyst for their ability to absorb carbon. The metal catalyst can be introduced via solution, evaporation or sputtering onto the synthesis substrate or into the synthesis chamber. The carbon source in t-CVD is most often carbonaceous gases including methane, acetyelene and ethylene, but can also include vaporized carbon feedstocks such as toluene. The process of the VLS growth mechanism is shown in Figure 5.

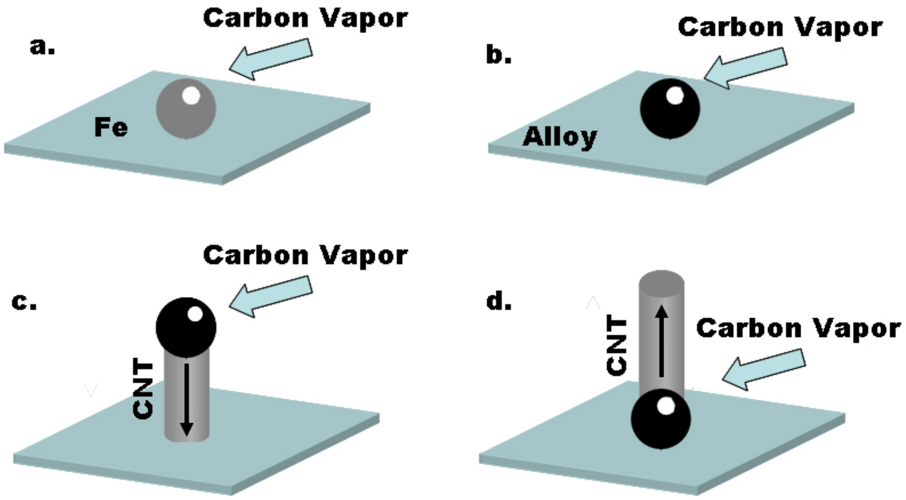

Figure 5. Various stages of vapor-liquid-solid (VLS) growth mechanism. Catalyst particle in molten state absorbs carbon in vapor form (a) to form an alloy (b). As the particle becomes saturated with carbon, a solid CNT begins to extrude from the particle. The final location of the catalyst particle defines tip grown (c) or root grown (d) CNTs.

The VLS process is energized by heat, which forces the metal catalyst into a molten state and also begins cracking the carbonaceous gases. Once gas decomposition has started, the carbon species begin to diffuse into the catalyst to form an alloy, shown in Figure 5(b). As more and more carbon elements are incorporated into the catalyst, the concentration of carbon exceeds the solubility of the catalyst particle. At this point, the catalyst particle beings to extrude a solid formation in the form of a CNT as seen in Figure 5(c,d). Depending on the final location of the catalyst particle, the nanotube is typically classified as either tip grown or root grown. The VLS growth of a germanium nanowire from a gold nanoparticle is shown in Figure 6 (a-g) and the growth of multiple nanowires is shown in Figure 6(h-i).

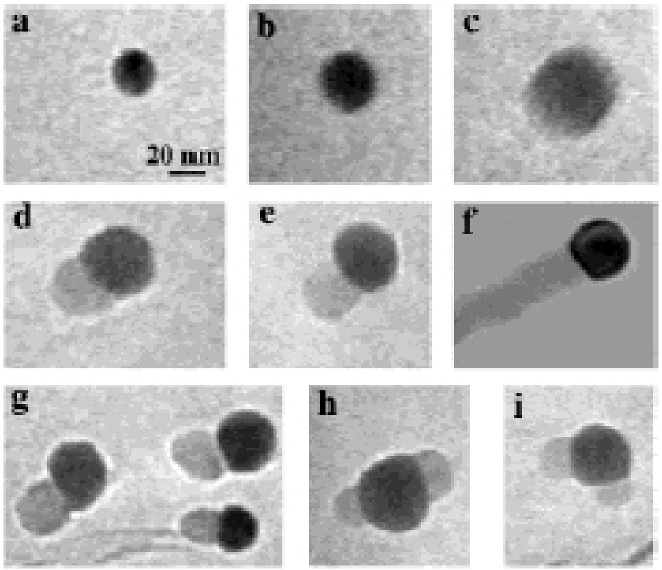

Figure 6. Formation of germanium nanowires from gold nanoparticles via the vapor-liquid-solid growth mechanism [59]. These transmission electron microscopy images reveal the extrusion of the germanium nanowires (c-i) from the saturated particle (b).

The major benefit to using CVD for the synthesis of CNTs lies in its ability to be scaled up in size, allowing the largest production facilities to produce several kilograms per day. The typical t-CVD setup includes a durable, high temperature compatible tube, usually of quartz or alumina, which is heated by a box furnace or heating coils. Carbon gases are channeled into the heated reactor zone via mass flow controllers and the eventual byproducts are evacuated through a fume hood. The t-CVD method allows for the production of both SWNTs and MWNTs.

2.2.2 Arc Discharge

The arc discharge CNT synthesis method relies upon the vaporization of carbon in the presence of catalyst (iron, nickel, cobalt, molybdenum) while under a vacuum of inert gas such as argon or helium. The vital components inside of an electric arc chamber are the two graphite rods that provide the arc necessary for synthesis. After creating an arc between these two rods, plasma is formed consisting of a mixture of carbon vapor, catalyst vapor and the inert gas. The two millimeter diameter rods are spaced a few millimeters apart as shown in Figure 7 and typical arc power settings are an arc current of 80 amps and a generating voltage of 60 kilovolts.

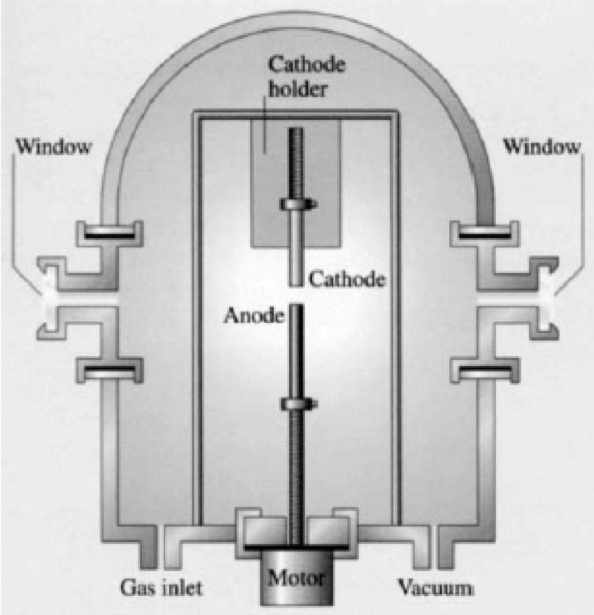

Figure 7. Arc discharge synthesis chamber, image taken from reference [52]. Critical components of the synthesis chamber include the anode and cathode graphite rods, vaccum port and gas inlet. An electrical arc creates a synthesis plasma between the rods.

The catalyst is typically introduced into this reaction via the anode in two predominant methods, drilled hole or uniformly dispersed. By the drilling method, a several centimeter hole is drilled into the end of the anode graphite rod and filled with the catalyst and graphite powder. The other type of anode has the catalyst uniformly dispersed within the rod and is easier to fabricate.

2.2.3 Laser Ablation

The CNT synthesis method of laser ablation is somewhat similar to arc discharge, in that both methods rely on the evaporization of solid graphite. While arc discharge relied upon a high voltage arc to create plasma, laser ablation utilizes a laser to add radiation energy to the synthesis reaction. Typically, a graphite pellet doped with a catalytic metal is placed inside the heated reaction zone of a furnace at around 1200 °C [60]. A laser is then directed onto the pellet in a pulsed or steady fashion causing the vaporization of the metal and graphite. The metal is often slower to sublime than the graphite, causing the synthesis reaction rate to gradually slow over time as the pellet becomes more and more metallic. The heated vapors combine and are deposited onto a cooled copper surface as seen in Figure 8 below.

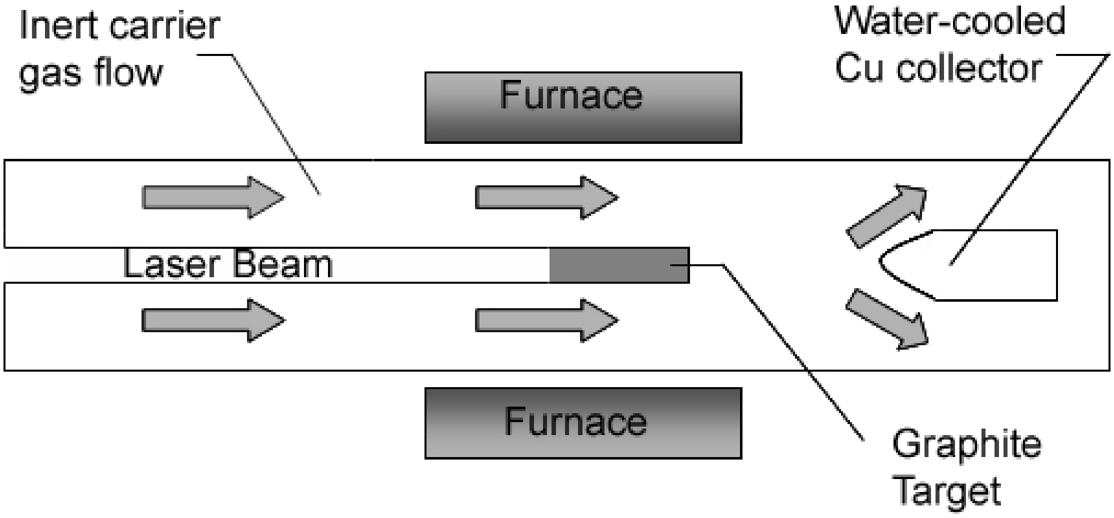

Figure 8. Laser ablation setup, adapted from reference [60]. Laser heating in addition to the elevated ambient from the furnace causes the graphite target to evaporate. Carbon nanotubes are collected downstream on the water cooled copper collector.

It should be noted that both laser ablation and arch discharge produce byproducts, including soot and amorphous carbon, in addition to SWNTs and MWNTs and must therefore always be purified post situ. The CNTs produced via laser ablation and arch discharge are generally of a higher quality than thermally produced CVD materials. The extreme temperatures generated during synthesis may help to anneal defects from the CNTs.

The growth mechanism driving laser ablation and arc discharge are similar in character because both methods involve the vaporization of large carbon deposits and subsequent condensation. While the precise workings of the mechanism are not fully understood [61], it is known that the laser ablation and arc discharge growth mechanism is similar to the VLS mechanism of thermal CVD. One hypothesis of the growth mechanism, supported by experimental study [61], suggests that CNTs form during the cooling of stages of the synthesis process. At first the graphite target and catalyst particles are vaporized by either the laser or electrical arc, creating a very hot plume of vapor that quickly expands and cools. Large carbon clusters are formed as the vaporized carbon species begin to cool. As the catalyst cools, but more slowly at first, they begin to attach to the carbon clusters. Nanotubes form from these carbon-catalyst clusters until either the catalyst particle has become too large or until synthesis conditions have cooled and do not allow the carbon to diffuse in or onto the catalyst particles [61]. The chart shown below details the three synthesis methods.

Table 2. Comparison of CNT synthesis techniques.

	Thermal CVD	**Laser Ablation**	**Arc Discharge**
Growth Mechanism	VLS	VLS	VLS
Process Temperatures	500-1000 °C	3000-4000 °C	
Carbon Source	Carbon gases or liquid	Solid Carbon	
Catalyst Source	Particles or thin films	Particles	
CNT surface or collector	High temp. compatible substrate	Copper collector	Carbon rod
Diameter Control	Large distribution	Small distribution	
CNT Relative Defectiveness	High	Low	
Nanostructure Arrangement	Yes, vertical alignment possible	No, randomly arranged	

2.3 Properties

While CNTs have a number of enhanced material properties over their bulk counterpart of pure carbon, the focus of this section is the mechanical properties and electrical transport properties.

2.3.1 Mechanical Properties

CNTs have a strength to weight ratio higher than that of steel. The reason for the strength of CNTs in the axial direction is the sp^2 bonds within the graphite sheets. In previous experimental research, the Young's modulus of near perfect SWNTs in the axial direction has been estimated at 1 TPa [3]. In another study of CVD produced MWNTs the tensile strength was measured to be lower than 100 GPa. Reasons for differences between such estimates and measurements include point defects within the graphite planes and a misalignment of the graphitic planes with regard to the central axis. Nano-scale point defects should intuitively have a greater impact on nanotube sized features, versus their micro and macro sized fibers. Other more recent research, however has suggested that point and planar defects can act to strengthen MWNTs as they are strained in the axial direction [62].

There are several methods available to measure the mechanical properties of CNTs, including bulk material analysis, resonance measurements, and microsystems tooling measurements. Due to their high tensile strength and low density, CNTs have been viewed as an excellent choice for composite filling [63]. If sufficient knowledge of the alignment and volume fraction of the CNT filler is present, it is possible to back-solve for the average tensile strength of the CNTs. This method however, is not the best for obtaining mechanical property information from individual CNTs, due to uncertainties in the CNT dispersion and directional alignment. Another method for estimating mechanical properties of CNTs involves observing the amplitude of their thermal vibration and backsolving for parameters using beam theory [3]. This measurement is performed inside a scanning electron microscope (SEM) chamber while elevating the ambient temperature of the CNT sample. Although this measurement isolates individual CNTs, it requires the use of thermal vibration theory to extrapolate a material property. A third method of measuring the mechanical strength of CNTs is to use a micromanipulator tool such as an atomic force microscope probe. In this method, a CNT is mechanically attached to the sharpened tip at the end of a sensing MEMS cantilever. The other end of the CNT is then rigidly adhered to a surface using an epoxy or binder and a pulling, tensile force is then placed on the CNT. By noting the cantilever deflection and knowing the cantilever spring constant, it is possible to calculate the stress and strain being place on the CNT and hence make a calculation regarding its strength in the tensile direction [62].

2.3.2 Electrical Transport Properties

SWNTs can be either semiconducting or metallic depending on the chiral vector as depicted previously in Figure 1. Studies have shown that for given chiral vector directions, the electrical properties of the SWNT can be predicted. If the difference of the vector integers, given by *n-m,* is a multiple of three, then the nanotube is metallic. Otherwise the electrical behavior of the tube will be semiconducting. The subsequent electrical behavior resulting from these integer combinations is shown in Figure 9 below.

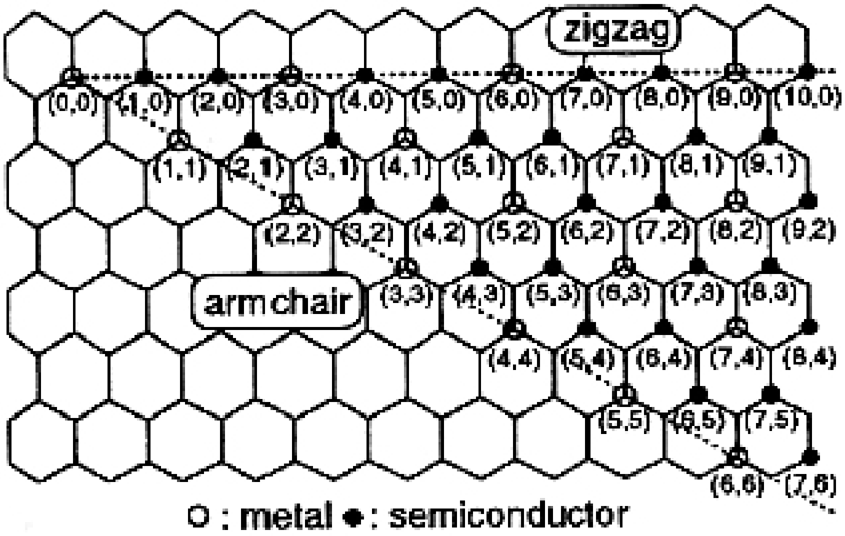

Figure 9. Conductivity roadmap for single walled carbon nanotubes indicating the conductivity of the nanotube produced with a chiral vector of given (n,m) integers. Multiwalled nanotubes tend to be metallic due to the low likelihood of all semiconducting nested nanotubes.

Shown in Figure 9, the chiral vector integer pairs that produce metallic CNTs are represented as hollow circles, while semiconducting CNT producing pairs are shown as dark circles. The 1-D structure of CNTs is associated with a specific type of band structure that can give rise to unusual electrical transport properties. Due to the 1-D nature of their band structure, SWNTs exhibit peaks or spikes in their density of state (DOS) diagrams as shown below in Figure 10.

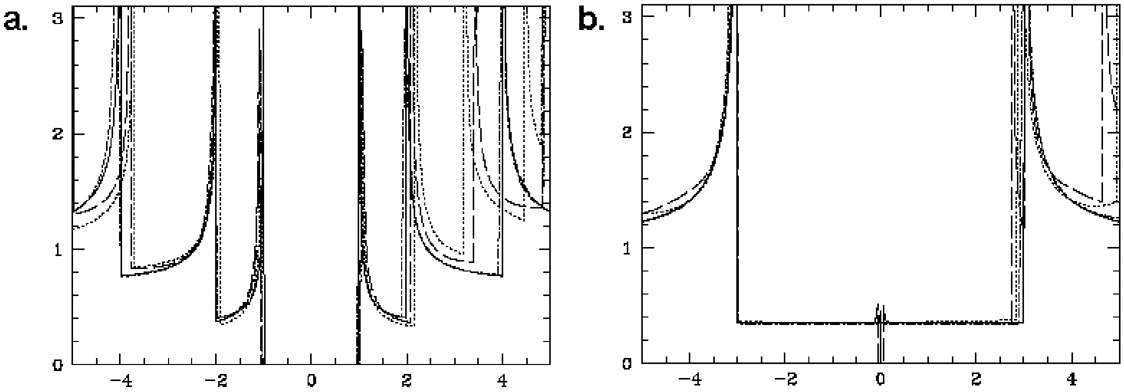

Figure 10. Density of states diagrams for a semiconducting CNT (a) and a metallic CNT (b) taken from reference [64]. The spikes in the figure represent energy levels at which electrons tend to exist and are called van Hove singularities. The metallic tube (b) can readily move electrons between the two lowest energy levels. The energy band gap seen in (a) between the lowest level states is indicative of a semiconducting tube (a).

The DOS diagrams shown in Figure 10(a,b) are representative of semiconducting and metallic CNTs respectively. The peaks in the DOS diagrams are called van Hove singularities and are representative of the energy levels where the electrons tend to exist in the orbitals. One distinguishing difference between the semiconducting and the metallic DOS diagrams are that electrons can exist at zero energy. In the outer singularities of the semiconducting tube, there exists a need to transition between peaks, as opposed to the metallic tube where electrons can move more readily. The band gaps between the van Hove singularities seen in Figure 10 can be estimated using the theoretical prediction,

$$E = \frac{k a_{c-c} \gamma_o}{d}$$

In this relation, E is the transition energy, $a_{c\text{-}c}$ is the nearest-neighbor carbon-carbon distance, 0.144 nm, γ_o is the nearest-neighbor carbon-carbon interaction energy, 2.9 eV [65], d is the SWNT diameter and k is an integer constant. The values of k can be 2, 4 and 8 for the 1st, 2nd and 3rd van Hove singularities in semiconducting tubes and 6 and 12 for the 1st and 2nd van Hove transitions in metallic tubes respectively [66]. The ability to create SWNTs in large quantities with a common chirality and electrical properties is still the largest problem faced in the CNT synthesis field.

The electrical and mechanical properties of CNTs are summarized in the following Table 3.

Table 3. Physical properties of single and multiwalled CNTs

Physical Property	**SWNT**	**MWNT**
Tensile Strength (GPa)	50-200 [67] 3.6-22.2 [68]	11-63 [69] 6.2-22.2 [4]
Young's Modulus (GPa)	1000 [67] $1300\pm^{600}_{400}$ [70]	270-950 [69] 690-1870 [4]
Current Density (A/cm^2)	10^7–10^8 [71]	10^9 [72]
Electrical Conductivity (S/m)	$1x10^6$ [9]	1/13 [72]

2.4 Microsystems Applications

Carbon nanotubes have been employed in several microsystems applications to date including electronic circuits, field emission devices and bulk material reinforcement. According to Moore's law as first stated in 1965, the number of transistors in an integrated circuit (IC) will double every 18 months. The semiconductor industry has relied upon the miniaturization of transistor gate lengths to enable a greater transistor density and also allow ICs to run at faster speeds. One major problem that the high density of transistors creates, however, is the buildup of large heat fluxes. This has lead semiconductor manufacturers and research groups worldwide on a search for alternative materials to silicon. In response to this, IBM has recently demonstrated a 12 transistor ring oscillator can be fabricated onto the side of an individual CNT [73]. An image of the 18 μm long circuit is seen below in Figure 11 with a detail image showing the CNT.

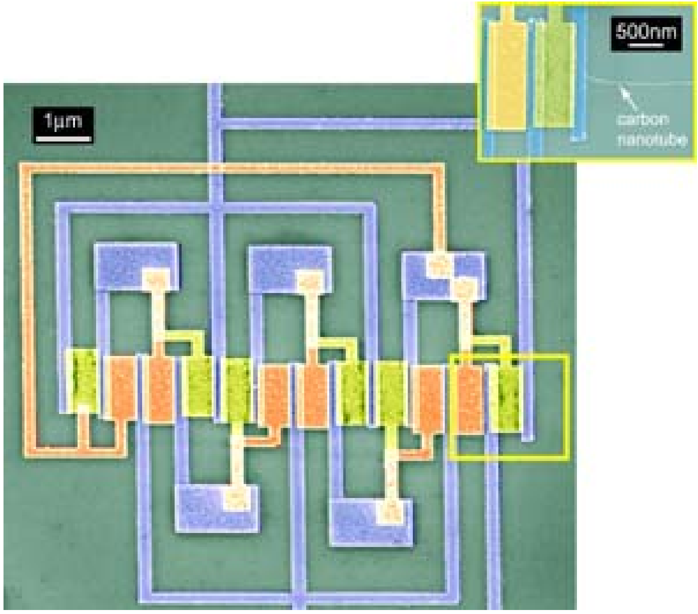

Figure 11. IBM produced ring oscillator consisting of 12 transistors built onto the side of an individual CNT [73]. The arrangement of the device allows it to test the speed at which the CNT based transistors are capable of switching.

IBM previously had published work demonstrating a functional logic circuit comprised almost entirely of CNTs. This recently fabricated ring oscillator allows researchers to test the switching speed of the fabricated transistors, made from palladium and aluminum. This is just one promising application of CNTs that may grow in popularity as transistor dimensions continue to miniaturize.

Another application of CNTs is their use as a field emission display material in displays and monitors. Samsung has developed a 38 inch working prototype model and in Austin, Texas based Applied Nanotech has developed a 22 inch model. The prototype nanotube emission display (NED) as seen below in Figure 12 was made by Motorola Labs [74].

Figure 12. Nanotube emitting display made by Motorola Labs [74]. The use of CNTs as field emitters has the potential to make display panels millimeters thin and economical to manufacture.

The 5 inch diagonal display is made by growing CNTs directly onto glass versus other application methods such as pasting or printing of CNTs. The display panel is only 4 mm thick and inexpensive to manufacture, such that Motorola estimates that a 40 inch display could be made for less than $400. In a conventional cathode ray television, an electron gun fires electrons at a phosphor-coated glass divided into pinpoints to create images. The electrons, however, need to disperse in a large vacuum tube, which is why TV tubes are so large and bulky. In a field emission display (FED) television, generated electrons are filtered into an array of thousands of tips only a few nanometers wide. When these electrons are delivered to the screen, the television has the ability to be much thinner. One reason why CNTs are good field emitters are because of their high aspect ratios which enhances the electric field at their tips. If CNT based field emission displays continue to be improved, they can be expected on store shelves in the next 5 to 10 years.

The third application for CNTs is their use as a woven sheet like material as recently demonstrated by Prof. Ray Baughman at the University of Dallas Nanotech Institute [75]. The researchers start by first producing a large area of vertically aligned CNTs resembling a forest in structure. A simple piece of adhesive tape is then used to tease some of the CNTs away from the side of the forest. Under this pulling motion, the interactive forces between the millions of aligned nanotubes causes the next row of sequential nanotubes to become uprooted and self align into a fabric. The end result of this process is a sheet of nanotubes only 50 nm thick, 3.5 cm wide and several meters in length. The sheets can be layered to create fabrics with very high tensilary strengths as shown below in Figure 13.

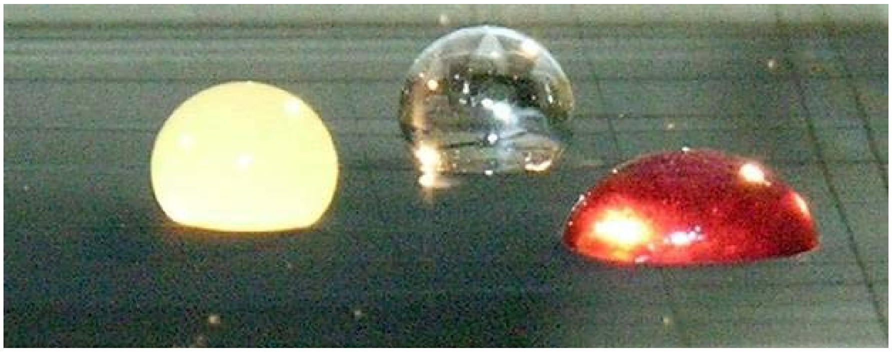

Figure 13. High tensile strength in CNT fabric is demonstrated as droplets of orange and cranberry juice and water are placed onto two stacked CNT sheets [75]. The droplets are roughly 50,000 times the mass of the two perpendicularly arranged CNT fabrics.

The droplets of orange juice, grape juice and water shown in Figure 13 are roughly 50,000 times the mass of the two perpendicularly aligned CNT sheets that support them. The CNT based fabric has a strength to weight ratio greater than Mylar and Kapton and can be produced at rates upward of 7 meters per minute. The sheets are capable of conducting electricity and emitting both light and heat when charged with an activation voltage. Sample uses for this transparent film material includes embedded sensors between glass surfaces, electrical heaters for defrost, or informative optical displays.

In summary, the simple structuring of carbon in CNTs gives rise to their extraordinary mechanical and electrical properties. There exists a multitude of methods by which CNTs can be produced and characterized. Depending upon the number of nested inner tubes, CNTs can either be singlewalled or multiwalled, each with its own characteristics and properties. These properties have propelled CNT researchers and industry to investigate future CNT microsystem applications.

CHAPTER III: NANOTUBE GROWTH TECHNIQUES

3.1 Global CVD

This section discusses the carbon nanotube synthesis techniques designed to allow for secondary microsystems applications and for direct microsystem integration.

3.1.1 Experimental Setup & Methods

The CNT synthesis setup that was employed in this experiment was thermal chemical vapor deposition relying on the VLS growth mechanism. The global CNT synthesis setup was purchased from CVD Equipment and features a 2” quartz tube heated by resistive heating coils contained within a box furnace as shown in Figure 14.

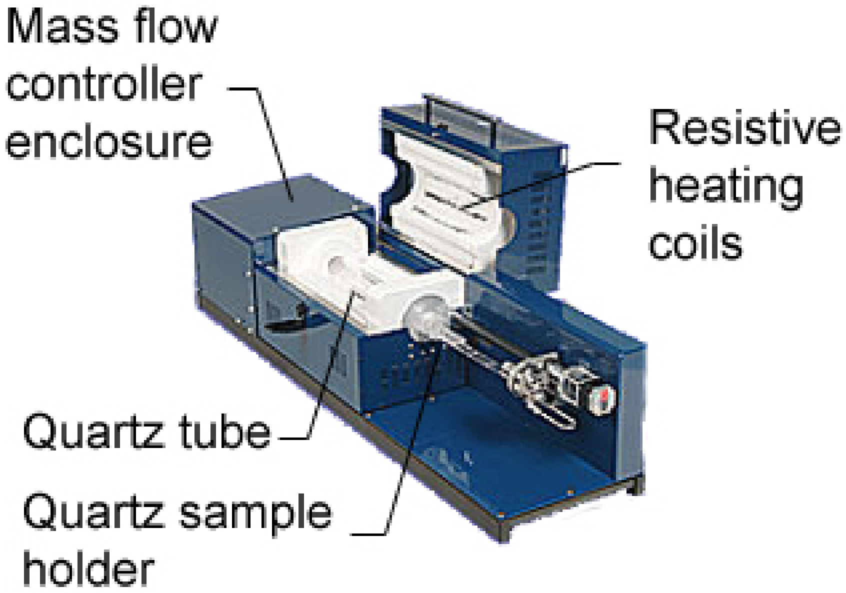

Figure 14. Easytube 1000 series tube furnace featuring a 5cm diameter quartz tube, automatic sample loader and 4 separate programmable mass flow controllers.

Gas and temperature recipes were programmed and saved into a control PC running a Labview based furnace control software. The control software had the ability to ramp up, maintain and cool to desired temperatures, while simultaneously controlling up to four mass flow controllers. The mass flow controllers released gasses into a main header before entering the quartz tube. The typical carbonaceous gasses used in the CVD setup were methane, ethylene and acetylene. Studies have shown that methane will only completely decompose in the process if the kinetic energy is sufficiently high (≥900 °C) [76]. Ethylene and acetylene are considered more reactive carbon sources as they decompose at lower temperatures [77]. The rate at which carbon is dissociated from the gas species will help dictate the resultant growth, as SWNT growth needs a low carbon supply rate [78]. Argon was introduced as a purge gas and hydrogen was used as a carrier and diluting gas. The process gases were exhausted out of the other end of the system and pulled away by a ventilation system, thus maintaining a pressure close to atmosphere.

The preparation of metal catalyst was an important step in the successful synthesis of CNTs via this method. Catalyst was introduced into the reaction via either particles in solution or evaporated thin films. Both of these methods utilized silicon as the base growth substrate. Silicon was chosen for the substrate material because it is capable of withstanding very high synthesis temperatures and is relatively inexpensive and durable.

In the method of particles in solution, iron and nickel nanoparticles, purchased commercially from Accumet Materials with an average diameter of 45 and 65 nm respectively, were dispersed in methanol. Particles were then pipette transferred onto a silicon substrate, which was then placed into a box furnace at 150 °C to evaporate the solvent, leaving the particles behind. The silicon substrate was only encapsulated by its native inherent oxide. The pipette method of catalyst introduction did not achieve good dispersion of catalyst across the surface of the substrate and was likely due to an elevated particle concentration. Under inspection with a microscope, it was evident that the nanoparticles were forming microscale clusters.

The second method of catalyst introduction involved thermally evaporating a thin film of iron catalyst onto the wafer in a clean room environment. Via this method, a wafer was first blown clean with nitrogen and then placed inside a plasma enhanced CVD chamber for processing. Typically a uniform 200 nm silicon dioxide layer was deposited onto the native wafer oxide. The base oxide layer acted as a support layer for the subsequent metal catalyst layers. The deposition of a sufficiently thick film of silicon dioxide was an important step. The oxide film performed two functions in the synthesis process by acting as a protective buffer layer and aiding in the formation of CNT nucleation sites. Previous studies have shown that reaction damaging iron and nickel silicides can form without the use of a silicon dioxide buffer layer [79]. The surface roughness of the silicon dioxide, as opposed to the near planar bare silicon, also favors the breakup of the thin catalyst film.

After the initial oxide deposition, catalyst metal layers were evaporated onto the surface of the wafer if a blanket film of catalyst was desired. In other cases, standard microelectronic photolithography was used to pattern photoresist to allow for the deposition of 2D catalyst shapes. A subsequent liftoff process in acetone would then remove the photoresist, leaving patterned metal behind on the wafer. During the liftoff process, the iron evaporated on top of photoresist would be lifted while the metal deposited in the feature wells would remain. Following liftoff, a descumming exposure to oxygen plasma was performed for 30 seconds to remove any residual photoresist around the feature edges. A number of metal catalysts were then deposited onto the substrates to allow for CNT growth, including iron, titanium-iron, nickel, and aluminum-iron. The metal evaporation could be done via two different methods: electron beam evaporation and thermal evaporation. Electron beam evaporation relies on a variable power, heating laser to melt and evaporate metal pellet in a ceramic crucible. Thermal evaporation relies upon a resistively heated boat to melt and evaporate metal flakes below a spinning sample holder. While both methods will evaporate the desired metals, electron beam evaporation offers better control of the deposition rate and also gives better line-of-sight deposition directionality. Following metal deposition, both patterned and unpatterned catalyst wafers were diced into manageable coupons typically 1 cm^2 that could fit within the tube furnace.

To investigate the output capabilities of the CVD setup with our various catalysts, process recipes were written and saved to the furnace control computer. The process recipe used in the parametric study involving iron and nickel nanoparticles for CNT synthesis is shown below in Table 4. The temperatures at which synthesis was performed include 500, 600, 700, 750, 800, 850 and 900 °C. The four primary steps of the synthesis process included the initial purge, the temperature rise and stabilization, the synthesis soak period, and finally the cooling of the reaction chamber. In the initial purge step, 10 liters/minute of argon was used to purge all air from the tube. In the second step, the temperature rose and was allowed to equilibrate at the desired synthesis temperature under a lower flow of argon. The third step was the synthesis period in which CNTs are created under constant temperature and gas flow rates. The duration of the third step was found to be roughly correlated to the final length of the nanostructures. As shown in the third step of Table 4, ethylene or acetylene only comprised 12% of the gases released during the reaction due to their high reactivity [77]. The last step of the process involved purging the growth gases from the tube and allowing the heating chamber to return to room temperature.

Table 4. Process recipe for iron and nickel nanoparticle catalyst.

Step	Name	Gas Flows (sccm)	Temperature (°C)	Duration (min)
1	Purge	10,000 Argon	0	.5
2	Rise & Stabilize	500 Argon	23 → 500:900	15
3	Soak	1000 Methane 500 Hydrogen 100 Ethylene or Acetylene	500:900	10
4	Cool	500 Argon	740 → 23	180

While the parametric study on catalyst nanoparticles covered a wide temperature range, almost all thin film recipe synthesis trials were performed around 700-740 °C. The recipe used to evaluate thin film catalysts had four primary steps as shown below in Table 5. The thin film process recipe was typically altered by switching ethylene with acetylene and also by changing the duration of the soak step. The thin film recipe was very similar to the particle catalyst recipe in its major steps.

Table 5. Process recipe for thin film catalyst.

Step	Name	Gas Flows (sccm)	Temperature (°C)	Duration (min)
1	Purge	10,000 Argon	0	.5
2	Rise & Stabilize	500 Argon	23 → 720±20	15
3	Soak	1000 Methane 500 Hydrogen 100 Ethylene or Acetylene	720±20	1-20
4	Cool	500 Argon	740 → 23	180

To sample the diameters of the produced nanomaterials, SEM images were analyzed using an image processing software called Metamorph. A pixel based measurement was made of each focused CNT and compared to the scale bar of the image to determine the diameter. An average CNT diameter could then be generated for each synthesis temperature group of images. The image shown below in Figure 15, displays a group of approximately 25 sample measurements that have been collected from a SEM image.

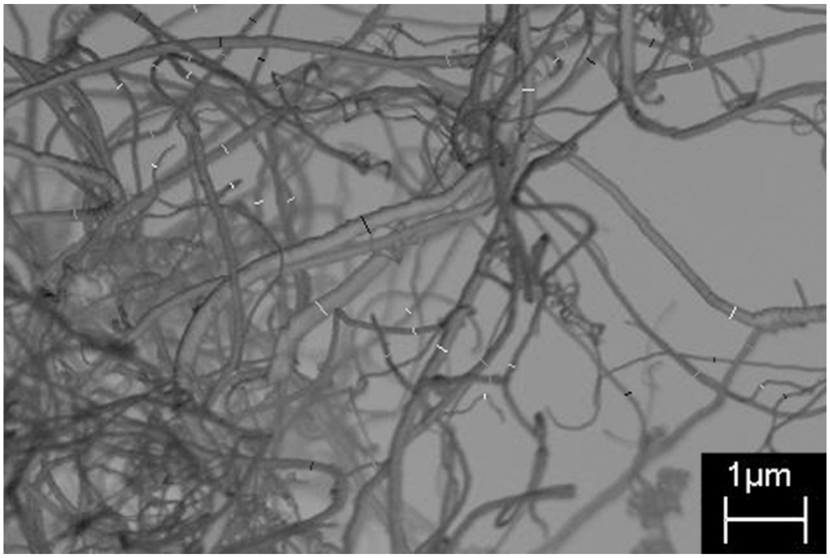

Figure 15. Sample diameter measurements of CNTs, created at 800 °C with iron nanoparticles in solution, taken using Metamorph image processing software. The image colors have been inverted to more easily see the measurement marks.

3.1.2 Experimental Results

CNT Synthesis via Iron and Nickel Nanoparticles

The following results were obtained by studying the output possibilities of a thermal CVD chamber using the varied synthesis parameters mentioned previously. Varying synthesis temperature and one of the gaseous carbon sources between ethylene and acetylene resulted in a large distribution of average diameters for both the iron and nickel catalyst as seen in Figure 16. The flow of methane and hydrogen was always left constant throughout the synthesis soak period. The diameter of the CNT structures varied with temperature, showing an increase in average diameter and also an increase in the variance of diameters produced. When using ethylene precursor gas, the average diameter was more varied between each of the three data sets than the acetylene/methane combination. Between 500-700 °C, ethylene produced features with an average diameter of 36 nm and a standard distribution of 15 nm. At higher temperatures between 750-900 °C, ethylene diameters increased between 50 nm and 90 nm respectively. The standard deviation in average diameter was also increased from 15.1 nm to 33.6 nm respectively. At lower temperatures, acetylene produced no growth at 500 °C and small diameter growth of 27.4 nm at 600 °C. As temperature was increased from 600-900 °C, acetylene produced diameters between 23.1 nm and 88.7 nm with standard deviations of 9.5 nm and 33.4 nm respectively. Both acetylene and ethylene gas showed a minimum in average diameter variance between 700-750 °C.

This experiment agrees with previous studies that have shown that increasing the synthesis temperature will result in larger catalyst nucleation sites, which yield larger diameter features [80, 81]. As 65 nm particles were only used in this trial, particle size does not seem to be a major determining factor in CNT diameter as reported elsewhere [18]. It should be noted however, that smaller diameter particles (~5 nm) were used elsewhere. One explanation for the large diameter features seen at higher temperatures is that the molten aggregated catalyst particles are combining to form larger particles. A final note that can be taken from Figure 16 is that the ethylene produced CNT diameters show less repeatability in comparison to the acetylene based CNT diameters. The large deviation that occurs in one of the low temperature acetylene trial data points stems from a low count of CNTs produced on that given sample.

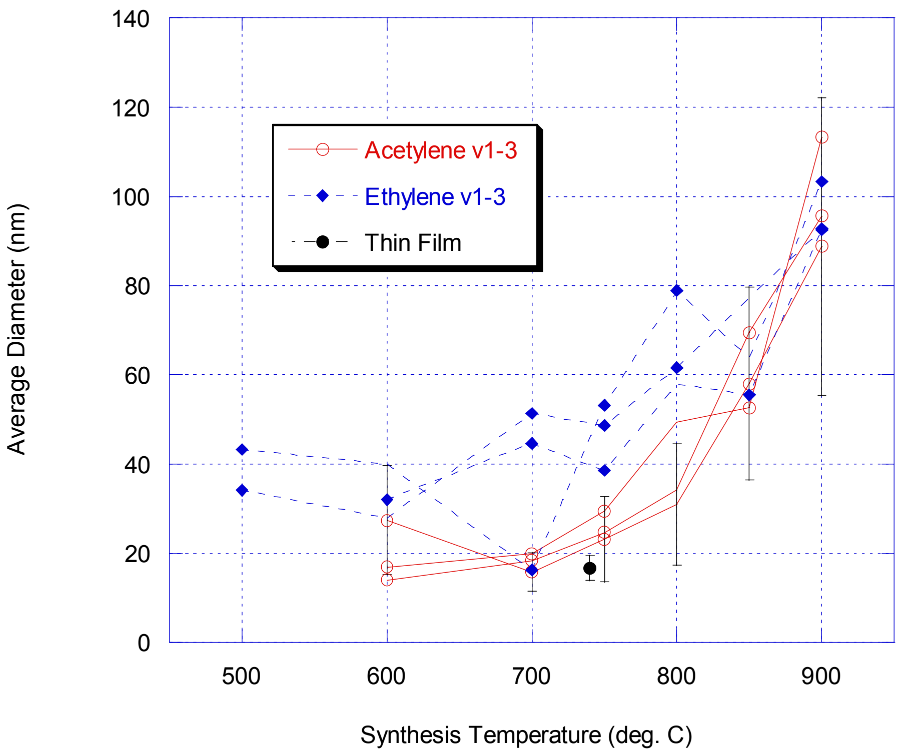

Figure 16: Iron catalyst MWNTs at varying synthesis temperatures, ethylene and acetylene gas flows compared. Sample error bars represent 1 standard deviation from a set of acetylene data and the thin film data point. Average mean diameter increases along with diameter standard deviation with elevated synthesis temperature. All the samples represented in this analysis were produced in synthesis periods of 10 minutes.

SEM images of CNTs produced on iron particle catalyst indicate that mostly carbon nanotubes were produced, with the only possible carbon fibers occurring at 600 °C and lower. The relatively lower synthesis temperatures between 500 and 600 °C produce very sparse growth and little nanotube production as evident by the small aspect ratios of materials produced. Nanofeatures with varied aspect ratios were produced at 500 °C and 900 °C as shown in Figure 17.

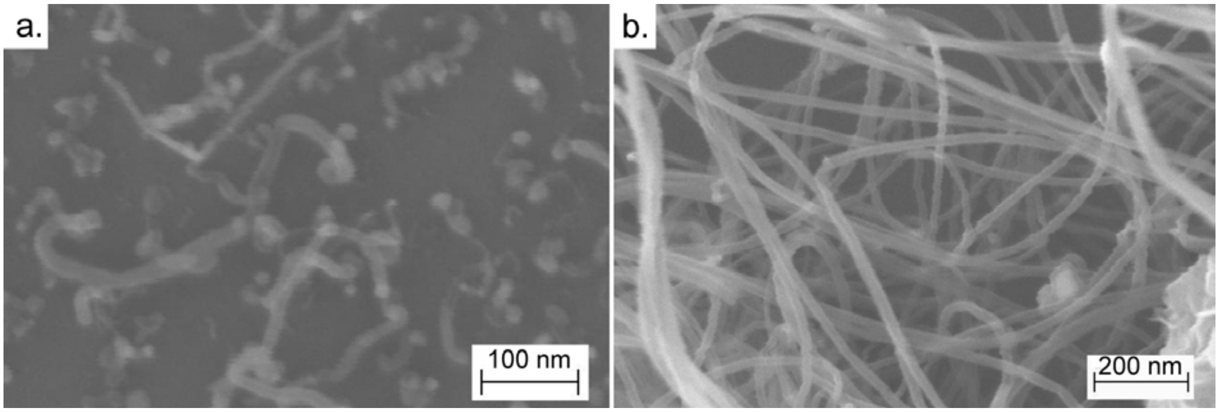

Figure 17. Comparison of low and high aspect ratio CNT growth on iron nanoparticles using acetylene, methane, and hydrogen at temperatures of 600 °C and 900 °C, respectively. Synthesis temperatures below 600 °C generally did not produce highly graphitic nanofeature growth.

As the temperature reached 700 °C, CNTs began to form and appear in greater abundance than the low temperature growth. The materials produced here showed little variation in average diameter and had larger aspect ratios. As the synthesis temperature was further increased, the abundance of CNTs continued to increase, but so did the presence of larger diameter tubules.

SEM analysis revealed that large diameter carbon fibers and carbon nanotubes were produced on the nickel catalyst. Using ethylene and methane precursor gasses at 500 and 600 °C resulted in a large quantity of carbon fibrils, with little nanotube production. As the synthesis temperature was raised to 700 °C, CNTs began to appear, and the large diameter fibers were not present. A significant amount of impurity carbon formed as well. At 800 °C, no CNTs or fibers were produced. SEM analysis showed only amorphous carbon impurities and nickel catalyst particles. Synthesis at 900 °C was similar to the lower temperature synthesis, with a mixture of nanotubes and fibers. The standard deviation in average diameter increased as synthesis temperature increased.

Using a mixture of acetylene and methane gas produced larger diameter carbon fibers and nanotubes than ethylene gas at corresponding temperatures. Additionally the standard deviation in average diameter was larger for the acetylene/methane mixture. Once again, a trend in decreasing diameter was seen as the temperature was increased from 500 to 750 °C.

In conclusion, both the nickel and iron nanoparticles form the smallest diameter structures between 700-750 °C. In both iron and nickel particles, the nanostructure growth appears less structured and has smaller aspect ratios at lower temperatures between 500-650 °C. The use of nickel catalyst at low temperature (500 °C) and acetylene gave rise to large amounts of coiled fibers, while the iron catalyst did not. As shown below in Figure 18, iron catalyst promoted CNT and CNF growth that looks more structured with less macroscopic sidewall defects. The SEM images shown in Figure 18 reveal differences in the structures produced at varied temperatures for both iron and nickel nanoparticles.

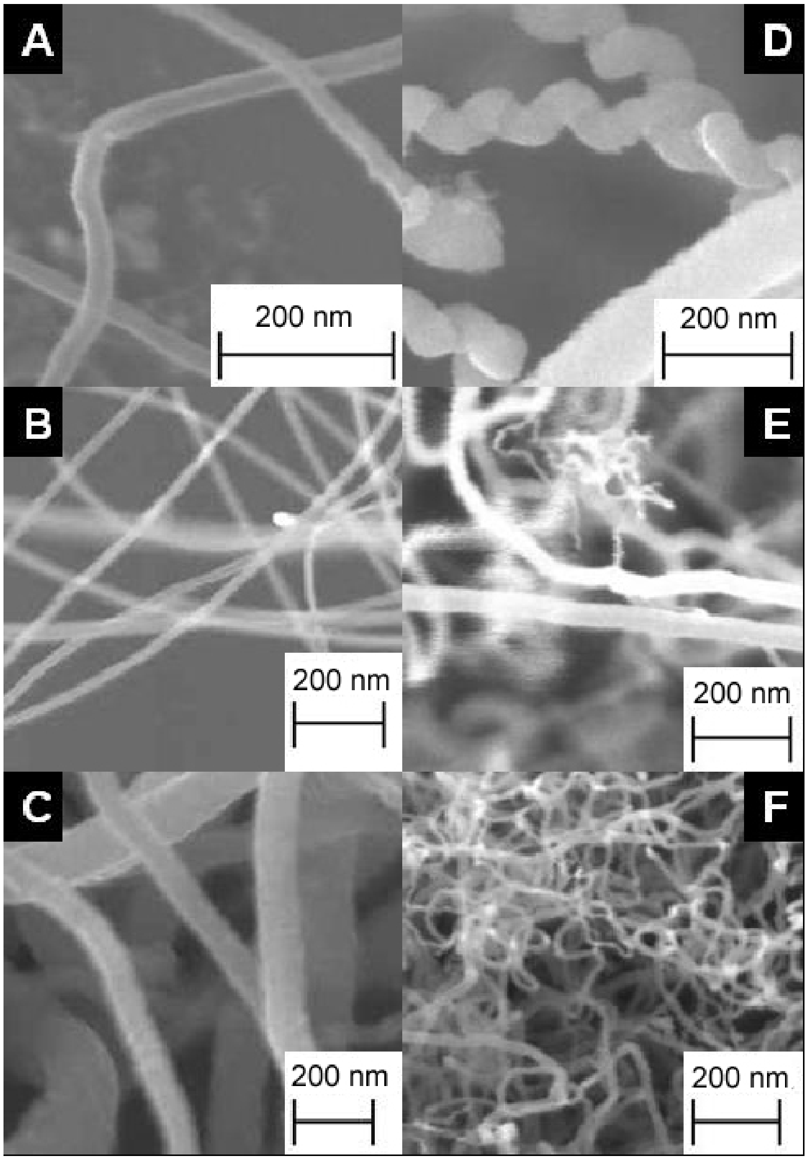

Figure 18: Typical SEM images of (a-c): Iron catalyzed CNTs produced at 600, 750, 900 °C respectively, (d-f): Nickel catalyzed materials produced at 500, 600, 700 °C. All these nanomaterials were created using the same acetylene/methane/hydrogen gas recipe as detailed above.

CNF Synthesis

Quantitatively, most of the fibers and nanotubes produced in the 500-600 °C range with nickel catalyst have a helical nature as seen above in Figure 18(d). While the use of acetylene versus ethylene gas did not seem to dictate a major difference in high temperature growth, the use of acetylene in combination with the low temperatures and nickel catalyst however, had a dramatic effect on the amount of helical nanostructures produced. The increased amount of helical CNFs can be seen below in Figure 19 where the relative amounts of helical nanofibers produced by acetylene and ethylene gas are compared. The application of a voltage (50V) to the furnace during synthesis was also shown to increase the percentage of helical tubes/fibers dramatically.

The increase in helical tubes due to acetylene was most likely due to a higher decomposition rate of the gas. Acetylene is less stable than both ethylene and methane at higher temperatures, and decomposes into active atoms very quickly. Due to the fast decomposition rates of the gas, more carbon atoms are readily available to nucleate and grow nanotubes and fibers. As the synthesis rate was increased, the number of point defects in the fiber sidewalls also increased which lead to coiling. The voltage which was applied to the furnace during synthesis further increased the decomposition rate of the acetylene, and thus the growth rate and coiling tendency also increased.

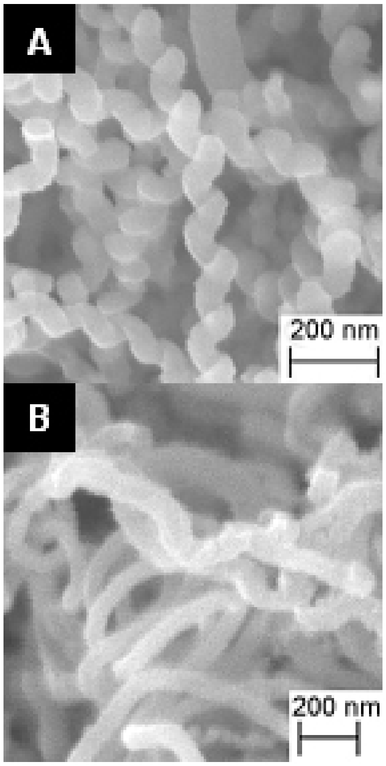

Figure 19. : Acetylene produced CNFs (a) Ethylene produced CNFs (b), both using nickel catlalyst at a synthesis temperature of 500 °C. The application of a 50V bias to the sample during synthesis proved to increase the amount of helical configured CNFs as seen in (a).

Evaporated Thin Film Catalyst

Also plotted in Figure 16, is an average diameter data point with standard deviation bars from a thin film catalyst produced CNT sample. This sample was created by evaporating 10 nm of iron onto a silicon wafer with a 200 nm thermally grown silicon dioxide layer. The synthesis trial was then performed using the CVD parameters as described above. The break-up of the thin film into catalyst particle “islands” takes place prior to the introduction of the carbonaceous gases during the temperature ramping in the presence of argon gas. The data point in Figure 16 at 740 °C reflects a smaller average diameter than most of the IPA-particle trials and also an improved variance. The low variance in the thin film catalyst data point was due to the uniformity and good dispersion of catalyst islands made possible by evaporating a precise thin film on top of a near planar surface.

Thin film catalyst was also more probable to produce macroscopically aligned CNTs as seen below in Figure 20(a,b). The vertical alignment mechanism was believed to result from the crowding of very densely spaced catalyst islands. The CNTs created at these nucleation sites crowd against neighboring CNTs and are pushed upwards in a crowding manner. While appearing to be perfectly vertically aligned from a macroscopic perspective, the individual CNTs actually appear wavelike and random. The alignment phenomenon has been observed in some cases with the particle in solution catalyst as seen in Figure 20(c), but occurs much more seldom.

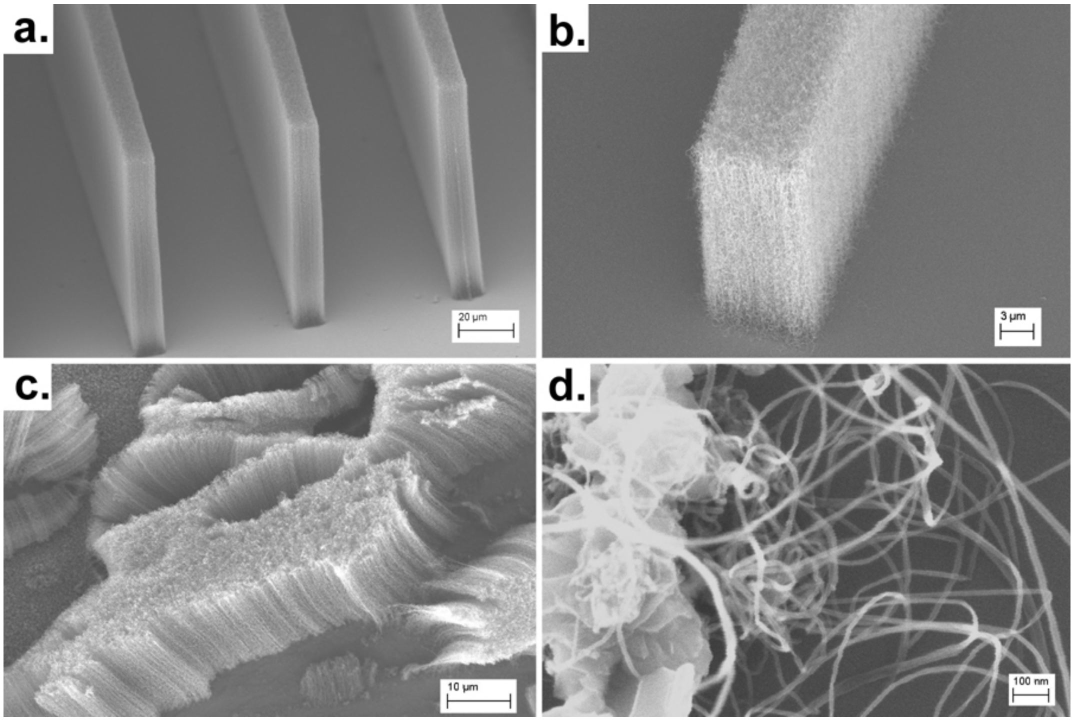

Figure 20. Alignment results of various catalysts. Evaporate thin film demonstrated the greatest probability to form vertically aligned features as seen in (a,b). Vertical alignment was also seen in some cases where particles in solution were spinning coated onto a substrate (c). Drip dispersing catalyst particles demonstrated only randomly arranged CNTs (d).

In the case of thin evaporated catalyst films, if the resultant CNT growth was greater than 10 μm then vertical alignment was almost guaranteed. In the case of particles in solution, however, the deposition method had a large impact on the probability of producing aligned CNTs. If the particles were simply dripped onto the substrate via a pipette, the resulting dispersion of the catalyst would be very poor and would lead to a random entanglement of the synthesized CNTs as seen in Figure 20(d). When the catalyst solution was spin coated onto the silicon wafer substrate and allowed to dry, the dispersion of the catalyst proved much better and resulted in pockets of aligned growth as seen in Figure 20(c).

The output synthesis possibilities were not investigated for the evaporated thin film catalyst as it was for the particles in solution catalyst. After reliable, well structured growth was found to be produced at temperatures of 700-740 °C using acetylene, methane and hydrogen, this recipe was used for the majority of subsequent thin film studies performed.

During experimentation, it was found that ethylene was less reactive than acetylene, thus providing a lower carbon flux and yielding slower CNT growth per synthesis minute. This discovery was implemented by altering the film recipe shown in Table 5. By flowing 700 sccm of ethylene over iron thin film catalyst at 700 °C, very short vertically aligned CNTs could be achieved. Using very short soak durations, short vertically aligned CNT growth could be achieved as shown below in Figure 21.

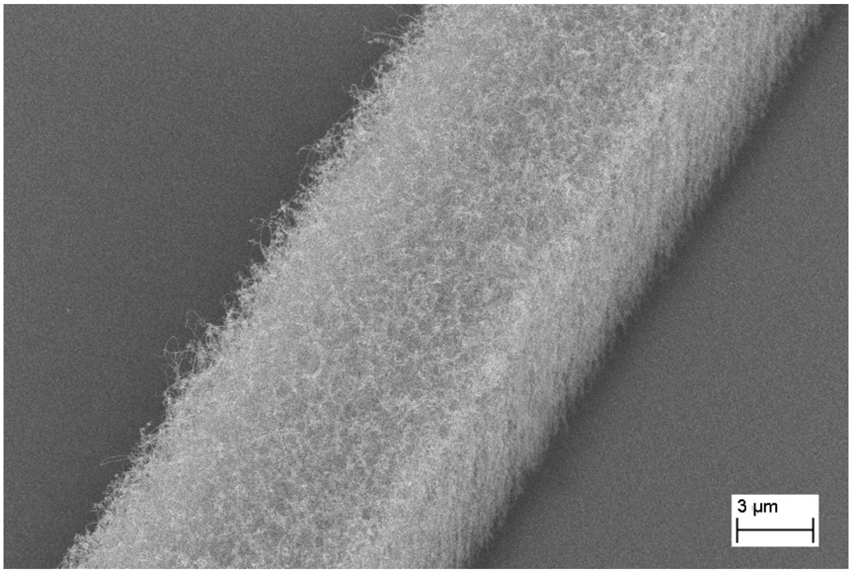

Figure 21. Short vertically aligned growth measuring 4-5 µm in height, caused by growth period conditions of 700 sccm ethylene at 700 °C for 2 minutes. At this temperature, ethylene provides little carbon to the synthesis reaction resulting in short growth and high control of the produced CNT height.

TEM Analysis

Imaging via TEM allowed for structural analysis, where upon it was determined that the quantities produced at temperatures over 700 °C were multiwall nanotubes (MWNT). TEM also revealed that the coiled materials produced at 500 °C appear to be amorphous in structure as seen below in Figure 22(a). Additional TEM imaging will be necessary to verify this claim. The MWNT quantities produced at the higher temperatures exhibit an increase in order with increase in temperature as seen below in Figure 22(b-c).

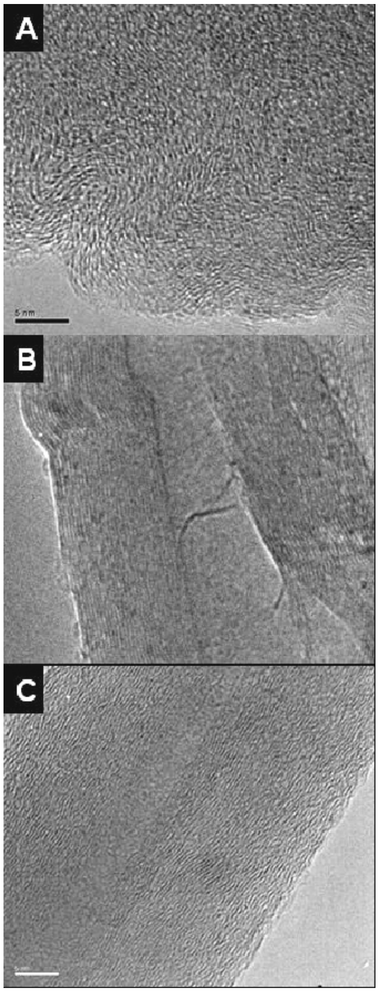

Figure 22. Transmission electron microscopy images of MWNTs produced with iron particles at (a) 500 °C (b)750 °C and (b)900 °C. The increase in graphitization with higher synthesis temperature is seen in images (b,c) as evidenced by their more pronounced sidewalls. The scale bar is equal to 5 nm.

Raman spectroscopy is a well known optical analysis technique that has the ability to provide a wealth of knowledge, including the ability to distinguish between semiconducting and metallic tubes and to determine the diameter and orientation of nanotubes [82-85]. The absence of the characteristic radial breathing mode (RBM) is further indication that the samples are lacking single wall nanotubes (SWNT) and are mostly comprised of MWNT. By the use of Raman spectroscopy, the relative intensities of the D band (1350-1365 cm^{-1}) and G band (1580-1620 cm^{-1}) can be compared to make a qualitative judgment of the defectiveness of the CNT materials produced [86, 87]. Measurements can be seen below in Figure 23, wherein the Raman scans of several different temperature synthesized samples are compared.

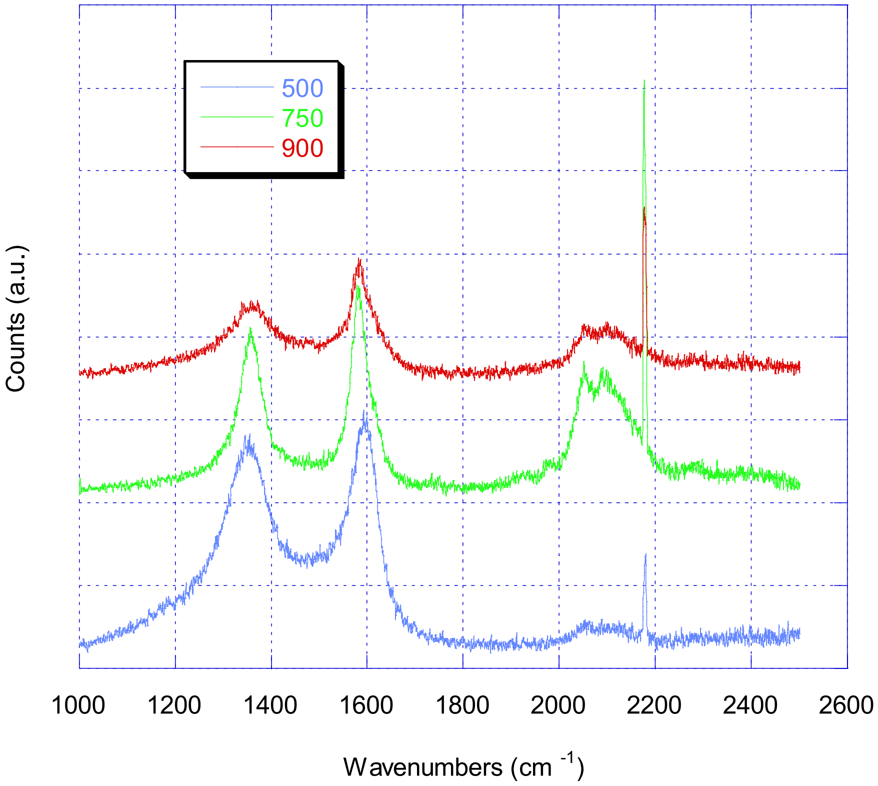

Figure 23. Raman spectroscopy scans of nanostructures produced at synthesis temperatures of 500 °C, 750 °C, and 900 °C using nanoparticle in solution based catalyst. The ratio of the defective band (1350-1365 cm^{-1}) over the graphitic band (1580-1620 cm^{-1}) is seen to decrease for each increase in synthesis temperature. This is supported by the transmission electron microscopy results shown above in Figure 22, that also indicate lower amounts of defects and greater graphitization at higher synthesis temperatures.

Shown in Table 6 below, the average intensity ratio was calculated from three different Raman scans for carbon nanomaterials synthesized at 3 different temperatures. The intensities of the peaks were found using a curve fitting software provided with the Renishaw brand Raman microscope. The I_d/I_g ratios collected indicated that as the synthesis temperature was raised to 700 °C and above, the defectiveness of the synthesized materials was reduced and the structure improved. This was supported by the more structured appearance of the graphitic planes in the high temperature materials seen in the TEM images in Figure 22(b,c).

Table 6. Intesity ratios of D-peak and G-peak from sample Raman scans for samples in Figure 22.

Synthesis Temperature (°C)	I_d/I_g	Avg. I_d/I_g
500	0.909	0.882
	0.873	
	0.864	
750	0.782	0.658
	0.658	
	0.535	
900	0.653	0.689
	0.734	
	0.681	

The difference in the intensity ratios between 750 °C and 900 °C did not improve with an increase in temperature, indicating that the structure did not significantly improve beyond 750 °C. This supports the minima in average diameter and variance for the CNTs produced around 700-740 °C as seen in Figure 16. Attempts were made experimentally through the process of thermal annealing to improve the I_d/I_g ratio of several CNT samples. Defects in the sidewalls of arc-grown CNTs can be removed by this process but generally require temperatures of at least 760 °C in air environment [88]. CNTs produced via thermal CVD however, have been shown to readily oxidize under these conditions. The inherent differences in structure and graphitization amongst different synthesized CNTs make it difficult to compare annealing possibilities in varied CNT materials. The Raman spectroscopy intensity ratios, I_d/I_g, shown in Table 6, are typical of unpurified thermal CVD grown CNTs.

3.2 Localized CVD for Direct Growth

3.2.1 Experimental Setup & Methods

In contrast to the global synthesis methods of section 3.1, localized synthesis of carbon nanotubes was investigated using a calibrated heated atomic force microscope cantilever made at Georgia Tech [89] and is pictured below in Figure 24. The heated cantilever demonstrates that localized microsystem heating can be used to synthesize CNTs as opposed to global exposure of the microsystem to the high temperature field.

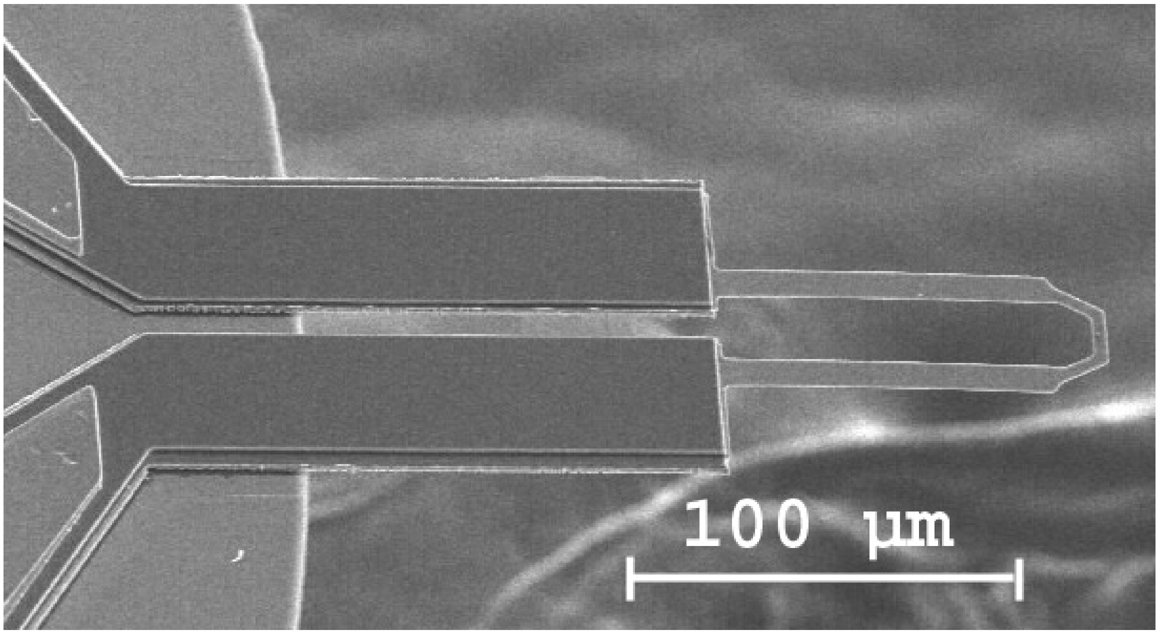

Figure 24. Image of heated atomic force microscopy cantilever fabricated at Georgia Tech. The cantilever features a resistive heating element in the end of the device and a read/write tip.

These cantilevers feature a low doped silicon region near the tip, effectively creating a resistive heating element as shown in operation in Figure 25.

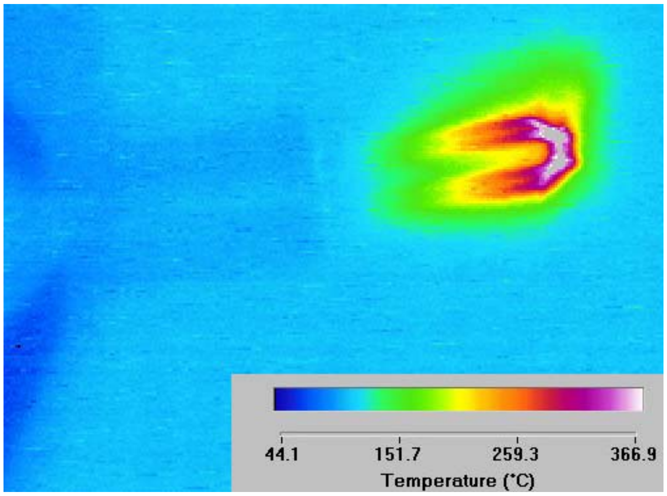

Figure 25. Infrared image demonstrating cantilever heating capability. The device shown is safely approaching 370 °C in the lesser resistively doped heater region. These cantilevers have demonstrated temperatures upwards of 800 °C without thermal damage.

Similar cantilevers were designed for data storage [90] and have since been shown to capable of highly sensitive metrology [91] and nanomanufacturing [92]. To deposit catalyst onto the cantilever, the device was taped onto a silicon substrate and inverted within a metal deposition chamber. Electron beam evaporation deposited 10 nm iron catalyst film onto the cantilever prior to its temperature calibration. The electron beam evaporated film was sufficiently thin to form islands upon heating [21, 93]; each island acted as an individual growth site for CNTs. The image in Figure 26 shows an iron film that has been broken up via heating in the cantilever heater region.

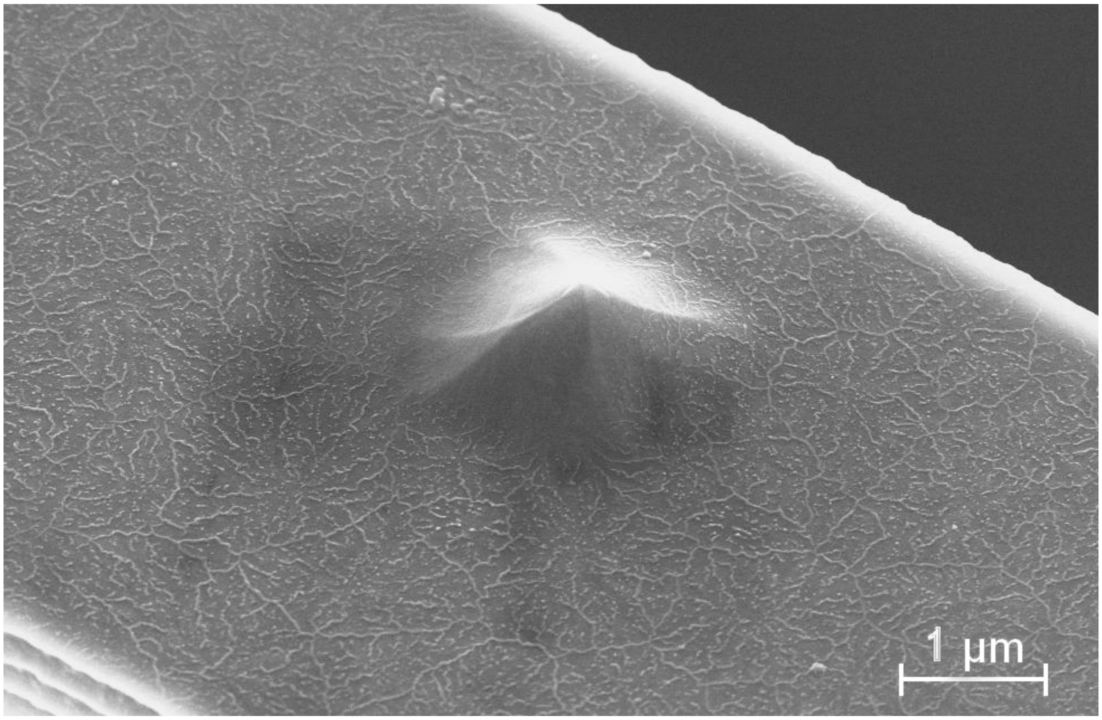

Figure 26. Scanning electron microscope image shows thin film iron catalyst breaking up under heating from the cantilever heater region. As the cantilever continues to heat, the iron film will continue to disperse and create CNT nucleation sites across the end of the cantilever. Also pictured at center is the sensing tip of the cantilever.

Resistance versus voltage curves were collected before and after the iron catalyst deposition and during the Raman spectroscopy based cantilever temperature measurements. Inspection of these curves ensured that the electrical functionality of the device remained constant. Figure 27 shows the typical response of a cantilever with increasing power input during each of the four phases of the cantilever synthesis process.

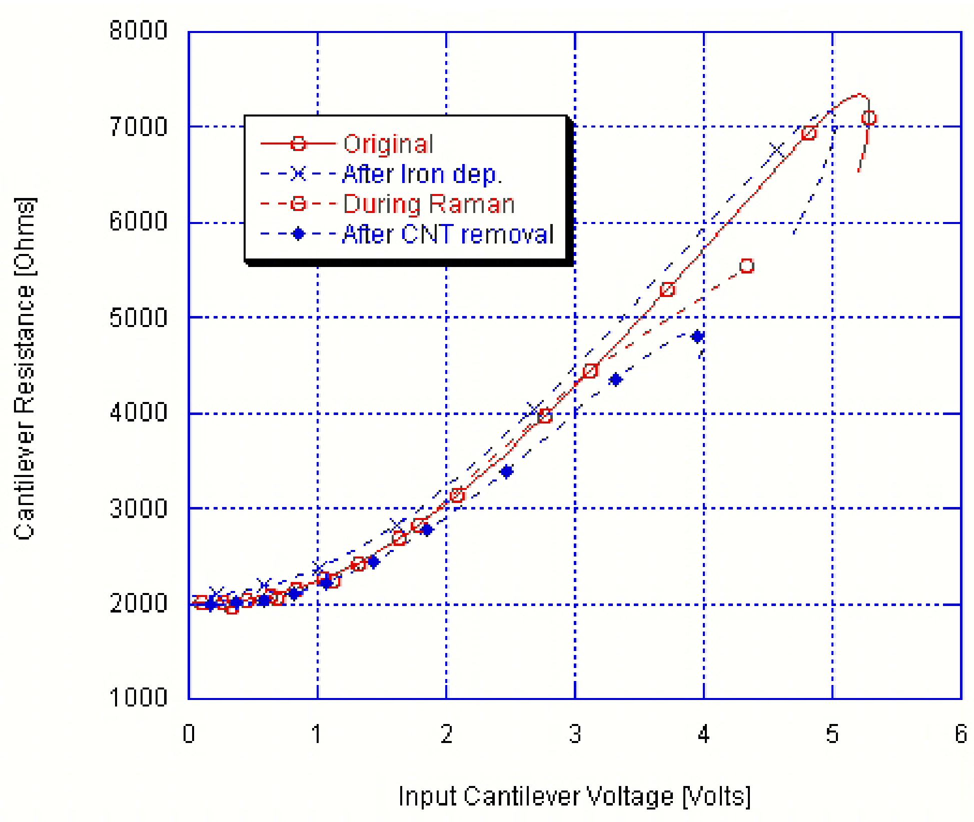

Figure 27. Cantilever resistance response to input voltage signal of 0-5 V. As seen in the figure, the iron deposition, temperature calibration and synthesis of the CNTs does not radically affect the electrical response of the device. The iron catalyst film is sufficiently thin such that it does not cause continuity across the cantilever electrical contact pads.

While infrared microscopy can be used to make an estimate of the cantilever temperature, a much more precise method is Raman spectroscopy. Laser Raman thermometry calibrated the temperature of the heated AFM cantilever to within 4 °C [94]. The cantilever temperature calibration was performed using a Raman Spectrometer operating in 180° backscattering geometry. The cantilever heater was excited by a 488 nm Ar+ laser and the scattered light was collected by a 0.25 m focal length spectrometer with a 3000 l / mm grating. The laser power at the sample was 57.3 µW and the collection time was 60 seconds. For these conditions, the laser did not produce heating in the cantilever. The Stokes shift, measured in wavenumbers, was linear with temperature between 300 – 1300 K, resulting in a simple device temperature calibration. The temperature of the cantilever tip, T_{tip}, was given by,

$$T_{tip} = \frac{\Delta\omega}{k} + T_{amb}$$

where $\Delta\omega$ is the change in the Stokes shift in wavenumbers between powered and unpowered states, k is the temperature calibration coefficient for silicon, and T_{amb} is the ambient room temperature. The temperature calibration coefficient, k, was equal to 0.023 $\mathrm{cm}^{-1}/°\mathrm{C}$ and determined by measuring the Stokes shift from a reference silicon sample placed in a heated temperature stage. The measured cantilever temperature was linear with input power of the device and thus a desired surface temperature could be achieved by controlling the input power. This calibration data is shown in Figure 28.

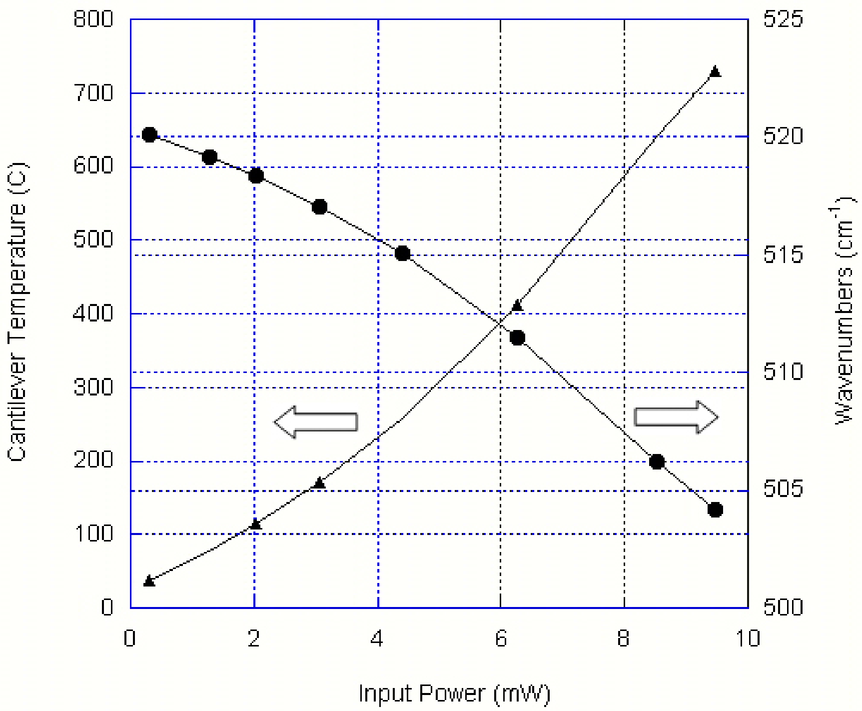

Figure 28. Raman temperature calibration of heated AFM cantilever. The Raman shift is linear with increase in cantilever input power during calibration. Because the Raman shift is also linearly related to the temperature of silicon, cantilever temperature can be estimated from input power to the device.

Raman measurements confirmed the presence of localized heating at the free end of the AFM cantilever in the small resistive, low doped region. The spatial temperature distribution along the end of the cantilever is demonstrated below in Figure 29. It can be clearly seen that the greatest temperatures are reached in the center of the cantilever heater region and then begin to lower with greater distance into the device legs. Additional details of the temperature profile have been published elsewhere [94].

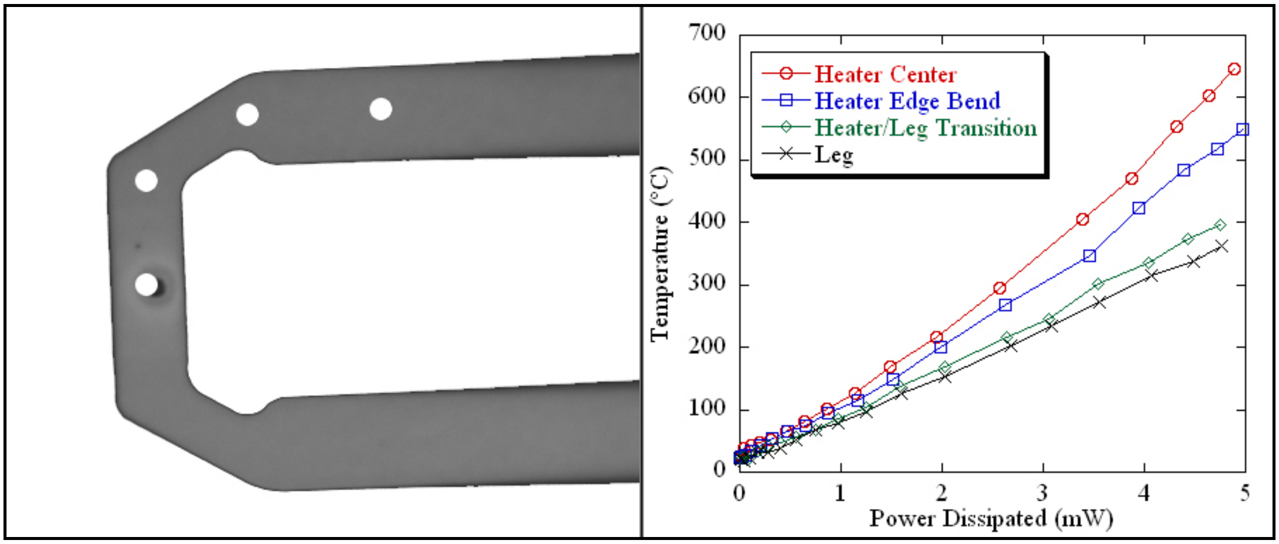

Figure 29. Cantilever image at left shows Raman spectroscopy scanning points. Plot of heating profiles is taken from work done previously on characterizing the heater region of thermal cantilever [28]. Plot indicates maximum temperatures at center of heater region.

Following the electrical and temperature calibrations, the cantilever was mounted into a 2" quartz tube, with electrical connections from the cantilever to external driving electronics. Abstract diagrams of the cantilever mounted inside the quartz tube are shown in Figure 30 and Figure 31.

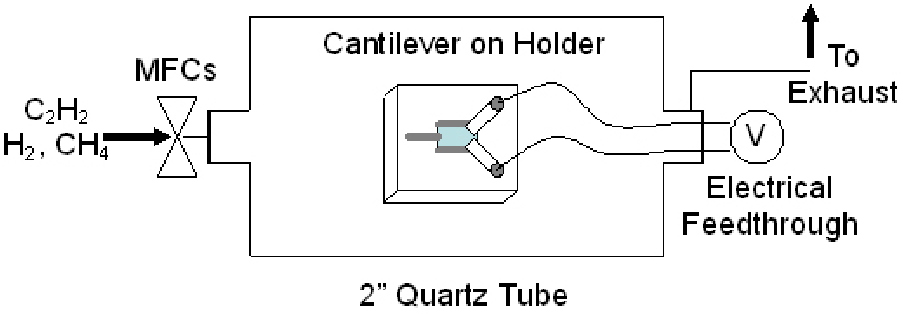

Figure 30. Cantilever mounting diagram for localized synthesis. Synthesis is performed inside quartz tube with no assistive ambient heating. Synthesis process takes approximately 10 minutes to complete and is readily assembled.

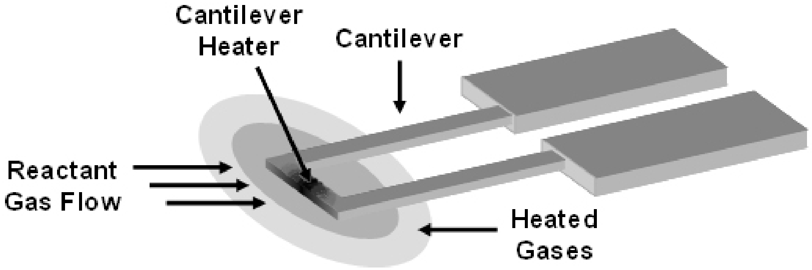

Figure 31. Enlarged detail of cantilever during CNT synthesis. During heating, carbon gases are decomposed and allowed to saturate the catalyst particles on the cantilever end.

Argon purged the tube for 2 minutes prior to the introduction of the hydrocarbon reaction gases and the cantilever heating. Following the purge, methane, hydrogen and acetylene were introduced and controlled by individual mass flow controllers at flowrates of 1000 sccm, 500 sccm and 100 sccm respectively for the duration of the growth period. During the trial, the cantilever was heated to 800 °C for 15 minutes. To achieve synthesis onto the cantilever heater region, the temperature of the gases surrounding the heater region must be great enough to induce decomposition of the carbonaceous gases. At the end of the soak period, the cantilever was powered down and argon was reintroduced to purge the remaining hydrocarbons. The entire process was performed at atmospheric pressure and without background furnace heating.

Microcantilevers are capable of highly sensitive detection of changes in mass adhering to the cantilever through changes in cantilever resonant frequency [95]. To quantify the added mass of the synthesized nanotubes, an Asylum MFP-3D AFM system measured the resonance properties at each stage in the processing. During these measurements, the cantilever was mounted into a rigid clamp. The AFM laser spot was reflected onto a photodiode capable of detecting the inherent thermal noise vibration in the cantilever. Using a fast Fourier transform, the software package was capable of locating the resonant frequency of the cantilever at four discrete steps of the synthesis process: prior and post iron deposition, post synthesis and finally post CNT removal from the cantilever.

3.2.2 Experimental Results

The following section discusses the results obtained by attempting direct CNT integration into a microsystem on an atomic force microscope cantitlever. Scanning electron microscopy (SEM) images taken of the cantilever after synthesis attempt, revealed vertically aligned CNTs covering the cantilever heater region. The CNTs were approximately 5-10 μm in height and of diameter in the range of 10-30 nm. Although the entire cantilever was coated in catalyst, the growth of CNTs was limited solely to the heater region as seen below in Figure 32, demonstrating the selectivity possible via this method.

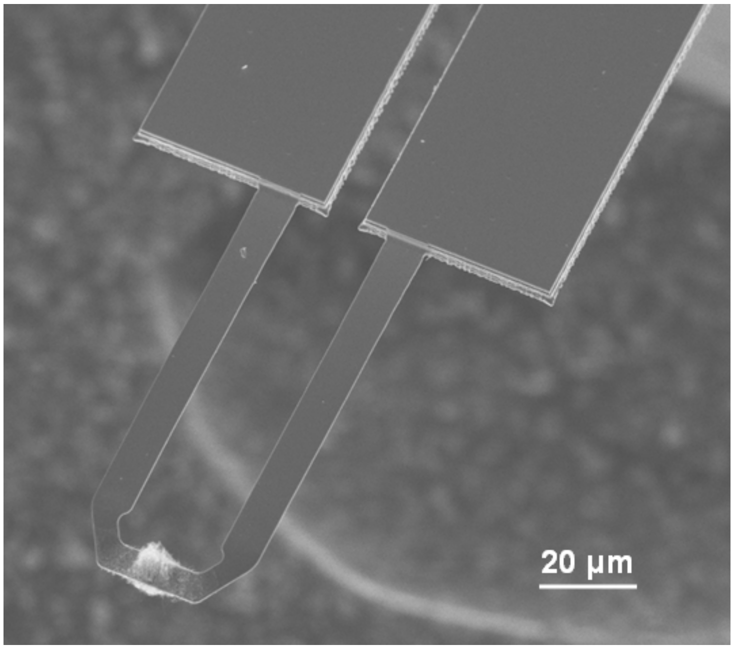

Figure 32. Scanning electron microscope image of the cantilever with CNTs on the heater region. As seen in the image, the CNTs are locally confined to the desired synthesis area.

Raman microscopy determined that the CNTs were highly graphitic with a graphitic to defect band intensity ratio greater than 2. The vertical array of nanotubes displayed a slight Gaussian profile across the length of the heater region as seen in Figure 33,

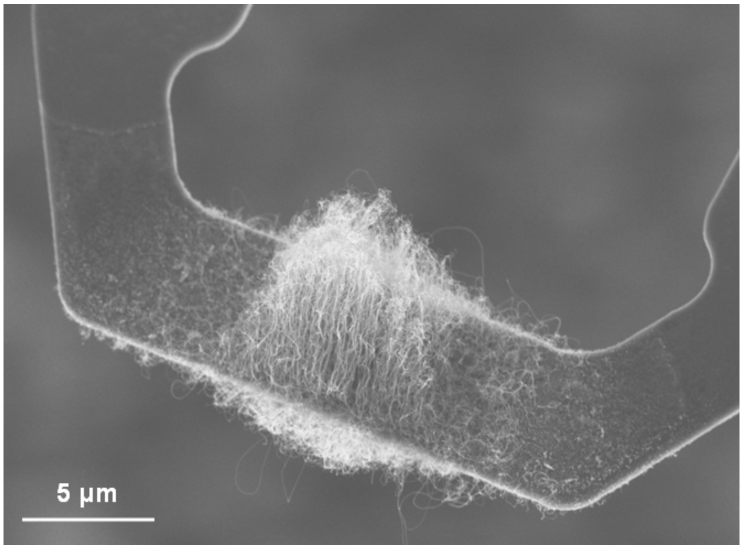

Figure 33. Enlarged view of cantilever heater region with CNT growth. The growth of CNTs is locally confined to the heater region and the tallest growth occurred at the midpoint of the heater region where temperatures are greatest. Breakup of the iron catalyst film can be seen extending outwards towards the legs of the device where temperatures gradually decrease.

providing insight to the temperature field in the cantilever and in the surrounding gas. Based on our experiments with heated ambient environments, an ambient temperature greater than 700 °C is required to create the aligned CNT arrays from 10 nm iron films.

As stated previously, microcantilevers are capable of highly sensitive detection of changes in mass adhering to the cantilever through changes in cantilever resonant frequency. The resonant frequency of the cantilever was measured at four times: initially, after depositing iron catalyst, with nanotubes on the end, and lastly after CNT removal. The cantilever resonant frequency decreased from 119.73 to 119.10 kHz, or about .52 %, due to the iron deposition, and then again 119.10 to 118.23 kHZ, or about .73 %, due to CNT growth. The cantilever was found capable of detecting mass changes as small as 5×10^{-16} kg. To ensure that we were indeed detecting CNT mass, the cantilever was self-heated to 900 °C in air, a process that reliably oxidizes and removes CNTs. SEM verified that the cantilever was cleaned in this cleaning step. Following cleaning, the cantilever resonant frequency increased to the pre-CNT value of 119.09 kHz. Figure 34 summarizes these resonant frequency results and is shown below.

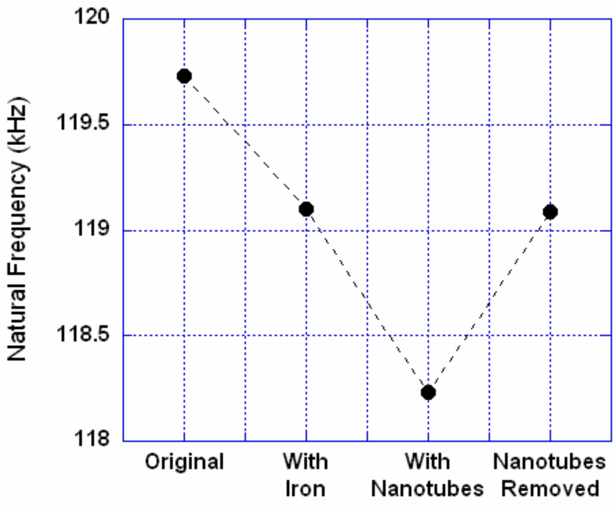

Figure 34. Resonant frequency of cantilever during process. With the added mass of the iron catalyst film, the frequency dropped to 119.10 kHz. After synthesis, the added point mass of CNTs resulted in a frequency decrease to 118.23 kHz. When the CNTs were removed through oxidation, the cantilever natural frequency increased to 119.09 kHz.

The change in mass due to CNT growth, Δm, can be modeled as

$$\Delta m = \frac{k\left(f_2^{-2} - f_1^{-2}\right)}{4\pi}$$

where k is the cantilever spring constant and f is the cantilever resonant frequency [95]. Typically this equation has a constant coefficient multiplier to account for the distribution of mass along the length of the cantilever, but in this case all of the CNTs are located at the cantilever free end and no multiplier is required. The cantilever spring constant was 0.536 N / m and thus we estimate that the mass of grown CNTs was close to 1.4×10^{-14} kg. This mass is consistent with estimates made from estimates of the nanotube volumetric coverage observed in SEM and assuming a density of graphite of 1.7 g / cm^3. The cantilever was further characterized with periodic heating with the goal of thermogravimetric measurement of the CNT mass, but we were unable to produce definitive results. The cantilever did not show a different response to an input electrical pulse with and without the CNTs, thus indicating the CNTs were a negligible addition of thermal mass. A plot of the heating time response can be seen in Figure 35, showing data before and after CNT mass removal.

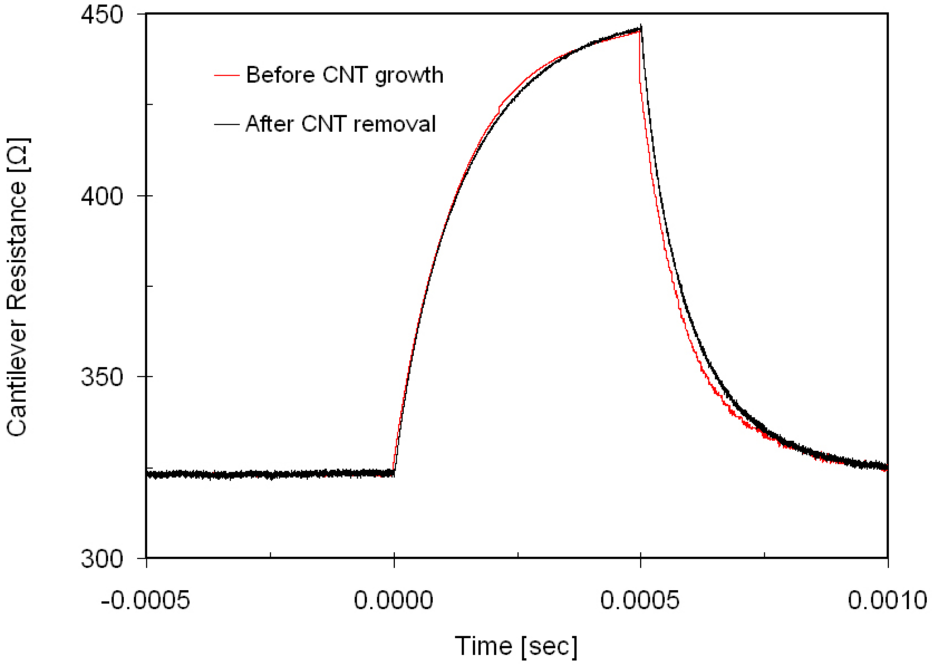

Figure 35. Heating time constant of cantilever. As seen, the added thermal mass of the CNTs did not alter the heating time constant of the cantilever heating region.

Finally, the cantilever was characterized with force-distance curves [96]. The nanotubes exhibited a spring constant of 10^2 less than the cantilever.

Factors Affecting Synthesis Success

There were several factors that affected the synthesis process that should be noted. The size of the heater region could affect the synthesis success rate, since it seems intuitive that a larger heater surface area would enable a greater decomposition of the carbon gas molecules. To test this phenomenon, microfabricated heater beams of lengths up to 500 µm were tested for their CNT synthesis capabilities. These beams, depicted in Figure 36,

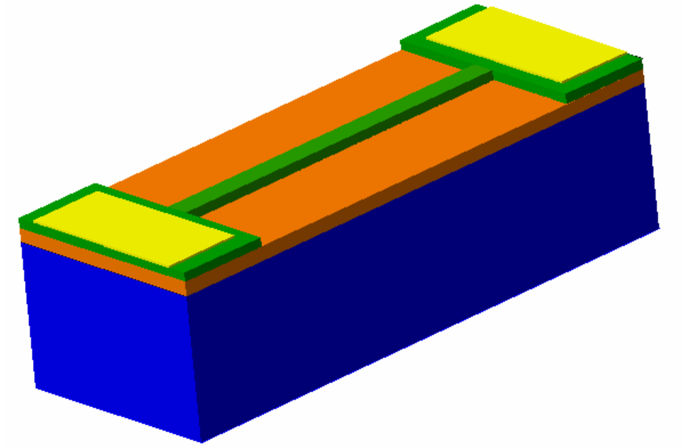

Figure 36. Schematic image of polysilicon heater beam. Beams were made from polysilicon on oxide wafers using a two step lithography process in lengths of 100, 200, 300, 400, 500 µm and widths of 5, 10, 20 µm. The aluminum contact pads seen in yellow were $1 cm^2$ for electrical connectivity.

were created using a two step lithography mask process from a doped polysilicon-on-oxide wafer and are described in detail elsewhere [28]. A fixed polysilicon beam as pictured in Figure 37,

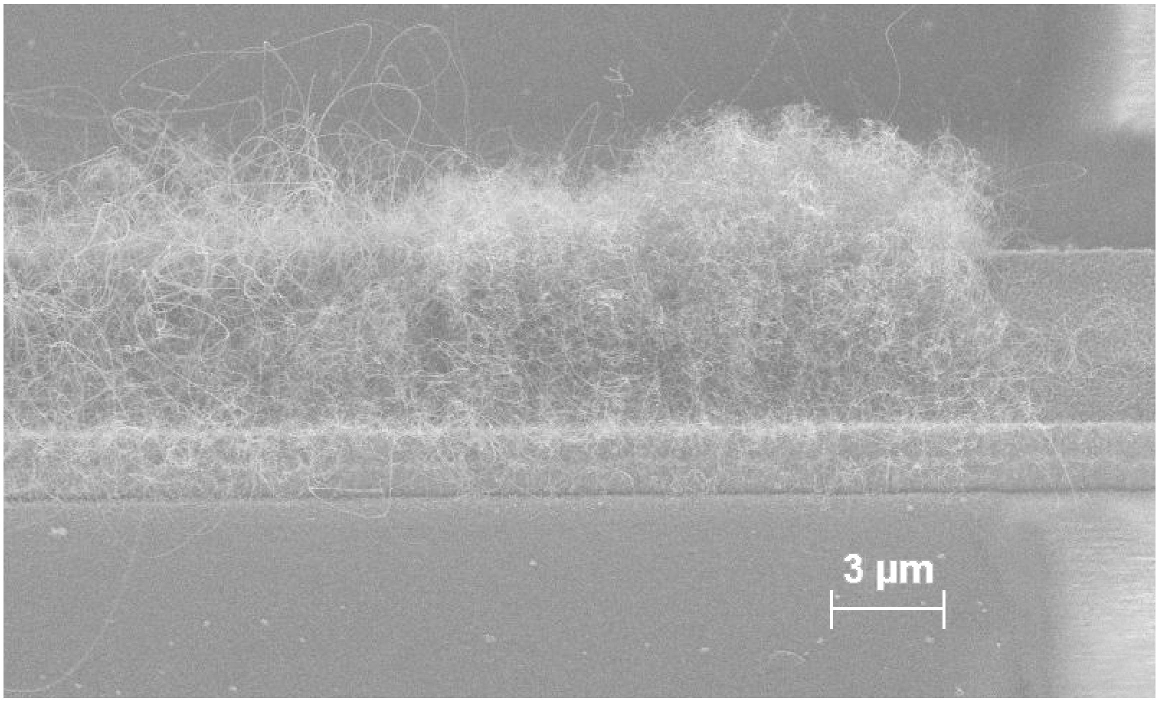

Figure 37. Growth of CNTs on polysilicon heater beam. The synthesis of CNTs onto heated beams proved easier than onto the cantilever structure due to their large size and ability to withstand large amounts of input power.

proved much more reliable in yielding CNT growth. Another factor was the ambient conditions present while making the temperature calibrations. Measurements made in laboratory air are quite different than inside the synthesis chamber at the time of synthesis. The thermal conductivity of the process gases at the time of synthesis, are higher than that of air, therefore resulting in a varied heat flux conducted to the surrounding gasses. The carbonaceous gases flowing during the synthesis trial are also acting in convection, dissipating some of the heat generated in the tip. The total volumetric flow rate of approximately 1.5 liters per minute divided by the cross section of the 5cm tube gives a gas velocity of roughly 50 cm per minute.

3.3 CNT Enhancement via Protective Coatings

To test the ability of enhancing the robustness of CNTs, vertically aligned CNTs, with an average diameter of approximately 20 nm, were produced on silicon substrates and coated with aluminum dioxide and titanium dioxide via atomic layer deposition (ALD).

3.3.1 Experimental Setup & Methods

The CNTs were placed within a chamber and exposed to chemical precursors following an experiment based on ALD processing conditions described elsewhere[97]. The sample was placed into a custom built ALD chamber as seen schematically in Figure 38.

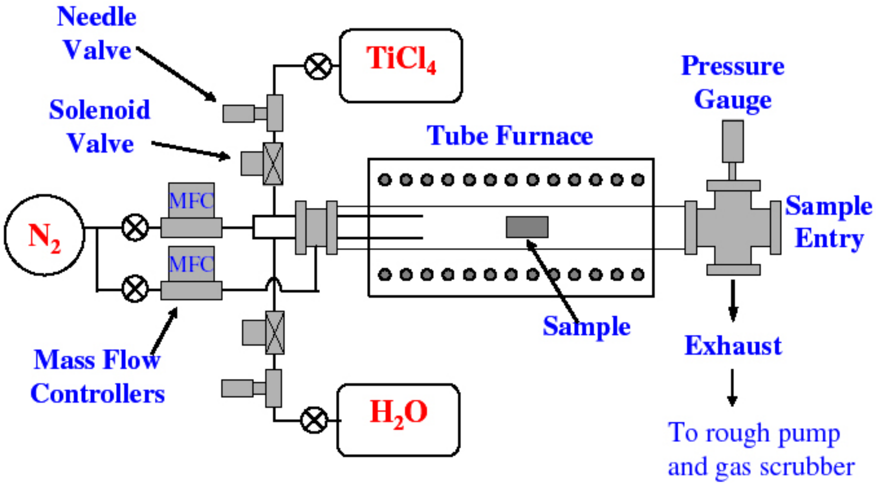

Figure 38. Experimental setup of an atomic layer deposition chamber (ALD). Similar to the chemical vapor deposition setup, ALD involves both mass flow controllers and a heated box furnace. In this setup however, solenoid valves provide the ability to pulse process gases.

This chamber consists of a rotary vane pump, a Thermolyne tube furnace with a single zone that houses the sample deposition area, a chemical precursor delivery system, and a nitrogen purge. The tube furnace is specified to have a 6” wide region with a ±0.3°

C temperature variance, and a 12” region with ±3° C temperature profile. The substrates were placed on a 4” quartz boat and were positioned 5” from the center of the furnace, toward the exhaust side. The temperature deviation in this 4” region was measured to be ±0.15 °C at 100 °C. The system was designed for liquid precursors and is capable of producing both titanium dioxide, TiO_2, and aluminum dioxide, Al_2O_3. The production of TiO_2 utilized $TiCl_4$, Titanium Tetrachloride and H_2O liquid precursors, while the Al_2O_3 used $Al(CH_3)_3$, Trimethylaluminum and H_2O liquid precursors.

TiO_2 was grown onto the CNTs using alternating 4 sec pulses of $TiCl_4$ and H_2O, each separated by a 10 s, 225 sccm N_2 purge, while maintaining the substrate at 100 °C. Meanwhile the Al_2O_3 was grown onto the CNTs using alternating 4 sec pulses of $Al(CH_3)_3$ and H_2O, each separated by a 10 s, 225 sccm N_2 purge, while maintaining the substrate at 80 °C. Using known deposition rates, the ALD process was allowed to deposit sequential layers until layers of approximately 10 nm were deposited onto the CNTs. The vacuum level within the reactor was ~500 mTorr during pulses, and 200 mTorr during purges. The precursor gases, derived from room temperature liquid sources, were introduced to a N_2 carrier gas using computer controlled solenoid valves. Post-deposition heat treatment was performed in the ALD reactor with constant N_2 flow of 225 sccm.

To test the robustness of these enhanced CNTs, the coated samples were placed inside a Linkam brand, model 1500 heating chamber and exposed to heated laboratory air. The heating chamber is shown in Figure 39.

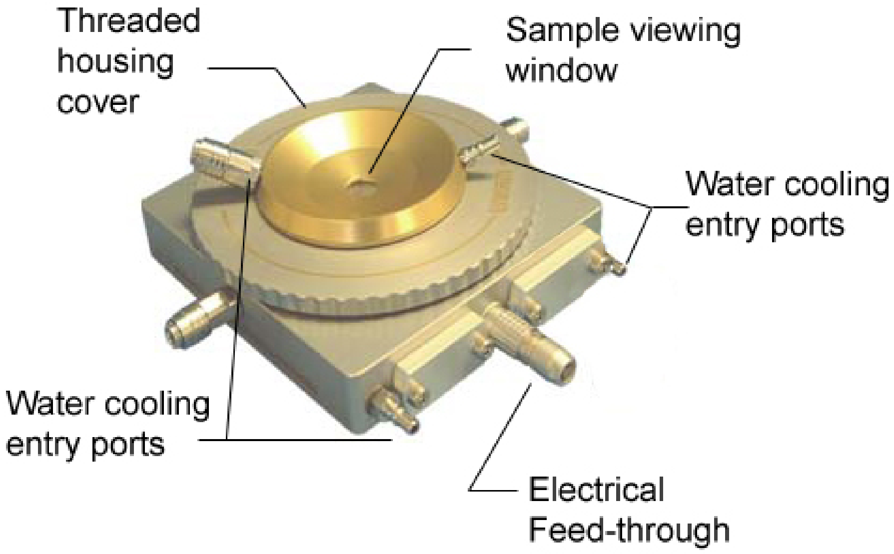

Figure 39. Linkam TS-1500 spectroscopy compatible heating stage. The top viewport window allows for Raman microscopy scanning at elevated temperatures up to 1500 °C. The chamber also has the capacity for vacuum, electrical feed-through, and gas connections. The stage temperature is controlled using heating pulses from a separate temperature controller. The stage is used to characterize samples under elevated temperatures.

The temperature inside the crucible was raised to 700 °C, a temperature which readily oxidizes CNTs, and maintained for a 30 minutes. During the heating period, the sample was monitored via Raman spectroscopy using a 50X ultra long working distance objective. The graphitic peak was monitored and a scan of the sample was completed every 4 minutes. This experiment was performed on samples receiving 10 nm layers of Al_2O_3 and TiO_2 and also on a bare control sample.

3.3.2 Experimental Results

CNTs having received protective coatings were subjected to thermal oxidation and the life span of the sample was noted. With increased duration, the sample was slowly oxidized, resulting in a decrease in the graphitization of the CNTs, detectable by the loss of spectral counts in the 1580 cm^{-1} wavenumber regime. By this experiment, a subjective conclusion could be made if certain CNTs were made more robust or protected by their coatings.

A more common experiment to test the robustness of materials to thermal oxidation is thermogravinometric analysis or TGA. TGA works similarly to the method employed here, but instead monitors sample mass fluctuation as a function of time. Although available, this method was not attempted due to the lack of precise knowledge of sample coating thickness and the total CNT mass and the lack of a sufficient sample size (~5 mg). Figure 40, shows the normalized intensity of the characteristic graphitic CNT peak with respect to time for the Al_2O_3 and TiO_2 samples as well as an uncoated controls sample.

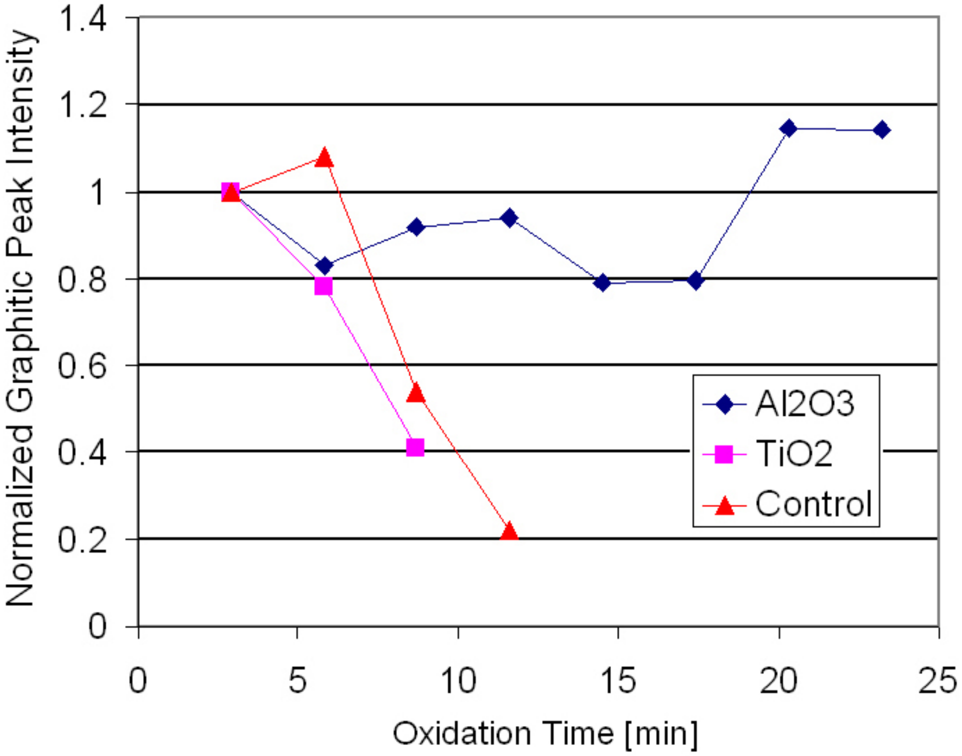

Figure 40. Degree of graphitization given by the ratio of the Raman measured G band (1580-1620 cm^{-1}) intensity over the initial graphitic band intensity. While the control sample and TiO_2 coated CNTs show rapid loss in graphitization, the Al_2O_3 coated CNTs prove to be more resistant to oxidation at 700 °C.

As seen in Figure 40, the sample that resisted oxidation the best was coated in alumina. The TiO_2 and unprotected control samples both oxidized very rapidly in almost the same amount of time. The poor performance of the titanium dioxide sample likely stems from the lack of an ALD coating as evidenced by small diameters in SEM images. Some gas species adhere better to a given surface than others and successful ALD growth is largely dependent upon the synthesis parameters. As seen in Figure 41(c,d), the outer diameter of the TiO_2 CNTs pictured does not seem to have been enlarged by the desired 10 nm coating. Measurements made with a SEM provided sample diameters of 24.9, 25.8, 23.8 and 26.6 nm for ALD TiO_2 coated tubes expecting 10 nm conformal coatings. For the sample to have received the desired TiO_2 coating, the CNT original diameter would need to be roughly 5 nm, small for MWNTs made via our processing conditions.

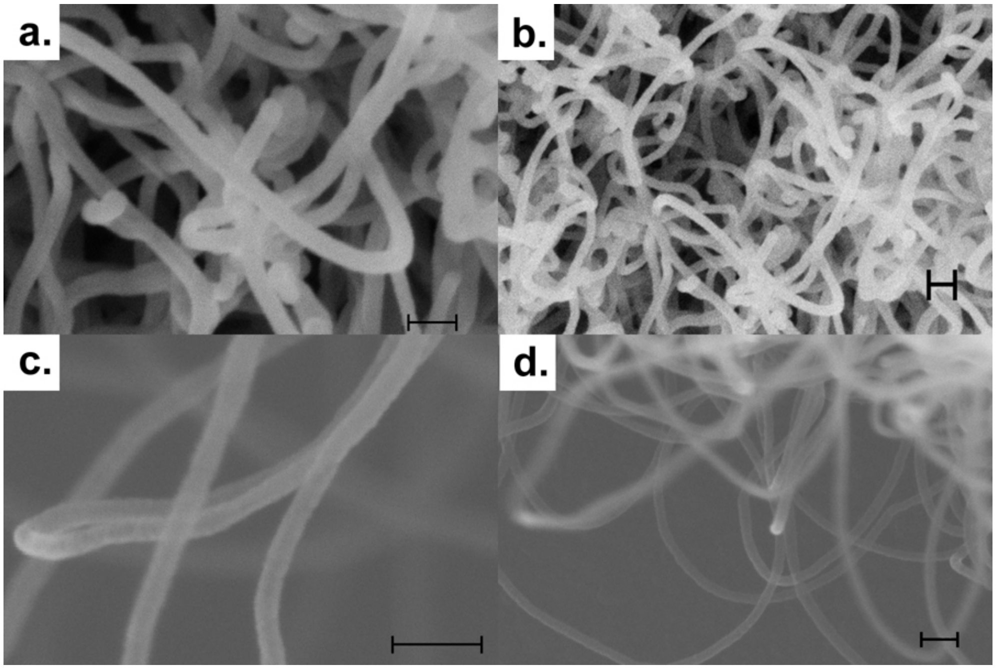

Figure 41. ALD coated CNTs, 10 nm Al_2O_3 (a,b), 10 nm TiO_2 (c,d), all scale bars are equal to 100 nm. The Al_2O_3 coated tubes (a,b) exhibit diameters between 40-50 nm, thus supporting the 10 nm conformal coating onto ~20-25 nm CNTs. The CNTs coated with 10 nm TiO_2(c,d) however, appear similar to the original 20-25 nm features.

While the titanium coatings proved ineffective at protecting the CNTs from oxidation, the alumina coatings did make the CNTs more resilient. As seen in Figure 41(a,b) the alumina coated CNTs appear larger and fused together in places where the CNTs were in close proximity during the coating process. Measurements taken of the alumina coated CNTs reports outer diameters of 45.3, 48.4 and 50.2 nm. These measurements are consistent with expected data, given that CNTs made by our thermal CVD process are typically 20-25 nm in diameter. As seen in the oxidation graph above, the aluminum dioxide sample was very resilient to oxidation at a temperature of 700 °C. With increased duration, beyond what is shown in the graph, the probing laser began to induce further heating of the tubes leading to a more premature oxidation in the measurement area.

To ultimately detect whether a TiO_2 or Al_2O_3 coating is present, transmission electron microscopy (TEM) or energy dispersive spectroscopy (EDS) analysis could be performed upon the sample. Unfortunately, TEM and EDS analysis were not performed to help distinguish whether an ALD coating was present.

CHAPTER IV: NANOTUBE INTEGRATION/PRINTING

Combining inherently flexible nanomaterials with polymer substrates could yield low-cost high-performance electrical devices which cannot be produced using current semiconductor processing methods. As most polymers can not withstand high synthesis temperatures, there exists a need for methods to integrate CNTs into substrates at low temperatures. To create flexible electronic traces and other enhanced substrates, CNTs were imprinted into polymer in two distinct fashions. The CNTs were printed in a two dimensional manner with random orientation via hot emboss imprint lithography and also in a three dimensional manner with vertical orientation via microwave embossing. These low temperature interfacing methods are vital to applications where elevated temperatures can cause damage to components.

4.1 Hot Emboss Imprint Lithography

4.1.1 Experimental Setup & Methods

This section outlines the experimental setup required to realize the integration of CNTs into 2-dimensional flexible electronics and is described in detail elsewhere [98]. To create two dimensional networks of randomly aligned CNTs, hot embossing imprint lithography was employed. Aligned CNTs were grown on silicon master templates, and then transferred into polymethyl methacrylate (PMMA) near the PMMA glass transition temperature, T_g, using a dual heated platen hydraulic press. Patterning of the catalyst and the resulting nanotubes was independent of surface texture. Smooth master templates transferred the CNTs to the polymer without significantly affecting polymer topography.

The complete imprint process is shown below in Figure 42(a-c), demonstrating the initial sample placement, pressing motion, and subsequent platen release.

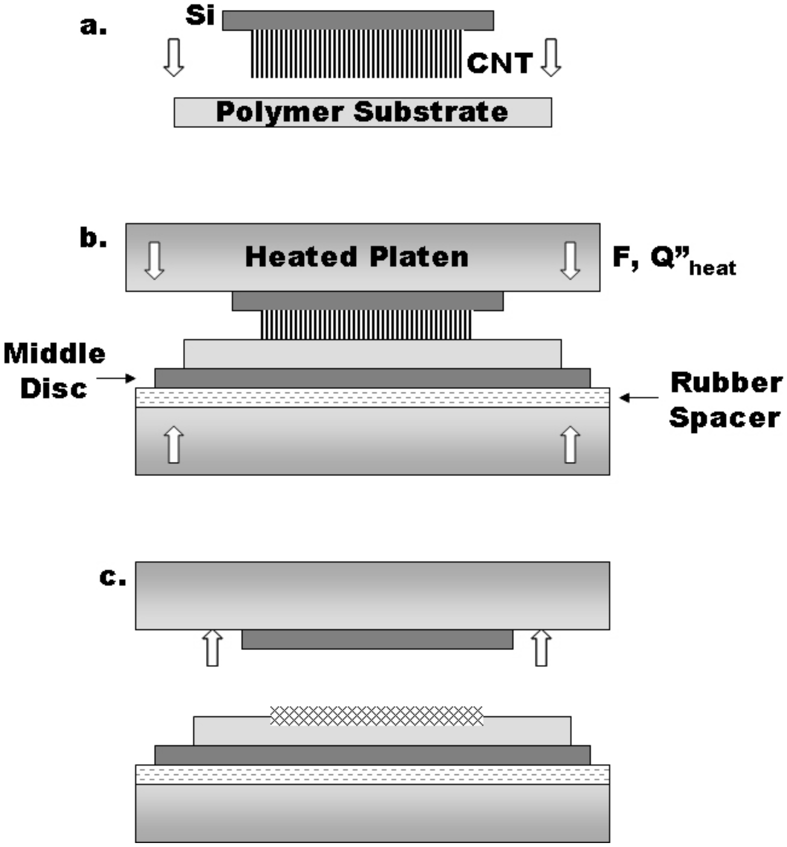

Figure 42. Imprint lithography printing process. The CNT patterned silicon coupon is placed face down onto the polymer substrate (a). This sandwich is placed inside the heated press on top of a clean middle disk resting on a rubber spacer. The rubber helps achieve a uniform loading across the sample. After pressure is applied for 4 minutes the platens are separated revealing the sample.

Master templates were fabricated from standard silicon wafers having a SiO_2 surface layer. Evaporated iron catalyst films (10 nm thickness) were patterned on the SiO_2 using photolithography and a standard lift-off technique. The iron catalyst was patterned in parallel lines 8 mm X 10 μm with line pitch varying 10-500 μm.

To synthesize CNTs, the wafer was diced and placed into a high temperature CVD furnace. The templates were preheated to the temperature of 660-900 °C in Argon, and then exposed to a mixture of acetylene, hydrogen, and methane in a 1:5:10 ratio for growth periods of 3-15 minutes. After synthesis, the templates were placed in a hot press upside down on a PMMA substrate and heated to 143 °C under a 667 N force as seen in Figure 42(b) and maintained for 4 minutes. To help prevent translation and smearing of the CNT features, a metal disk was not placed onto the sandwich structure as seen above in Figure 42. After cooling to room temperature, the load was released and the master removed from the substrate as seen above in Figure 42(c). The success of this process was inspected using a high resolution scanning electron microscope (HRSEM) after a thin gold film was deposited onto the sample.

Electrical characterization of the imprinted CNT traces was performed using a standard field effect transistor structure. First, wires were attached to the ends of the nanotube traces to form the source and drain contacts. Parylene (1 μm) was evaporated over the devices to serve as a gate dielectric for an evaporated Au gate electrode. Gate lengths were 6-8 mm. Current-voltage characteristics were measured using a source meter. The tests showed linear I-V responses for source-drain voltages up to 30 V. Gate biases to 250 V showed no effect on the I-V response; subsequent tests were performed on devices without a top gate contact due to the lack of a transistor like response. Resistance values ranged between 1 kΩ – 9 MΩ across all samples. For a single die, resistance variations of ±20% across 10 CNT traces could be obtained. A slight increase in sample resistance was also observed with bending strain. In addition, impedance measurements between 1 -30 MHz revealed no frequency dependence, showing some attributes of simple metallic resistors.

4.1.2 Experimental Results

Carbon nanotube synthesis on the silicon master templates produced well-controlled dense patterns with vertical alignment as shown in Figure 1. Scanning electron microscopy (SEM) images showed that the nanotubes were of height 5 – 100 nm, depending upon process conditions. Raman spectra showed the nanotubes were highly graphitic and transmission electron microscopy showed the CNTs were predominately multiwalled.

Inspection of the CNT transfer into the polymer showed very good transfer as can be seen in Figure 43 below.

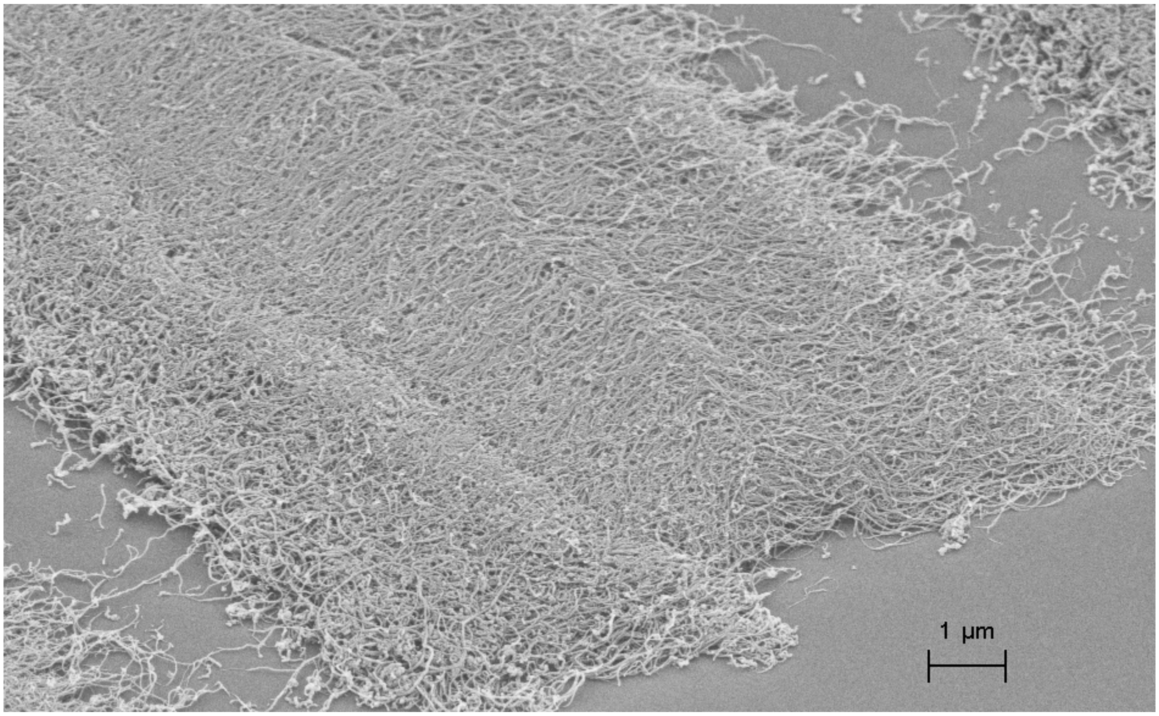

Figure 43. Scanning electron microscopy image of two dimensional CNT imprint by hot emboss imprint lithography process. As seen in the image, the CNTs are well adhered to the substrate. The CNTs have a very low vertical profile and show very low traces of catalytic iron particles at higher magnification images.

Inspection of the master template revealed that the majority of the carbon nanotubes were transferred into the polymer substrate. The CNTs remaining on the master were sparse and were only visible under SEM. The transfer of the nanotubes into the polymer can be attributed to two mechanisms: 1) the adhesion of the nanotubes to the deforming polymer when embossed near Tg, and 2) entanglement in the nanotube network which occurs during aligned growth. The entanglement of CNTs can result in large areas of nanotubes being transferred from interlocking forces. Such an effect is key to manipulating continuous nanotube films pulled from CNT forests. As expected Raman spectra showed no structural change in CNTs following transfer, since no major deformation of the individual CNTs took place.

Electrical testing of the imprinted CNT traces without gate electrodes produced typical I-V responses to the one as seen below in Figure 44.

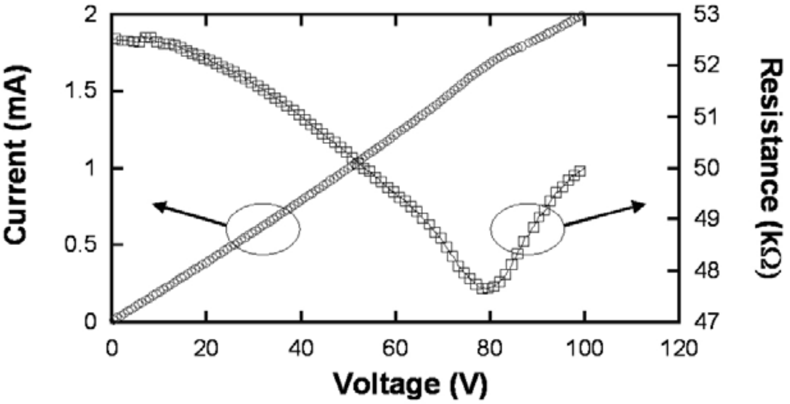

Figure 44. Typical I-V response of imprinted CNT trace. The linear behavior of the CNT trace is similar to the response of a resistor, indicating that most of the CNTs are metallic. The resistance of the trace decreases with resistive heating up to 80 V, where the trace begins to experience failure due to melting of the surrounding polymer.

For this sample, the room temperature resistance was 52.5 kΩ but decreased with increasing applied power due to resistive-heating above 10 V which was also confirmed using infrared thermography. The CNT network exhibited a linear but negative temperature coefficient of resistance (TCR) near -51.3 Ω / °C, typical of semiconductors. This behavior is indicative of the thermally-induced excitation of charge carriers in the nanotube network. In general, the TCRs were 0.04 – 0.1 % / °C for all samples. For voltages above 80V, a permanent residual increase in resistance was observed which was associated with the melting of the PMMA and significant deformation of the CNT traces. Further exploration of the effect of deformation on the nanotube network through bending experiments was also performed. Bending of the samples out to 2.5% strain resulted in an increase of approximately 3% in resistance as seen in Figure 45.

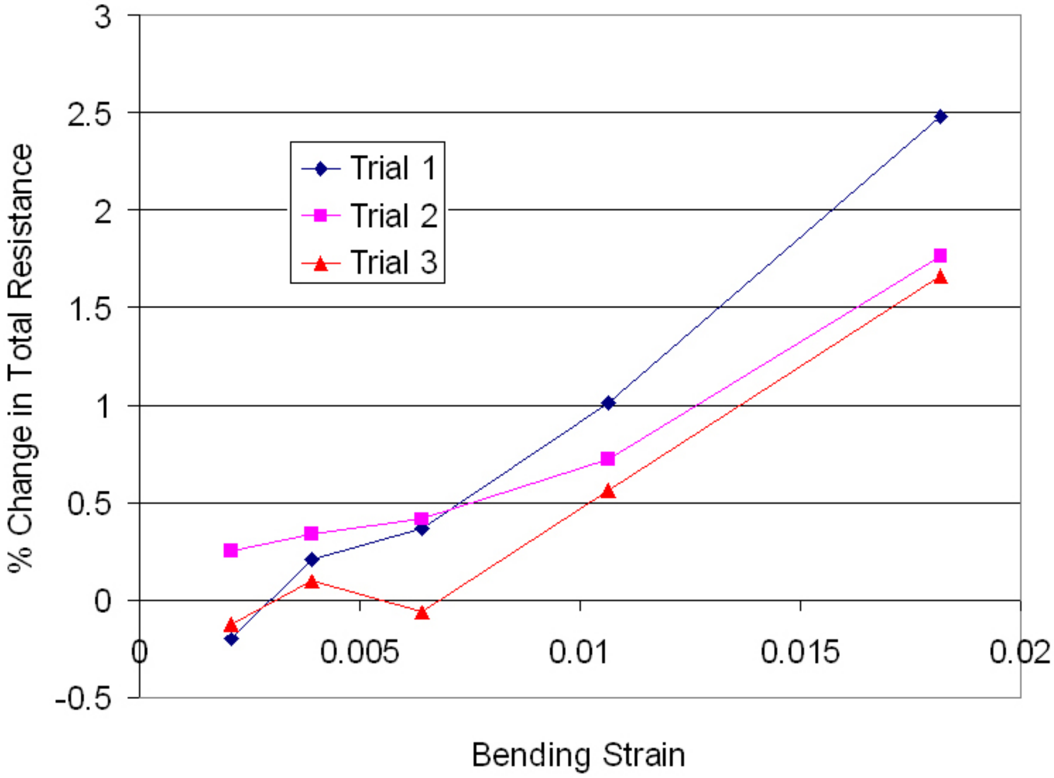

Figure 45. Imprinted CNT trace response to bending strain. Varying amounts of bending strain were applied to the trace and the resistance was found to vary 1% between 3 successive trials. This demonstrates the ability of the CNT-CNT network within the trace to accept deformation and reforming without a loss of electrical conductivity.

After releasing the load, a residual increase in trace resistance of about 1% was observed due to the deformation showing very minor effects on sample behavior for small strain applications.

4.2 Vertical Variable Frequency Microwave Imprinting

As opposed to imprinting CNTs in a two dimensional manner, the following sections describes the newly discovered process of transferring vertically aligned CNT features into a polymer surface using a variable frequency microwave (VFM) as the source of heating excitation.

4.2.1 Experimental Setup & Methods

Figure 46, as seen below, shows the process in which carbon nanotubes were transferred into a commercially available polycarbonate film. As seen in Figure 46(b), microwaves instantly heat the samples uniformly in comparison to hot embossing method.

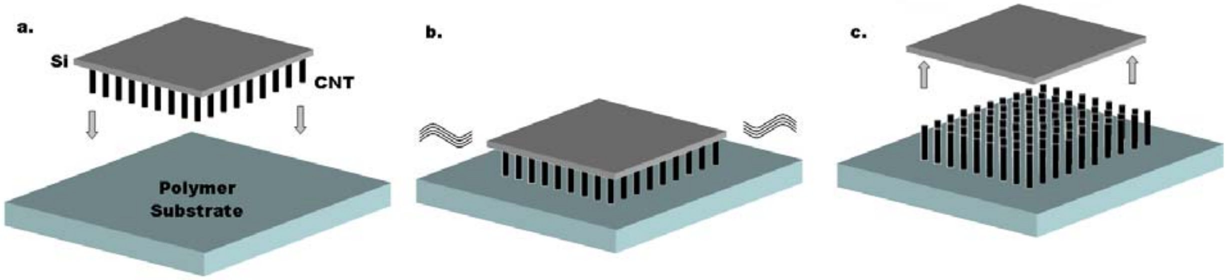

Figure 46. Schematic shows process of transferring CNTs into a polymer substrate by variable frequency microwave excitation (a-c). The CNT patterned coupon is placed face down onto the polymer substrate (a). The sandwich is then placed inside microwave chamber and exposed to electromagnetic waves for 4 minutes (b). The silicon coupon is then lifted from the embedded CNTs, leaving vertically standing features (c).

Vertically aligned carbon nanotube arrays were first grown on a silicon substrate by chemical vapor deposition. First, a 200 nm thermal oxide layer was grown on 525 μm thick silicon substrate as a catalyst support. To promote the self assembly of carbon nanotube arrays, a 5 nm iron thin film was patterned on the oxidized surface using standard photolithography and lift off techniques. Patterns consisted of arrays of circles that were 10 μm in diameter and squares which were 750 μm on a side. The sample was then placed in a quartz tube furnace and heated to 740°C for 10 minutes under 1000 sccm of argon flow to promote the break up of the Fe catalyst into nanoparticle nucleation sites. Carbon nanotubes were grown using a mixture of methane, acetylene and hydrogen at flowrates of 1000, 100, and 500 sccm, respectively for 15 minutes. Inspection of the carbon nanotubes showed excellent vertical alignment with an average diameter of 20 nm and a height of 50 μm. Microraman spectroscopy measurements indicated a graphitic to defect intensity ratio greater than 1.5. No radial breathing mode was observed, indicating that the tubes were multiwalled. By varying the synthesis time, gas flow rates and substituting ethylene for acetylene, the vertically aligned carbon nanotube height could be easily varied from 2- 200 μm. These tubes were synthesized under the same conditions as the hot embossing CNTs.

The silicon master with the aligned CNT patterns was then placed on a 500 μm thick polycarbonate film with the nanotubes facing the polymer. Care was taken to ensure that very little translation or shifting of the silicon substrate occurred in order to prevent shearing of the nanotube patterns. Avoiding the shearing of the nanotube patterns was important for printing vertically aligned tubes since the weak SiO_2-supported Fe catalyst interface promoted easy removal of the tubes with applied force.

Thus, distortions from shearing would result in tubes being removed from the stamp prior to printing. It would be possible to use a multilayer catalyst structure including films such as Ti and Al to promote greater adhesion, if desired, which would allow shearing to be used to print patterns at an angle. In the current approach as depicted in Figure 46, the polycarbonate/nanotube/silicon structure resulted in the weight of the silicon substrate being supported by the nanotube arrays which provided the pressure during the embossing process.

The sandwiched structure of silicon, CNTs and polycarbonate was then placed inside a Lambda Technology model Microcure 2100 variable frequency microwave (VFM) to locally heat the carbon nanotube pattern. The microwaves were emitted by a CPI brand rack mounted generator. In this process, the conductive silicon and carbon nanotube features coupled with the microwave energy which caused them to heat while the polycarbonate remained at room temperature. As a result of the low thermal conductivity of the polycarbonate film, highly localized heating was expected to occur at the nanotube-polymer interface. The microwave processing was operated under temperature control where the microwave source was pulsed in order to heat the sample to a desired temperature. In this arrangement, a fiber optic-coupled infrared sensor monitored the backside of the silicon chip; monitoring the temperature of the nanotubes directly was not possible. For temperature measurements, an emissivity of 0.75 was used for the rough silicon surface which correlated well with calibrations on a Quantum Focus Infrascope IR microscope system.

To determine if monitoring the backside of the silicon substrate was sufficient for estimating the nanotube temperature, separate microwave heating experiments for a polycarbonate, silicon, and carbon nanotube sample were performed. First, an IR sensor was focused on a polycarbonate film which was exposed to 60W of microwave energy for 2 minutes. Virtually no heating of the polycarbonate was observed, as seen below in Figure 47.

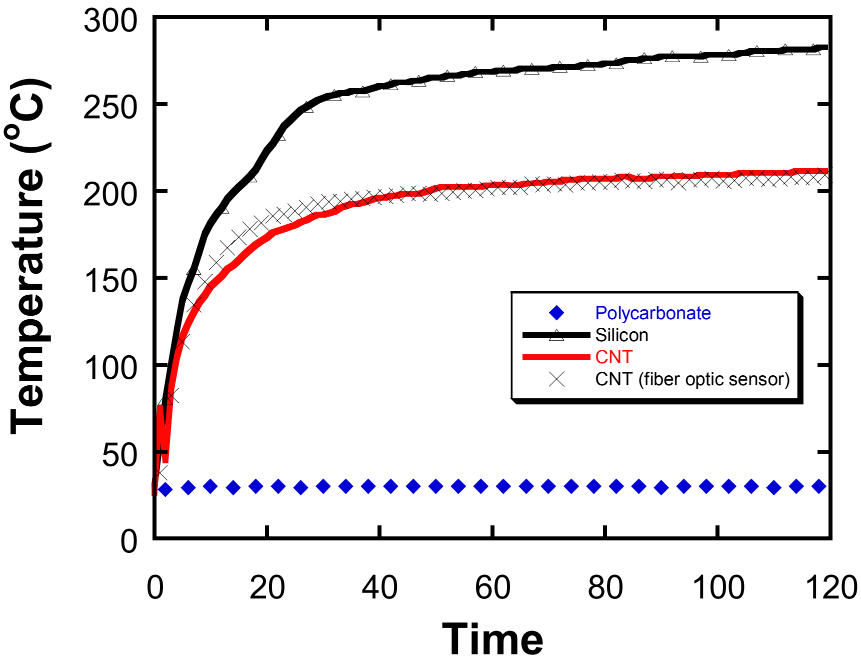

Figure 47. Individual temperature profiles for CNTs, silicon, and polycarbonate substrate during microwave exposure process. Each sample was exposed under the same power setting for 2 minutes and monitored via an infrared temperature sensor. The silicon demonstrated the greatest ability to absorb microwaves, while the polycarbonate did not show any signs of heating. This indicates that heat generated in the silicon and CNTs is conducted through the CNTs to melt the polycarbonate substrate locally.

Next, a blanket film of carbon nanotubes followed by a bare silicon sample were also exposed for two minutes and monitored by the IR sensor. Figure 47 shows that both the carbon nanotubes and silicon sample were subject to heating, with the silicon obtaining a higher temperature in both cases. The silicon achieved the greatest temperature because it is considered the most “lossy” material in the stacked structure.

An additional fiber optic based IR sensor was also used during the silicon heating experiments which agreed well with the remote IR sensor (Figure 47). These data suggest that during the processing of the structure in Figure 1, the silicon substrate obtains the highest temperature of any layer during microwave exposure. Since the carbon nanotubes also have a high thermal conductivity and low thermal mass, the nanotubes are expected to exhibit very little temperature drop between the surface of the silicon and the tip of the nanotubes. The backside silicon temperature is thus expected to be a good estimate of the carbon nanotube tip temperature.

Using the variable frequency microwave excitation, the backside temperature of the silicon was raised to 145 °C at a rate of 2 °C/second and held for 4 minutes to allow for pattern transfer. The emitted center frequency was 6.425 GHz and varied over a bandwidth of 1.15 GHz every 0.1 seconds. After microwave exposure, the sample was allowed to cool back to room temperature before being removed from the enclosure. The top side silicon was then removed from the assembly by tweezers. The entire sample then made conductive upon receiving a thin sputtered gold film prior to being inspected using high resolution SEM.

4.2.2 Experimental Results

The results of vertically imprinting CNTs via microwave excitation show this method to be a new and promising procedure for nanostructure transfer. Figure 48, as seen below, shows the transfer of cylindrical carbon nanotube towers and square patterns.

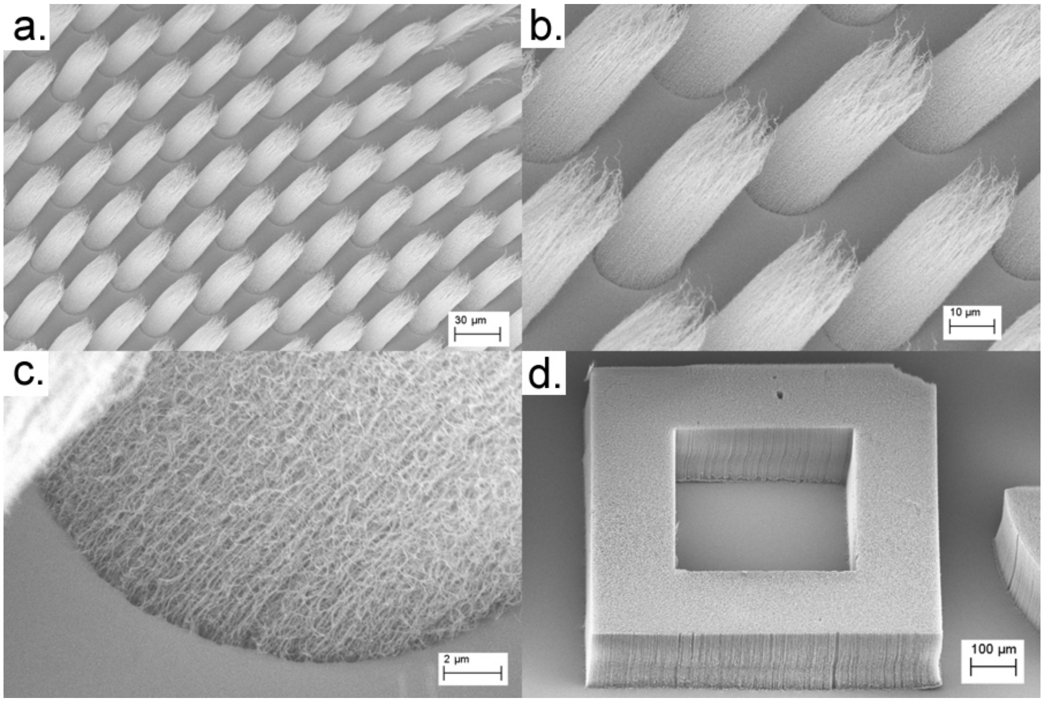

Figure 48. Microwave embossing of vertical aligned CNTs. Differences in adhesion between the silicon substrate and the CNTs accounts for the torn CNT appearance (a,b) versus the smooth surface appearance (d). The CNTs are submerged into the melted substrate as seen in image (c).

From the scanning electron microscopy images, it is clear that excellent vertical alignment of the features is maintained from this process. A close up image of the device shows that the tubes are embedded in the polymer layer with little distortion of the polymer around the nanotube towers as a result of the localized heating of the polymer around the nanotubes. In the case of the nanotube towers, the carbon nanotubes appeared “torn” at the top surface. An inspection of the silicon stamp after the microwave transfer process revealed a number of carbon nanotubes still adhered to the silicon surface. Subsequent trials resulted in a very clean transfer from the silicon stamp as shown with the square feature in Figure 48(d). While it is not clear the reason for the adhesion between the nanotubes and silicon stamp in the first transfer, this result suggests that altering the adhesion of the catalyst layer to the silicon can be used to manipulate the exposed surface after the transfer. In the case of the torn nanotubes, less of the iron catalyst is transferred with the nanotubes, which may be beneficial in applications where metal is not desired, for example carbon nanotube templates for biological cell growth. Transfers with the weak interface results in features with a very uniform and flat tops which are desirable for creating field emission devices on flexible substrates where a counter electrode is placed at a uniform spacing from the CNTs.

The microwave assisted transfer method creates a locally heated embossing stamp with low thermal mass which has the ability to rapidly heat and cool. This is in direct contrast to imprint lithography tools where large platens must be heated and cooled with large thermal time constants. Thus, the microwave processing provides a rapid method for nanomaterial transfer into thermoplastic polymers. The use of a silicon substrate enables the localized absorption and heating of the nanomaterials, even if the microwave energy absorptivity of the nanomaterial is low. The absorption of the microwave energy by the nanotubes is dependent on nanotube diameter, impurity concentration, and nanotube properties. While our nanotubes were metallic and approximately 20 nm in diameter, previous research suggests that small diameter single wall nanotubes are highly susceptible to microwave energy absorption and may even heat enough to thermally decompose [99-102]. Such decomposition was not seen during our exposure of multiwall carbon nanotubes as evident by SEM and Raman spectroscopy.

The patterning of vertically aligned carbon nanotubes is technologically important with applications in a wide range of technologies. This includes field emission displays, high thermal conductivity vias and interconnects, electrodes for flexible organic electronics, and superhydrophobic self cleaning surfaces. Results of experiments of water droplets on the pattern in Figure 48(a) showed a contact angle measurement of 168°. A sample image of the superhydrophobicity test can be seen in Figure 49.

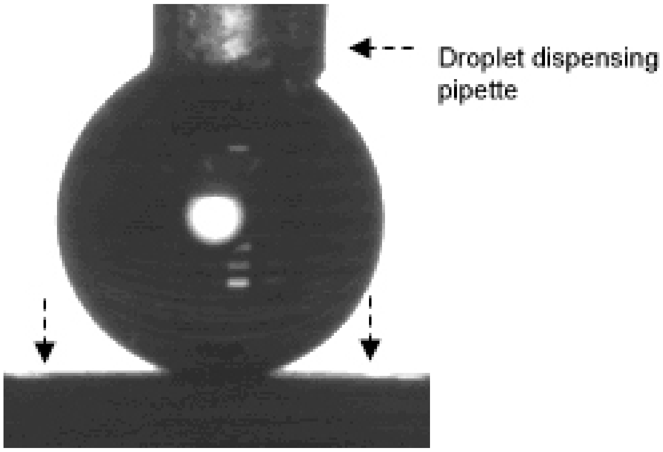

Figure 49. Hydrophobicity test of vertically standing CNTs. The CNTs proved to be superhydrophobic with a measured water droplet contact angle of 168°. The arrows in the image indicate the edges of the vertically standing CNT regions on the polymer substrate.

Optimization of nanotube pattern is expected to push this value above 170°. While the technique presented here utilized carbon nanotubes in polycarbonate, the methodology can be extended to other semiconductor nanomaterials which can be grown vertically on silicon substrates or substrates which are susceptible to microwave heating. Such nanomaterials include important wide bandgap semiconductors such as ZnO and GaN which are used in optoelectronic applications. At present, the method provides a quick and reliable process of vertical carbon nanotube printing which can be overlayed and integrated with polymer MEMS and flexible electronic devices which is not possible with other printing methods. In addition, the technology extends the integration of these materials with a wide range of thermoplastic polymers that are technologically important.

CHAPTER V: MICROBIOLOGICAL APPLICATIONS

CNT infused substrates, created by dry transfer printing, are of particular interest for select biomedical applications and microbiological research. Prosthetics research on carbon nanofibers has shown that osteoblast cells can demonstrate enhanced functionality with a decrease in nanofiber diameter [46] as well as promote a reduction in scar tissue [47]. Additional research on neuronal cell cultures has shown that CNTs, as devices, can improve neural signal transfer in a network of cells [49]. These reasons justify a further investigation into the use of neuron stimulating CNT based substrates and CNT micropatterned cell guiding substrates and are presented in the following sections.

5.1 CNT Enhanced Substrates for Neuronal Stimulation

5.1.1 Experimental Setup & Methods

An early step in showing the feasibility of using CNTs for neuronal stimulation, required demonstrating that CNTs grown on silicon would support neuronal incubation and growth. Prior to preparing the substrate however, the cells to be used in the experiment need to be cultivated and prepared. The cells that were used to investigate the possibility of using CNTs for stimulating electrodes were cortical neurons obtained from 9-day-old chicken embryos. Cerebral hemispheres were stripped of meninges, cut into small pieces, and enzymatically dissociated with 0.25% trypsin in Ca^{2+}/Mg^{2+} -free phosphate-buffered saline (PBS) for 20 min at 37 °C. The reaction was stopped by addition of 10% fetal bovine serum. After a brief centrifugation, the cells were resuspended in Dulbecco's modified Eagle's Medium (DMEM) containing 10% heat-inactivated fetal bovine serum (FBS), 100 μg/ml streptomycin, 100 U/ml penicillin G, and 292 μg/ml L-glutamine. Cells were further dissociated by trituration through a flame-constricted Pasteur pipette. Cells were then plated on collagen-coated tissue culture dish and incubated for 60 min at 37 °C in 5% CO_2 atmosphere. The non-neuronal cells attach quickly and firmly to the dish while neurons form homotypic neuronal aggregates in the supernatant. Purified neuronal cultures were subsequently prepared by harvesting, rinsing, and dissociating these neuronal aggregates by gentle trituration.

To show the feasibility of CNTs as neuron stimulators, CNTs were needed to be long and well vertically aligned. Upon reaching a height greater 100 μm, CNTs grown by thermal CVD tend to bend and lose their alignment in the vertical direction. Upon being exposed to the aqueous solution necessary to seed neurons, these CNT features would collapse. To remedy this problem, attempts were made to make the CNT features more rigid and demonstrate improved adhesion to the substrate. To achieve better adhesion to the silicon substrate a multilayered catalyst was used in the synthesis of the CNTs. After placing a clean wafer in a buffered oxide etch solution for 30 seconds, a 30 nm film of titanium was deposited underneath the standard 5 nm iron film. While acting as a diffusion barrier layer between the iron and the silicon, the titanium should show better adhesion to the silicon than the iron alone.

Another method for helping to improve the adhesion to the substrate was the use of plasma enhanced CVD (PECVD) grown silicon dioxide. In this process, vertically oriented CNTs, produced on a silicon coupon, were exposed within a Unaxis brand PECVD chamber to the reactant gases SiH_4 and N_2O. The RF power used to ignite the plasma was 25 W, the deposition duration was 2 minutes at 150 °C at a pressure of 10 torr. Following the deposition, nitrogen was used to purge the chamber of any remaining chemicals for 5 minutes prior to venting the chamber. The CNT sample was then inspected under a Canon optical microscope with a 100X objective lens and a LEO 1530 brand SEM for deposition thickness and uniformity.

Cells were seeded with a density of 25,000 cells/cm^2 on sterilized silicon wafers patterned with both types of carbon nanotubes, those produced with titanium-iron catalyst and those coated with silicon dioxide. The samples were then placed sterile in individual wells of a 24-well culture dish and cultured for 48 hr in 5% CO_2 atmosphere at 37 °C. To evaluate the cell growth present, the samples were prepared for SEM viewing. After two days of incubation on the CNT enhanced surface, cell samples were washed three times with Ca^{2+}/Mg^{2+} containing PBS. Fixation was done for 30 min in 2.5% gluteraldehyde, then substrates were rinsed three times with PBS, dehydrated by first using 10 min sequential washes in ethanol (25%, 30%, 50%, 70%, 80%, 90%, 95%, 100%), followed by 10 min sequential washes in series of hexamethyldisilazane (HMDS) (25% HMDS in ethanol; 50% HMDS in ethanol; 75% HMDS in ethanol; 100% HMDS; all solutions vol/vol). The samples were allowed to air dry, sputter-coated with gold, and examined using a LEO 1530 SEM at an acceleration voltage of 3 keV.

5.1.2 Experimental Results

The problem that was encountered, performing the cell culturing process on top of the CNTs, was that of CNTs falling over upon exposure to an aqueous solution. The first method used to overcome this lack of root adhesion was the use of multilayered catalyst. Research at Purdue University has shown that the use of a titanium buffer layer underneath the iron catalyst can help promote better adhesion of the resulting CNTs to the substrate. The cell culturing that was performed on a CNT “carpet” growth sample based on titanium iron catalyst resulted in very scarce cell proliferation and growth. The very few cells that were observed via SEM did not extend their arms in an attempt to anchor themselves.

The secondary set of CNTs that were introduced as cell growth substrates were coated in silicon dioxide to help make them more rigid. While the coatings by silicon dioxide appear uniform on the individual nanotube, the coating on all CNTs over the entire substrate was slightly less uniform. The major factors contributing to the deposition of SiO_2 in narrow, high aspect ratio trenches are chamber pressure, temperature and RF plasma power. Via an optical microscope, it was evident that as the trench width and pillar spacing became smaller, less and less of the CNT sidewalls and adjoining substrate received SiO_2 coating. The plasma deposition also had trouble penetrating the CNT array network, resulting in nanotube features with shell-like coatings. Evidence of this can be seen in an SEM image in Figure 50, as inner CNT features measure roughly 25 nm and outer features roughly 80 nm.

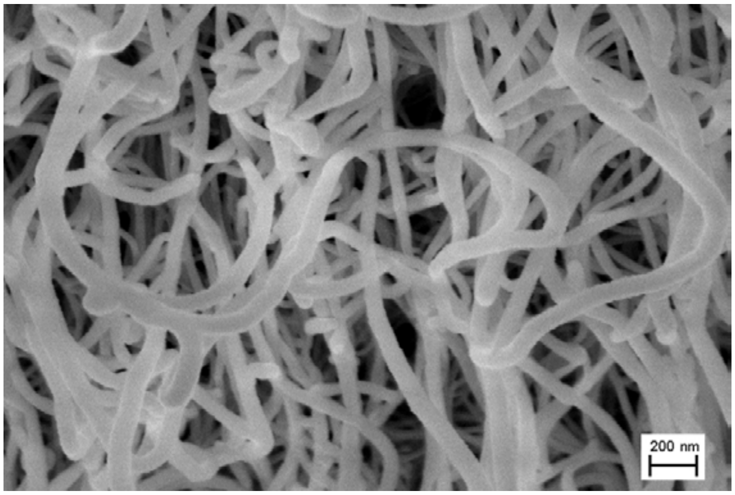

Figure 50. Scanning electron microscopy image demonstrating the uniformity of plasma enhanced deposition of SiO_2 onto CNTs. The oxide coating is shown to only adhere to the outer most CNTs where diameters are close to 80 nm. The plasma does not coat CNTs closer to the center of the group where diameters still measure close to 25 nm.

Neuron cultures investigated via SEM, show signs of adhesion and preference to the micropatterned SiO_2 coated CNTs as seen below in Figure 51(top). While it is not expected for neurons to survive and grow on silicon dioxide based surfaces, images such as in Figure 51 below indicate otherwise.

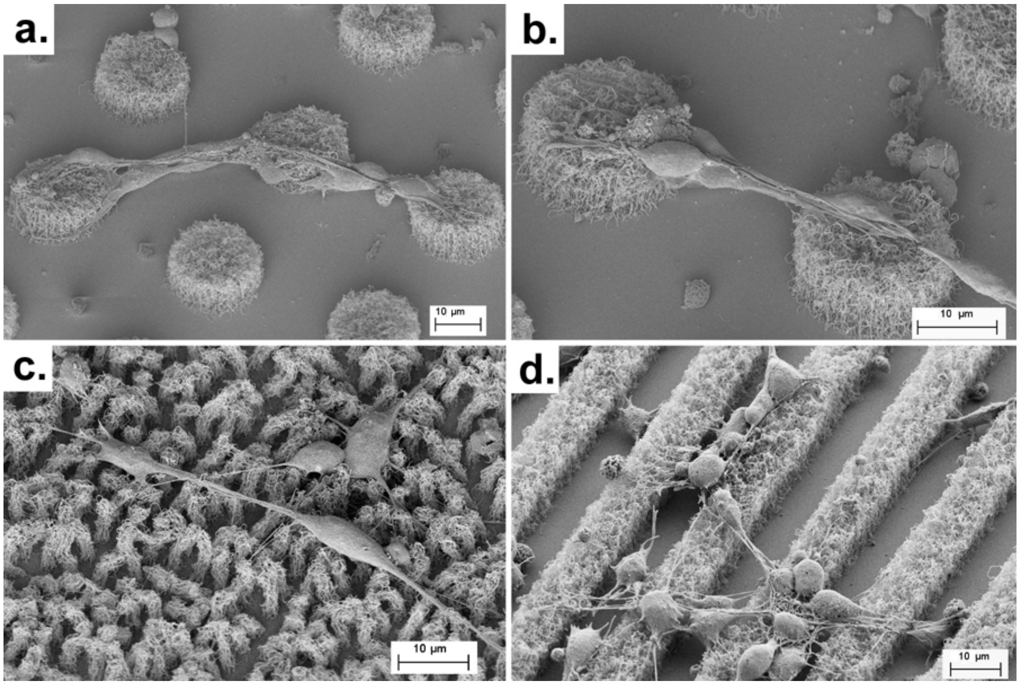

Figure 51. Scanning electron microscopy images of neurons cultured on SiO_2 coated CNTs. The neurons appear to prefer the roughened CNT surface over the bare silicon substrate. Neurons are also shown to extend between CNT features and no negative effects to the silicon dioxide coatings.

While the SiO_2 coatings had the desired effect of making the CNTs more rigid, they also act as an electrical insulator, shielding their use as an electrode. Attempts made to etch away the topside SiO_2 from the CNT features using hydrofluoric acid vapors, resulted in a nonuniform oxide etching across the entire coupon.

5.2 Cell Guidance Substrates

5.2.1 Experimental Setup & Methods

To test the use of CNT enhanced polymeric substrates for cell guidance, it was desired that as little catalyst metal be transferred to the substrate as possible. A small fraction of the time during the hot emboss, imprint lithography process, the catalytic iron that seeds the CNT growth, is transferred in addition to the CNTs. This layer of iron particles is not desired when testing the response of cells to the nanopatterned substrates. Eliminating all traces of iron catalyst is impossible, due to catalyst particles that may end up enclosed with in the CNT. Rather than the total elimination of iron catalyst, a reduction in catalyst content was therefore a goal of preparing these substrates. Another challenge of producing cell guiding nanopatterned substrates was the loss of feature sizes due to buckling and compression during the hot embossing process.

To produce the nanopatterned substrates, a photolithography mask, used in other work to help measure cellular response to a patterned substrate, was implemented in the catalyst patterning stages. This mask featured a number of circular and lined arrays that varied in size and spacing, 1-75 μm, within a 12.5 mm coupon. After the growth of silicon oxide and patterning of photoresist, the iron catalyst was evaporated onto these catalyst coupons via electron beam evaporation. The metal patterns on the coupons were then exposed via a liftoff process in acetone and then separated using a dicing saw.

To produce shorter vertically aligned CNT features, thereby reducing the chance of feature distortion, ethylene was the only carbonaceous gas to be released into the reaction zone during the soak period. CNTs were created using a temperature of 700 °C and an ethylene flow rate of 700 sccm for a total of either 1 or 2 minutes depending on the desired height. Argon was then introduced to purge the quartz tube at the end of the synthesis period. Once the furnace had cooled to less than 100 °C, the sample could be removed from the chamber.

The hot emboss imprint lithography steps taken to transfer the CNTs into the .5 mm thick Goodfellow brand polycarbonate substrates is performed similarly to the two dimensional printing described in section 4.1 of this document. The platens were each heated to a temperature of 143 °C close to the T_g of the polycarbonate sheeting, and brought into close proximity of each other to allow for thermal equilibrium. After this, the CNT sample was placed facing downward onto a polycarbonate coupon, slightly larger in size. This assembly was then placed onto a 10 cm diameter metal disk resting on a .75 cm thick rubber gasket, designed to help distribute the load evenly between the coupons. After 5 minutes of compression at a force of 667 N, the platens are cooled back to 50 °C, to allow for cooling of the polycarbonate. The platens are then separated and the embossed polycarbonate is removed from the stacked structure.

Substrates are then evaporatively coated with 100 Å Ti and 200 Å Au. A uniform coating of the protein fibronectin is then absorbed to the surface to create a uniform surface chemistry. MC3T3-E1 Osteoblasts, a bone precursor cell, are now seeded onto the substrates at a density of 200 cells/mm^2 and incubated for 24 hours at 37 °C. The cells are first permeablized using PMSF in cytoskeleton buffer and fixed using 3.7% formaldehyde. Cell structures are then stained using immunofluorescent dyes. Cell nuclei are stained using Hoechst DNA stain (Invitrogen, Eugene, OR) and the cell cytoskeleton is stained using Rhodamin Phalloidin (Invitrogen, Eugene, OR). The cells are then visualized using a Nikon fluorescent microscope. Alignment of the cell body was determined via fitting each cell nuclei with an ellipse and comparing the direction of the central axis with that of the imprinted nanofeature traces. For SEM viewing, the cells are first fixed in a 2.5% glutaraldehyde solution, dried in ethanol and then gold coated to make them conductive. Imaging was performed at an acceleration voltage of 3 kV.

5.2.2 Experimental Results

Nanotextured polycarbonate substrates were successfully fabricated and cell cultures were deposited onto the substrates and allowed to grow. In some limited cases, the cells seemed to prefer the nanotextured CNT regions of the substrate versus the nonpatterned regions. The following images in Figure 52, display some of the promising cell growth that was observed using a SEM.

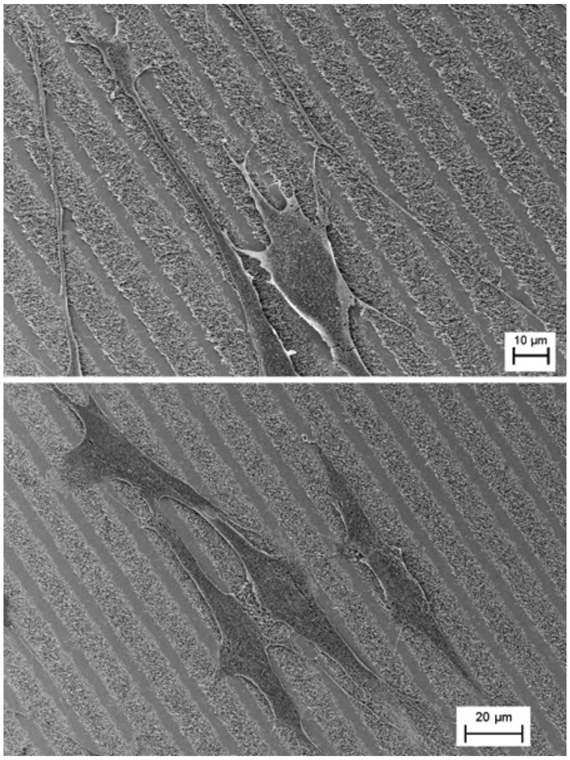

Figure 52. Scanning electron microscopy images of cellular adhesion to imprinted CNT patterns. These substrates were prepared using the hot embossing method to imprint CNTs into polycarbonate. The filopodia appear well anchored to the CNT features.

The seeding density of the cells was too large however, to make a reasonable, qualitative judgement regarding the cellular alignment to the substrate. As seen in the color altered image below in Figure 53, the cells had a large deal of interaction with each other beyond their interaction to the substrate. In Figure 53, the cells can be seen in dark spots while the substrate patterns can be seen in light grey vertical stripes.

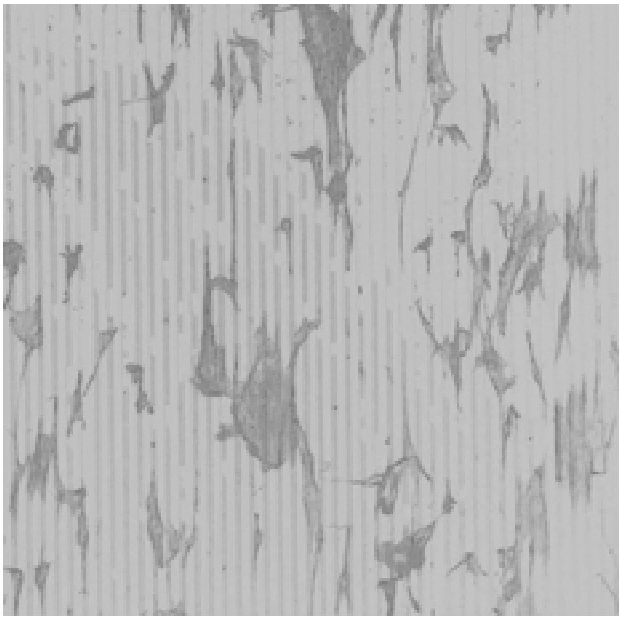

Figure 53. Florescent microscopy image of cells on CNT infused substrate. The image colors have been altered to make the cells more visible. As seen in the figure, there is a large amount of cell-cell interaction due to the high seeding density. The 5 μm CNT traces are shown as light grey vertical lines and are spaced 5 μm apart.

A conclusive decision can not therefore be made as to whether the CNT patterns are influencing the alignment and directionality of the cellular growth. There are no major differences or trends in the cellular alignment or proliferation, under the varied spacing and size of the nanostructured regions. It was expected that the cells would show the greatest response to the 10 μm or larger sized regions, because that is close to the size of the cell body.

Some of the more promising information that can be extracted from this study is that CNT based nanotextured substrates can support cellular growth. Many of the cell filopodia show interaction with the CNTs on the substrate, as they stretch out to anchor themselves to the polycarbonate.

CHAPTER VI: SUMMARY AND RECOMMENDATIONS

6.1 Summary

In this study, an investigation was performed to look at several approaches to integrating CNTs into micro-electromechanical systems (MEMS).

Synthesis of CNTs was studied in two different settings. Synthesis was first studied via a global scale chemical vapor deposition (CVD) process. By varying global growth parameters such as synthesis temperature and types of carbonaceous gases, this study attempted to qualify the output regime of the thermal CVD method using iron and nickel in nanoparticle and thin film form. Secondly, synthesis was performed directly onto a microsystem device via localized resistive heating. The achieved synthesis represents the first known instance in which CNTs were successfully synthesized onto a microsystem device that would also allow for post growth gravimetric analysis of the nanomaterials. The localized synthesis was also unique due to the use of microRaman thermometry calibration prior to the synthesis attempt. Following synthesis, the application of atomically layered, protective coatings was then investigated. In this study, aluminum oxide films were found to extend the life of MWNTs by shielding against the effects of oxidation.

Integration methods were then investigated to allow for CNT transfer to microsystem applications incapable of withstanding high synthesis temperatures. Two different integration methods were developed and demonstrated the ability to print CNTs into polymer substrates in two distinct fashions. The first method of printing by hot embossing allowed for the two dimensional transfer of randomly arranged CNTs. The functional electrical circuits which were used to evaluate this transfer method, showed reliable conductive behavior even under considerable bending strain. The second printing method of microwave embossing allows for the transfer of vertically aligned CNTs. The merits of this printing method were investigated by measuring the hydrophobicity of the imprinted CNTs on the polymer substrate. These transfer methods show promise for manufacturing of microscale electronics and enhancement of surfaces.

Lastly, post synthesis processing methods were used to create micropatterned CNT cell guidance substrates as well as neuronal stimulating substrates. Using the hot emboss imprinting method, the preferential guidance of cells on CNTs was investigated. Neuronal stimulating substrates were investigated by the deposition of silicon dioxide onto the synthesized CNTs. The neuronal cells showed favorable growth in the presence of the oxide coated CNTs.

Although the work represented in this thesis has made several large strides in the continued advancement of integrating CNTs into microsystem applications, additional work on these projects is warranted and justified. The integration of CNTs into polymers for flexible electronics and sensors is quickly becoming a hotly contended research area that should provide commercially viable products within a few years. While CNT based probe tips are already commercially available, there exists room for improvement in device design and manufacture. Additional work remains to be done on the project of CNT neuronal manipulation and possibly using CNTs for preferential cellular alignment to substrates.

6.2 Preliminary Results

6.2.1 Nonstandard Substrates

There are many reasons why silicon makes a very good substrate for producing CNTs, including its flatness, its low reactivity, high temperature resistivity and cleanliness. With the search to incorporate CNTs into various applications, however, comes the desire to perform CNT synthesis on various substrate materials. These substrates are labeled "nonstandard" due to the fact that they are either not readily available, expensive, roughened, or temperature sensitive. It is important that the well structured growth of CNTs be explored on both conventional and unconventional surfaces at high temperatures via thermal CVD. One application that is driving the desire for nonstandard substrates is the need for effective heat dissipation from copper substrates in particular. Copper is one of the best thermal conductors and is widely used within many profitable industries. If CNTs could be properly adhered to a copper surface without the intermediate use of a heat sink compound, the growth of CNTs could be viewed as a large fin array with a tremendous surface area. This is only one example of a potential use of CNTs where an alternative substrate to silicon is desirable.

An additional material of interest onto which CNTs were synthesized was MFI type zeolites. The MFI zeolite is based on the single molecule, made of a single silicon atom tetrahedrally bonded to oxygen atoms, arranged to form a porous lattice. The unidirectional metal evaporation only contacted one side of the zeolite structures and therefore resulted in the single sided growth of CNT forests. As seen in Figure 54(a), the length of the zeolite grounded CNT growth reached approximately 300µm and appeared rather consistent across the entire 1cm^2 sample.

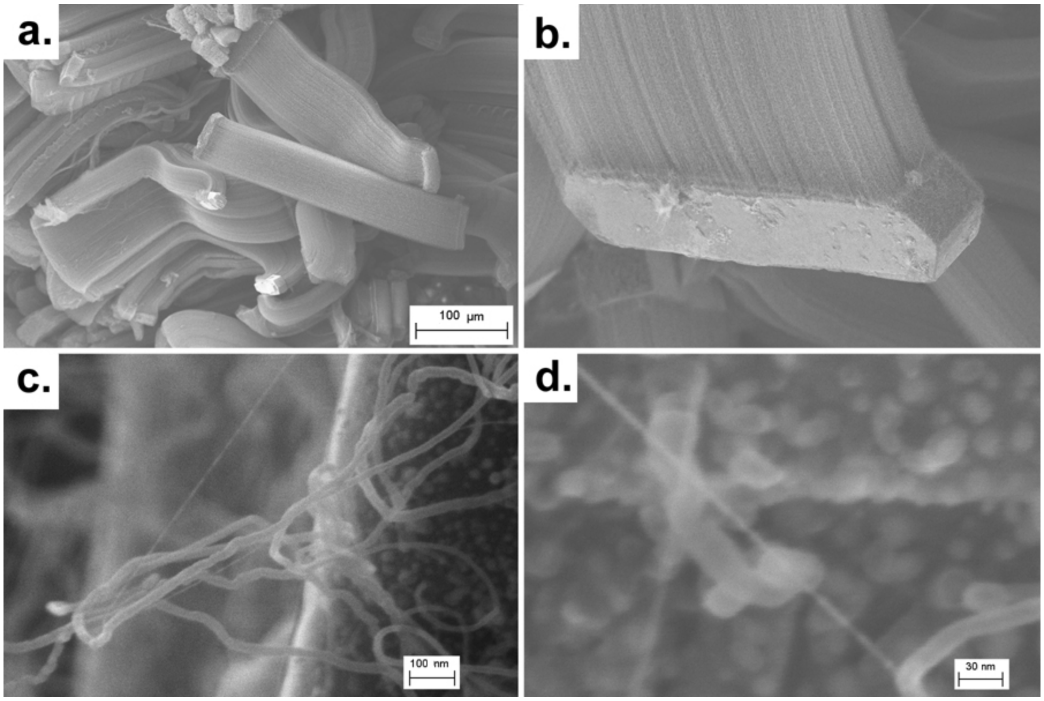

Figure 54. CNT growth onto MFI type zeolite structures. The CNT growth is quite long measuring 300 µm in length in images (a,b). Another item to note is the thin CNT in images (c,d), measuring less than 10 nm in diameter.

Even more impressive is the possibility for very small CNTs bordering the threshold in size to be SWNTs as seen in Figure 54(c,d). The CNT pictured is the same tube and stretches across the length of many zoomed viewing windows. Continued research into materials such as this should continue to yield further interesting findings.

Additional substrate materials that were investigated in this research project include graphite sheets, copper blocks, stainless steel blocks, and copper foil as shown below in Figure 55. All of these common materials received thin film catalyst coatings via electron beam evaporation. The CNT growth created on these materials did not appear as uniform as that on silicon substrates potentially due to their roughened topographies and possible alloying effects of the iron catalyst at high temperatures. Typical SEM results of synthesis attempts onto these materials can be seen in Figure 55, where images (a-d) depict growth onto graphite sheets, copper blocks, stainless steel blocks and copper foil respectively.

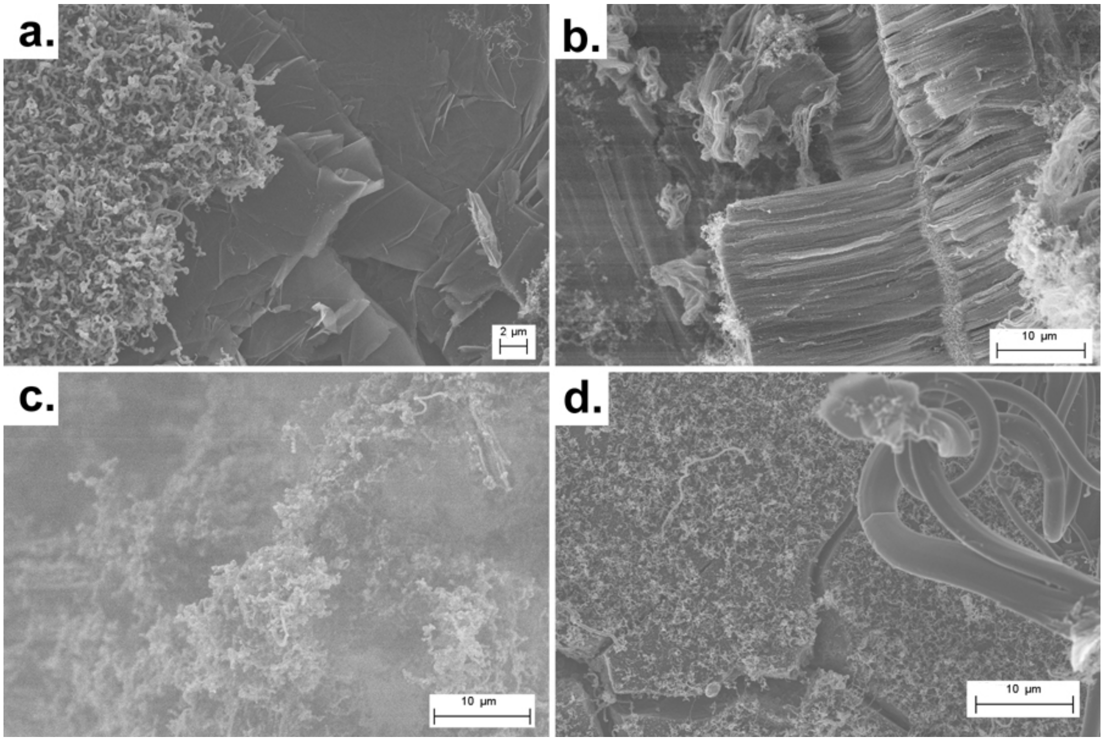

Figure 55. Images depict CNT synthesis attempts onto alternative substrates. These scanning electron microscopy images depict thin film iron growth onto a graphite sheet(a), a copper block(b), a stainless steel block(c) and lastly onto copper foil(d).

Challenging the use of high temperature processing, new synthesis methods are making the deposition of CNFs onto new and novel surfaces easier. One of these new promising methods is room temperature radio-frequency PECVD CNF synthesis [103], in which plasma is used to decompose methane.

6.2.2 Multilayered Catalysts

Preliminary work has been performed on the usage of multilayered metal catalyst layers to help improve the adhesion or properties of the resultant CNT growth. Two different combinations that have been explored in this work have been the use of iron with both aluminum and titanium underlayers. Of the two different combinations, the more successful pairing at producing vertically aligned features was aluminum-iron. A sample CNT growth image, using a 30 nm aluminum underlayer followed by a 5 nm iron layer, is shown in Figure 56.

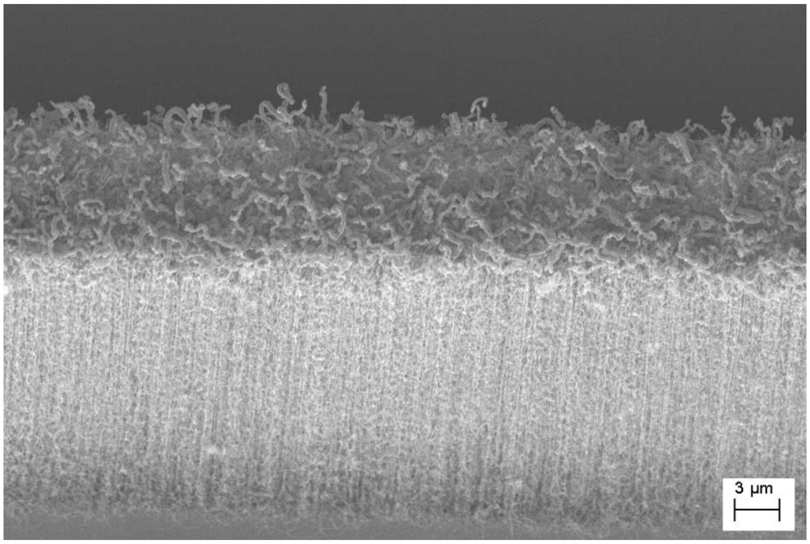

Figure 56. Scanning electron microscopy image of CNT growth using aluminum-iron thin film catalyst. The resultant structures in the image appears similar to iron thin film growth, but also exhibit a second phase of larger diameter tubules on top of the vertically aligned CNT array.

While the aluminum underlayer did allow for vertically aligned CNTs, several tens of microns in height, it also stimulated another layer of growth on top of the CNT array. This upper layer of growth featured fiber looking features measuring roughly 100-200 nm in diameter. Raman spectroscopy proved the growth to have little graphitization, thus indicating amorphous structured CNFs. Attempts to selectively oxidize the lesser structured CNFs by heating in laboratory air were not successful.

The second catalyst combination utilized titanium as the underlayer followed by a 5 nm layer of iron. This combination reacted differently than the aluminum underlayer catalyst, as no vertically aligned features were produced. A sample SEM image of the resultant growth is shown in Figure 57.

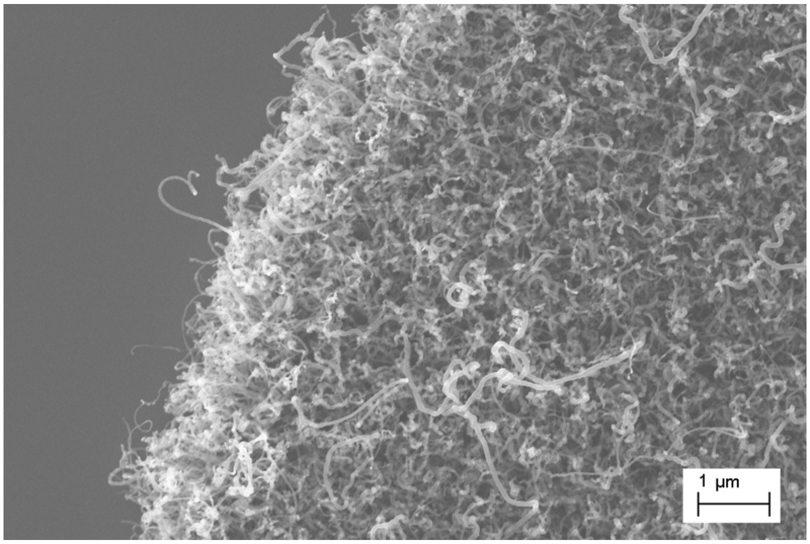

Figure 57. Scanning microscopy image of thin film titanium-iron catalyzed CNT growth. As seen in the image, titanium restricts the CNTs from achieving tall vertical alignment.

Optimization work is still being performed to find a suitable gas and temperature recipe that will produce well structured CNT growth on this catalyst combination.

6.2.3 SWNT Synthesis via Dendrimer Catalyst

Studies have shown that synthesis of SWNTs requires very small catalytic nanoparticles. The major obstacle faced in synthesizing SWNTs via thermal CVD lies in properly dispersing these metallic nanoparticles (1-2 nm) on the growth substrate. To counter this problem, recent work has started to focus on the use of dendrimer delivery based catalysts. Dendrimers are hyperbranched macromolecules that can be used in several types of applications that include forming drug delivery systems and nanoparticle templates. Studies have shown that dendrimer molecules can be used as cargos for the delivery of iron (III) acetates onto SiO2 substrates. After the initial seeding, a calcinations process, heating in air at 800 °C for 5 minutes, removes the dendrimer and begins to coalesce the Fe (III) species into iron oxide nanoparticles. The synthesis process is then carried out at 900 °C under the flow of methane, hydrogen and ethylene. Efforts are currently underway within the group of Graham et al. at the Georgia Institute of Technology to synthesize SWNTs in this manner using these commercially available supplies.

6.3 Future Work

6.3.1 Future Experiements

Experiments that remain to be performed include the successful synthesis of SWNTs via the dendrimer catalyst method, the characterization of iron thin film catalyst growth at varied conditions, the optimization of the vertical VFM based imprinting technique, and the successful implementation of CNT electrodes for neuronal stimulation.

6.3.2 Experimental Recommendations

This section outlines some aspects of the thermal CVD process and experimental setup that require further characterization if continued improvement in CNT synthesis is to continue. The first part of the process that will require a better understanding from the synthesis operator is the preparation of catalyst. This is one of the largest contributors to inconsistencies in the synthesis outcome of the tube furnace synthesis trials. Without meticulous and repetitive handling and preparation of the thin film catalyst in the microelectronics cleanroom, the synthesis trials will never be extremely reproducible. Another aspect of the synthesis process that needs to be studied is the impact made by performing synthesis in a less than clean tube. The buildup of residual carbons along the inside of the quartz tube will certainly degrade the intended CNT growth. A third issue that requires investigation is the number of catalyst containing samples that can be placed inside the tube furnace chamber at once. This issue should be investigated lastly after the catalyst and cleanliness issues have been solved. Constant conditions should give rise to constant results and when the aforementioned uncertainties are removed from the synthesis process, the validity of a given trial can be much better trusted.

REFERENCES

[1] J. P. Small, L. Shi, and P. Kim, "Mesoscopic themal and themoelectric measurements of individual carbon nanotubes," *Solid State Communications*, vol. 127, pp. 181-186, 2003.

[2] W. A. deHeer, A. Chatelain, and D. Ugarte, "A Carbon Nanotube Field-Emission Electron Source," *Science*, vol. 270, pp. 1179-1180, 1995.

[3] M. M. Treacy, T. W. Ebbesen, and J. M. Gibson, "Exceptionally high Young's modulus observed for individual carbon nanotubes," *Nature*, vol. 381, pp. 678-680, 1996.

[4] E. W. Wong, P. E. Sheehan, and C. M. Lieber, "Nanobeam Mechanics: Elasticity, Strength, and Toughness of Nanorods and Nanotubes," *Science*, vol. 277, pp. 1971-1975, 1997.

[5] S. Iijima, "Helical microtubules of graphitic carbon," *Nature*, vol. 354, pp. 56-58, 1991.

[6] C. Journet, W. K. Maser, P. Bernier, A. Loiseau, M. L. d. l. Chapelle, S. Lefrant, P. Deniard, R. Lee, and J. E. Fischer, "Large-scale production of single-walled carbon nanotubes by the electric-arc technique," *Nature*, vol. 388, pp. 756-758, 1997.

[7] Y. Saito, T. Nakahira, and S. Uemura, "Growth Conditions of Double-Walled Carbon Nanotubes in Arc Discharge," *Journal of Physical Chemistry B*, vol. 107, pp. 931-934, 2002.

[8] A. Puretzky, D. Geohegan, H. Schittenhelm, X. Fan, and M. Guillorn, "Time-resolved diagnostics of single wall carbon nanotube synthesis by laser vaporization," *Applied Surface Science*, vol. 197, pp. 552-562, 2002.

[9] A. Thess, R. Lee, P. Nikolaev, H. Dai, P. Petit, J. Robert, C. Xu, Y. H. Lee, S. G. Kim, A. G. Rinzler, D. T. Colbert, G.E.Scuseria, D. Tomanek, J. Fischer, and R. E. Smalley, "Crystalline Ropes of Metallic Carbon Nanotubes," *Science*, vol. 273, pp. 483-487, 1996.

[10] K. S. Choi, Y. S. Cho, S. Y. Hong, J. B. Park, D. J. Kim, and H. J. Kim, "The Role of Ammonia Treatment in the Alignment of the Carbon Nanotubes Synthesized with Ni and Fe via Thermal Chemical Vapor Deposition," *Journal of Korean Physical Society*, vol. 39, pp. S7-S10, 2001.

[11] Y. C. Choi, Y. M. Shin, Y. H. Lee, B. S. Lee, G.-S. Park, W. B. Choi, N. S. Lee, and J.M.Kim, "Controlling the diameter, growth rate, and density of vertically aligned carbon nanotubes synthesized by microwave plasma-enhanced chemical vapor deposition," *Applied Physics Letters*, vol. 76, pp. 2367-2369, 2000.

[12] C. J. Lee, J. H. Park, and J. Park, "Synthesis of bamboo-shaped multiwalled carbon nanotubes using thermal chemical vapor deposition," *Chemical Physics Letters*, vol. 323, pp. 560-565, 2000.

[13] F. Rohmund, L. Falk, and E. Campbell, "A simple method for the production of large arrays of aligned carbon nanotubes," *Chemical Physics Letters*, vol. 328, pp. 369-373, 2000.

[14] R.-E. M. O.A. Nerushev, D.I. Ostrovskii, M. Sveningsson, M. Jönsson, F. Rohmund, E.E.B. Campbell, "The temperature dependece of Fe-catalysed growth of carbon nanotues on silicon substrates," *Physica B*, vol. 323, pp. 51-59, 2002.

[15] H. Ago, K. Nakamura, S. Imamura, and M. Tsuji, "Growth of double-wall carbon nanotubes with diameter-controlled iron oxide nanoparticles supported on MgO," *Chemical Physics Letters*, vol. 391, pp. 308-313, 2004.

[16] J. H. Hafner, M. J. Bronikowski, B. R. Azamian, P. Nikolaev, A. G. Rinzler, D. T. Colbert, K. A. Smith, and R. E. Smalley, "Catalytic growth of single-wall carbon nanotubes from metal particles," *Chemical Physics Letters*, vol. 296, pp. 195-202, 1998.

[17] S. Sato, A. Kawabata, D. Kondo, M. Nihei, and Y. Awano, "Carbon nanotube growth from titanium-cobalt bimetallic particles as a catalyst," *Chemical Physics Letters*, vol. 402, pp. 149-154, 2005.

[18] S. N. Zaretskiy, Y.-K. Hong, D. H. Ha, J.-H. Yoon, J. Cheon, and J.-Y. Koo, "Growth of carbon nanotubes from Co nanoparticles and C_2H_2 by thermal chemical vapor deposition," *Chemical Physics Letters*, vol. 372, pp. 300-305, 2003.

[19] H. Cui, G. Eres, J. Y. Howe, A. Puretkzy, M. Varela, D. B. Geohegan, and D. H. Lowndes, "Growth behavior of carbon nanotubes of multilayered metal catalyst film in chemical vapor deposition," *Chemical Physics Letters*, vol. 374, pp. 222-228, 2003.

[20] Y. M. Shin, S. Y. Jeong, H. J. Jeong, S. J. Eum, C. W. Yang, C. Y. Park, and Y. H. Lee, "Influence of morphology of catalyst thin film on vertically aligned carbon nanotube growth," *Journal of Crystal Growth*, vol. 271, pp. 81-89, 2004.

[21] Y. J. Yoon, J. C. Bae, H. K. Baik, S. Cho, S.-J. Lee, K. M. Song, and N. S. Myung, "Growth control of single and multi-walled carbon nanotubes by thin film catalyst," *Chemical Physics Letters*, vol. 366, pp. 109-114, 2002.

[22] B. Yang, M. S. Marcus, D. G. Keppel, P. P. Zhang, Z. W. Li, B. J. Larson, D. E. Savage, J. M. Simmons, O. M. Castellini, M. A. Eriksson, and M. G. Lagally, "Template-directed carbon nanotube network using self-organized Si nanocrystals," *Applied Physics Letters*, vol. 86, pp. 1-3, 2005.

[23] E. W. Wong, M. J. Bronikowski, M. E. Hoenk, R. S. Kowalczyk, and B. D. Hunt, "Submicron patterning of iron nanoparticle monolayers for carbon nanotube growth," *Chemistry of Materials*, vol. 17, pp. 237-241, 2005.

[24] M. Hughes; and G. M. Spinks, "Multiwalled carbon-nanotube actuators," *Advanced Materials*, vol. 17, pp. 443-446, 2005.

[25] C. K. M. Fung, V. T. S. Wong, R. H. M. Chan, and W. J. Li, "Dielectrophoretic Batch Fabrication of Bundled Carbon Nanotube Thermal Sensors," *IEEE Transactions on Nanotechnology*, vol. 3, pp. 395-403, 2004.

[26] S. Hofmann, B. Kleinsorge, C. Ducati, and J. Robertson, "Controlled low-temperature growth of carbon nanofibers by plasma deposition," *New Journal of Physics*, vol. 5, pp. 153.1-13, 2003.

[27] O. Englander, D. Christensen, and L. Lin, "Local synthesis of silicon nanowires and carbon nanotubes on microbridges," *Applied Physics Letters*, vol. 82, pp. 4794-4799, 2003.

[28] M. Abel, "Thermal Metrology of Polysilicon MEMS using Raman Spectroscopy," in *Mechanical Engineering*, vol. Master of Science. Atlanta: Georgia Institute of Technology, 2005.

[29] E. Sunden, T. Wright, J. Lee, W. King, and S. Graham, "Room-temperature chemical vapor deposition and mass detection on a heated atomic force microscope cantilever," *Applied Physics Letters*, vol. 88, 2006.

[30] E. Snow, J. Novak, P. Campbell, and D. Park, "Random networks of carbon nanotubes as an electronic material," *Applied Physics Letters*, vol. 82, pp. 2145-2147, 2003.

[31] C. K. M. Fung, V. T. S. Wong, R. H. M. Chan, and W. J. Li, "Dielectrophoretic Batch Fabrication of Bundled Carbon Nanotube Thermal Sensors," *IEEE Transactions on Nanotechnology*, vol. 3, pp. 395-403, 2004.

[32] P. Yang, Y. Wu, and R. Fan, "Inorganic Semiconducting Nanowires," *International Journal of Nanoscience*, vol. 1, pp. 1-39, 2002.

[33] Y. Zhou, A. Gaur, S.-H. Hur, C. Kocabas, M. A. Meitl, M. Shim, and J. A. Rogers, "p-Channel, n-channel thin film transistors and p-n diodes based on single

wall carbon nanotube networks," *Nano Letters*, vol. 4, pp. 2031, 2004.

[34] E. Menard, K. J. Lee, D. Y. Khang, R. G. Nuzzo, and J. A. Rogers, "A printable form of silicon for high performance thin film transistors on plastic substrates," *Applied Physics Letters*, vol. 84, pp. 5398, 2004.

[35] C. Barry, N. Lwin, W. Zheng, and H. Jacobs, "Printing nanoparticle building blocks from the gas phase using nanoxerography," *Applied Physics Letters*, vol. 83, pp. 5527, 2003.

[36] G. Blanchet and J. Rogers, "Printing techniques for plastic electronics," *Journal of Imaging Science and Technology*, vol. 47, pp. 296, 2003.

[37] G. Blanchet, S. Subramoney, R. K. Bailey, G. D. Jaycox, and C. Nuckolls, "Self-assembled three-dimensional conducting network of single-wall carbon nanotubes," *Applied Physics Letters*, vol. 85, pp. 828, 2004.

[38] X. Duan, C. Niu, V. Sahi, J. Chen, W. Parce, S. Empedocles, and J. Goldman, "High-performance thin-film transistors using semiconducting nanowires and nanoribbons," *Nature*, vol. 425, pp. 274, 2003.

[39] H. Jacobs and G. M. Whitesides, "Submicrometer patterning of charge in thin-film electrets," *Science*, vol. 291, pp. 1763, 2001.

[40] M. A. Meitl, Z. Yangxin, A. Gaur, J. Seokwoo, M. Usrey, M. Strano, and J. Rogers, "Solution casting and transfer printing single-walled carbon nanotube films," *Nano Letters*, vol. 4, pp. 1643, 2004.

[41] Y. Sun, D. Khang, F. Hua, K. Hurley, R. Nuzzo, and J. Rogers, "Photolithographic route to the fabrication of micro/nanowires of III-V semiconductors," *Advanced Functional Materials*, vol. 15, pp. 30-40, 2005.

[42] Y. Sun and J. Rogers, "Fabricating semiconductor nano/microwires and transfer printing ordered arrays of them onto plastic substrates," *Nano Letters*, vol. 4, pp. 1953, 2004.

[43] X. Duan, Y. Huang, Y. Cui, J. Wang, and C. Lieber, "Indium phospide nanowires as building blocks for nanoscale electronic and optoelectronic devices," *Nature*, vol. 409, pp. 66-69, 2001.

[44] P. Smith, C. Nordquist, T. Jackson, and T. Mayer, "Electric-field assisted assembly and alignment of metallic nanowires," *Applied Physics Letters*, vol. 77, pp. `399-1401, 2000.

[45] Y. Jung, S. Kar, S. Talapatra, S. Soldano, G. Viswanathan, X. Li, Z. Yao, F. Ou, and P. Ajayan, "Aligned carbon nanotube- polymer hybrid architectures for diverse flexible electronic applications," *Nano Letters*, vol. 6, pp. 413-418, 2006.

[46] K. Elias, R. Price, and T. Webster, "Enhanced functions of osteoblasts on nanometer diameter carbon fibers," *Biomaterials*, vol. 23, pp. 3279-3287, 2002.

[47] J. McKenzie, M. Waid, R. Shi, and T. Webster, "Decreased functions of astrocytes on carbon nanofiber materials," *Biomaterials*, vol. 25, pp. 1309-1317, 2004.

[48] H. Hu, Y. Ni, V. Montana, R. Haddon, and V. Parpura, "Chemically Functionalized Carbon Nanotubes as Substrates for Neuronal Growth," *Nano Letters*, vol. 4, pp. 507-511, 2004.

[49] V. Lovat, D. Pantarotto, L. Lagostena, B. Cacciari, M. Grandolfo, M. Righi, G. Spalluto, M. Prato, and L. Ballerini, "Carbon nanotube substrate boost neuronal electrical signaling," *Nano Letters*, vol. 5, pp. 1107-1110, 2005.

[50] J. Charest, L. Bryant, A. Garcia, and W. King, "Hot embossing for micropatterned cell substrates," *Biomaterials*, vol. 25, pp. 4767-4775, 2004.

[51] R. Saito, G. Dresselhaus, and M. S. Dresselhaus, *Physial Properties of Carbon Nanotubes*. London: Imperial College Press, 1998.

[52] M. S. Dresselhaus, G. Dresselhaus, and P. C. Eklund, *Science of Fullerines and Carbon Nanotubes*: Academic, 1995.

[53] B. Bhushan, *Springer Handbook of Nanotechnology*: Springer - Verlag, 2004.

[54] N. Wang, Z. K. Tang, G. D. Li, and J. S. Chen, "Single-walled 4Å carbon nanotube arrays," *Nature*, vol. 408, pp. 50-51, 2000.

[55] J. Tersoff and R. S. Ruoff, "Structural properties of a carbon-nanotube crystal," *Physical Review Letters*, vol. 73, pp. 676, 1994.

[56] L. X. Zheng, M. J. O'Connell, S. K. Doorn, X. Z. Liao, Y. H. Zhao, E. A. Akhadov, M. A. Hoffbauer, B. J. Roop, Q. X. Jia, R. C. Dye, D. E. Peterson, S. M. Huang, J. Liu, and Y. T. Zhu, "Ultralong single-wall carbon nanotubes," *Nature Materials*, vol. 3, pp. 673, 2004.

[57] W. C. Ren and H. M. Cheng, "Herringbone-type carbon nanofibers with a small diameter and large hollow core synthesized by the catalytic decomposition of methane," *Carbon*, vol. 41, pp. 1657, 2003.

[58] H. Cui, D. Palmer, O. Zhou, and B. R. Stoner, "Aligned carbon nanotubes via microwave plasma enhanced chemical vapor deposition," presented at MRS Fall Meeting, Boston, 1999.

[59] Y. Wu and P. Yang, "Direct observation of vapor-liquid-solid nanowire growth," *Journal of American Chemical Society*, vol. 123, pp. 3165-3166, 2001.

[60] T. Guo, P. Nikolaev, A. Thess, D. T. Colbert, and R. E. Smalley, "Catalytic growth of single-walled manotubes by laser vaporization," *Chemical Physics Letters*, vol. 243, pp. 49, 1995.

[61] C. D. Scott, S. Arepalli, P. Nikolaev, and R. E. Smalley, "Growth mechanisms for single-wall carbon nanotubes in a laser-ablation process," *Applied Physics A*, vol. 72, pp. 573-580, 2001.

[62] A. Barber, R. Andrews, L. Schadler, and H. Wagner, "On the tensile strength distribution of multiwalled carbon nanotubes," *Applied physics Letters*, vol. 87, pp. 1-3, 2005.

[63] X. Zhang, T. Liu, T. V. Sreekumar, S. Kumar, V. Moore, R. Hauge, and R. E. Smalley, "Poly(vinyl alcohol)/SWNT Composite Film," *Nano Letters*, vol. 3, pp. 1285-1288, 2003.

[64] J. W. Mintmire and C. T. White, "Universal Density of States for Carbon Nanotubes," *Physical Review Letters*, vol. 81, pp. 2506-2509, 1998.

[65] S. D. M. Brown, P. Corio, A. Marucci, M. S. Dresselhaus, M. A. Pimenta, and K. Kneipp, "Anti-Stokes Raman spectra of single-walled carbon nanotubes," *Physical Review B (Condensed Matter and Materials Physics)*, vol. 61, pp. R5137-R5140, 2000.

[66] C. T. White and J. W. Mintmire, "Density of states reflects diameter in nanotubes," *Nature*, vol. 394, pp. 29, 1998.

[67] W. D. J. Callister, *Materials Science and Engineering an Introduction, 6th ed.*: Wiley, 2003.

[68] F. Li, M. Cheng, S. Bai, G. Su, and M. S. Dresselhaus, "Tensile strength of single-walled carbon nanotubes directly measured from their macroscopic ropes," *Applied Physics Letters*, vol. 77, pp. 3161-3164, 2000.

[69] M.-F. Yu, O. Lourie, M. J. Dyer, K. Moloni, T. F. Kelly, and R. S. Ruoff, "Strength and Breaking Mechanism of Multiwalled Carbon Nanotubes Under Tensile Load," *Science*, vol. 287, pp. 637-640, 2000.

[70] A. Krishnan, E. Dujardin, T. W. Ebbesen, P. N. Yianilos, and M. M. J. Treacy, "Young's modulus of single-walled nanotubes," *Physical Review B (Condensed Matter and Materials Physics)*, vol. 58, pp. 14013-14020, 1998.

[71] A. V. Melechko, V. I. Merkulov, T. E. McKnight, M. A. Guillorn, K. L. Klein, D. H. Lowndes, and M. L. Simpson, "Vertically aligned carbon nanofibers and related structures: Controlled synthesis and directed assembly," *Journal of Applied Physics*, vol. 97, pp. 041301-1-39, 2005.

[72] P. Poncharal, C. Berge, Y. Yi, Z. L. Wang, and W. d. Heer, "Room temperature ballistic conduction in carbon nanotubes," *Journal of Physical Chemistry B*, vol. 106, pp. 12104-12118, 2002.

[73] Z. Chen, J. Appenzeller, Y.-M. Lin, P. Soloman, P. Avouris, J. Sippel-Oakley, A. Rinzler, J. Tang, and S. Wind, "An Integrated Logic Circuit Assembled on a Single Carbon Nanotube," *Science*, 2005.

[74] B. F. Coll, K. A. Dean, E. Howard, S. V. Johnson, M. R. Johnson, and J. E. Jaskie, "Nano-emissive display technology for large-area HDTV," *Journal of the Society for Information Display*, vol. 14, pp. 477-485, 2006.

[75] M. Zhang, S. Fang, A. Zakhidov, S. Lee, A. Aliev, C. Williams, K. Atkinson, and R. Baughman, "Strong, Transparent, Multifunctional, Carbon Nanotube Sheets," *Science*, vol. 309, pp. 1215-1219, 2005.

[76] D. B. Hash and M. Meyyappan, "Model based comparison of thermal and plasma chemical vapor deposition of carbon nanotubes," *Journal of Applied Physics*, vol. 93, pp. 750, 2003.

[77] M. S. Kim, N. M. Rodriguez, and R. T. K. Baker, "The interaction of hydrocarbons with copper---nickel and nickel in the formation of carbon filaments," *Journal of Catalysis*, vol. 131, pp. 60, 1991.

[78] H. Kanzow and A. Ding, "Formation mechanism of single-wall carbon nanotubes on liquid-metal particles," *Physical Review B (Condensed Matter and Materials Physics)*, vol. 60, pp. 11180-11186, 1999.

[79] C. Ducati, L. Alexandrou, M. Chhowalla, G. Amaratunga, and J. Robertson, "Temperature selective growth of carbon nanotubes by chemical vapor deposition," *Journal of Applied Physics*, vol. 92, pp. 3299-3303, 2002.

[80] S. Bandow, S. Asaka, Y. Saito, A. M. Rao, L. Grigorian, E. Richter, and P. C. Eklund, "Effect of the Growth Temperature on the Diameter Distribution and Chirality of Single-Wall Carbon Nanotubes," *Physical Review Letters*, vol. 80, pp. 3779, 1998.

[81] F. Kokai, K. Takahashi, M. Yudasaka, R. Yamada, T. Ichihashi, and S. Iijima, "Growth dynamics of single-wall carbon nanotubes synthesized by CO2 laser vaporization," *Journal of Physical Chemistry B*, vol. 103, pp. 4346, 1999.

[82] J.-L. Sauvajol, E. Anglaret, S. Rols, and L. Alvarez, "Phonons in single wall carbon nanotube bundles," *CARBON*, vol. 40, pp. 1697-1714, 2002.

[83] M. S. Dresselhaus, G. Dresselhaus, A. Jorio, A. G. S. Filhos, and R. Sait, "Raman spectroscopy on isolated single wall carbon nanotubes," *CARBON*, vol. 40, pp. 2043-2061, 2002.

[84] S. Rols, A. Righi, L. Alvarez, E. Anglaret, R. Almairac, C. Journet, P. Bernier, J. L. Sauvajol, A. M. Benito, W. K. Maser, E. Munoz, M. T. Martinez, G. F. d. l. Fuente, A. Girard, and J. C. Ameline, "Diameter distribution of single wall carbon nanotubes in nanobundles," *The European Physical Journal B*, vol. 18, pp. 201-205, 2000.

[85] T. Liu and S.Kumar, "Quantitative characterization of SWNT orientation by polarized Raman spectroscopy," *Chemical Physics Letters*, vol. 378, pp. 257-262, 2003.

[86] M. Sveningsson, R.-E. Morjan, O. A. Nerushev, Y. Sato, J. Bäckström, E. E. B. Campbell, and F. Rohmund, "Raman spectroscopy and field-emission properties of CVD-grown carbon-nanotube films," *Applied Physics A*, vol. 73, pp. 409-418, 2001.

[87] T. L. W. Qian, F. Wei, H. Yuan, "Quantitative Raman characterization of the mixed samples of the single and multi-wall carbon nanotubes," *CARBON*, vol. 41, pp. 1851-1864, 2003.

[88] Y. S. Park, Y. C. Choi, K. S. Kim, D.-C. Chung, and Y. H. Lee, "High yield purification of multiwalled carbon nanotubes by selective oxidation during thermal annealing," *Carbon*, vol. 39, pp. 655-661, 2001.

[89] B. W. Chui, T. D. Stowe, Y. S. Ju, K. E. Goodson, T. W. Kenny, H. J. Mamin, B. D. Terris, and R. P. Ried, "Low-Stiffness Silicon Cantilever with Integrated Heaters and Piezoresistive Sensors for High-Density Data Storage," *Journal of Microelectromechanical Systems*, vol. 7, pp. 69-78, 1998.

[90] P. Vettiger and G. Binnig, "The nanodrive project," *Scientific American*, vol. 288, pp. 46-53, 2003.

[91] W. P. King, T. W. Kenny, and K. E. Goodson, "Comparison of thermal and piezoresistive sensing approaches for atomic force microscopy topography measurements," *Applied Physics Letters*, vol. 85, pp. 2086-2088, 2004.

[92] P. E. Sheehan, L. J. Whitman, W. P. King, and B. A. Nelson, "Nanoscale deposition of solid inks via thermal dip pen nanolithography," *Applied Physics Letters*, vol. 85, pp. 1589-1591, 2004.

[93] L. Delzeit, C. V. Nguyen, B. Chen, R. Stevens, A. Cassell, J. Han, and M. Meyyappan, "Multiwalled carbon nanotues by chemical vapor deposition using multilayered metal catalysts," *Journal of Chemical Physics*, vol. 106, pp. 5629-5635, 2002.

[94] M. R. Abel, T. L. Wright, E. O. Sunden, S. Graham, W. P. King, and M. J. Lance, "Thermal Metrology of Silicon Microstructures using Raman Spectroscopy," *Semi-Therm*, vol. 21, pp. 235-242, 2005.

[95] G. Y. Chen, R. J. Warmack, T. Thundat, D. P. Allison, and A. Huang, "Resonance Response Of Scanning Force Microscopy Cantilevers," *Review Of Scientific Instruments*, vol. 65, pp. 2532-2537, 1994.

[96] N. A. Burnham and R. J. Colton, "Measuring The Nanomechanical Properties And Surface Forces Of Materials Using An Atomic Force Microscope," *Journal Of Vacuum Science & Technology A-Vacuum Surfaces And Films*, vol. 7, pp. 2906-2913, 1989.

[97] M. D. Groner, F. H. Fabreguette, J. W. Elam, and S. M. George, "Low-Temperature Al_2O_3 Atomic Layer Deposition," *Chemistry of Materials*, vol. 16, pp. 639-645, 2004.

[98] A. C. Allen, E. Sunden, A. Cannon, S. Graham, and W. King, "Nanomaterial transfer using hot embossing for flexible electronic devices," *Applied Physics Letters*, vol. 88, pp. 083112, 2006.

[99] R. C. Che, C. Y. Zhi, C. Y. Liang, and X. G. Zhou, "Fabrication and microwave absorption of carbon nanotubes CoFe spinel nanocomposite," *Applied Physics Letters*, vol. 88, pp. 033105, 2006.

[100] J. N. Dahiya, R. Athinarayanan, J. A. Roberts, J. M. Tour, and D. W. Price Jr, "Microwave absorption in liquid crystals and carbon nanotubes," Ostrava, Czech Republic, 2004.

[101] T. J. Imholt, C. A. Dyke, B. Hasslacher, J. M. Perez, D. W. Price, J. A. Roberts, J. B. Scott, A. Wadhawan, Z. Ye, and J. M. Tour, "Nanotubes in microwave fields: light emission, intense heat, outgassing, and reconstruction," *Chemistry of Materials*, vol. 15, pp. 3969-70, 2003.

[102] A. Wadhawan, D. Garrett, and J. M. Perez, "Nanoparticle-assisted microwave absorption by single-wall carbon nanotubes," *Applied Physics Letters*, vol. 83, pp. 2683-2685, 2003.

[103] B. O. Boskovic, V. Stolojan, R. U. Khan, S. Haq, and S. R. Silva, "Large-area synthesis of carbon nanofibers at room temperature," *Science Materials*, vol. 3, pp. 165-168, 2002.